Quantum Control of Spin Systems in Diamond

by

Masashi Hirose

B.S., Keio University (2009)

Submitted to the Department of Nuclear Science and Engineering
in partial fulfillment of the requirements for the degree of

Doctor of Philosophy in Nuclear Science and Engineering

at the

MASSACHUSETTS INSTITUTE OF TECHNOLOGY

September 2015

Author .....
Department of Nuclear Science and Engineering
June, 2015

Certified by .....
Paola Cappellaro
Esther and Harold E. Edgerton Associate Professor of Nuclear Science and Engineering
Thesis Supervisor

Certified by .....
Bilge Yildiz
Associate Professor of Nuclear Science and Engineering, and Associate Professor of Materials Science and Engineering
Thesis Reader

Accepted by .....
Mujid S. Kazimi
TEPCO Professor of Nuclear Engineering
Chairman, Departmental Committee on Graduate Students

Quantum Control of Spin Systems in Diamond

by

Masashi Hirose

Submitted to the Department of Nuclear Science and Engineering
on June, 2015, in partial fulfillment of the
requirements for the degree of
Doctor of Philosophy in Nuclear Science and Engineering

Abstract

The precise control of a system which behaves according to the principles of quantum mechanics is an essential task in order to fully harness the unique properties of quantum mechanics, such as superposition and entanglement, for practical applications. Leveraging the quantum nature of the system would enable, for example, the implementation of quantum computation and quantum metrology. However, any realistic quantum system is inevitably coupled to its environment. The interaction with its surroundings irrevocably destroys the quantum nature of the system: mitigating decoherence is thus one of the central problems in quantum control. In this thesis, we develop novel control methods to protect a qubit from decoherence by two distinct approaches, and demonstrate them experimentally using the nitrogen-vacancy (NV) center in diamond.

The first approach rests on an open-loop control scheme and is tailored to improve quantum sensing tasks. We develop a continuous dynamical decoupling (CoDD) method that allows us to tune the degree of protection from a dephasing environment. Exploiting this flexibility, we show that the CoDD can be used to measure magnetic fields with sensitivity comparable to existing methods, while providing superior versatility in practical experimental settings. This protocol can adapt to various sensing conditions that might occur in biological and materials science such as measurement time and sensitive frequency.

The second approach exploits a coherent feedback protocol. We take advantage of a long-lived nuclear spin as an ancillary spin to protect the qubit of interest from decoherence. We show that the protocol protects the qubit as long as open-loop dynamical decoupling control schemes and it can be used against more general types of noise than the open-loop protocol. This method thus offers an alternative protocol to protect the qubit from decoherence in quantum computation and quantum metrology.

Thesis Supervisor: Paola Cappellaro
Title: Esther and Harold E. Edgerton Associate Professor of Nuclear Science and Engineering

Thesis Reader: Bilge Yildiz
Title: Associate Professor of Nuclear Science and Engineering, and Associate Professor of Materials Science and Engineering

Acknowledgments

My graduate research toward my Ph.D. over the six years at MIT has been exciting, intriguing and intellectually challenging. The completion of this work could not have been possible without supports of many people.

First and foremost, I would like to give very special thanks to my mentor, Paola, who convinced me to study at MIT and guided me all through my graduate year. Paola is a tremendously patient mentor who always gave me freedom and time to understand in my own way and has taught me the importance of thinking thoroughly and exhaustively.

Also, I would like to thank all of the past and present members at Quantum Engineering Group (QEG). In particular, from the very first day at the lab, I have been fortunate to work with my brilliant coworker, Clarice, who taught me fundamental skills of experiments. I would like to note that some of results in this thesis are attributable to a close collaborative work with her. Also, I would like to thank my hard-working partner, Mo, whom I closely worked with in the last year. In addition, I have been lucky to work with Alex from the early stage, who truly inspires me with his passion for science. I would like to thank Alex for providing a lot of comments and suggestions on this thesis. Also, I would like to thank Ashok, with whom I had shared a office room for five years. The conversations with Ashok was always enthralling and thought-provoking. I am also grateful to all other members of QEG: Gurneet, Honam, Easwar, Gary, Ulf, Elica, Laura, Joe, Luca, Kasturi, JC, Ken, Akira, Yixiang, and Calvin.

I would like to thank my friends in Japanese community at MIT, who shaped a precious part of my life at MIT. To mingle with them always made me feel at home. Numerous memories with them are invaluable.

Finally, I would like to thank my parents and grandmother in Japan and my wife, Chieh, who supported and encouraged me during the hardest time of my graduate studies. I could not have finished this work without her dedication.

Contents

List of Figures

List of Tables

Chapter 1

Introduction

1.1 Control of Quantum Systems

The precise control of a system which behaves according to the principles of quantum mechanics is an indispensable task in order to fully harness the uniqueness of quantum mechanics, such as superposition and entanglement, for practical applications. Leveraging the quantum nature of the system would enable, for example, the implementation of efficient computation (quantum computation) [132, 55] and high-precision measurements (quantum metrology) [21, 50].

However, any realistic quantum system is inevitably coupled to its environment. The interaction with its surroundings irrevocably destroys the coherent superposition of the system (*decoherence*) in course of time [158]. Mitigating decoherence is one of the central problems in quantum control and as such it has been intensively investigated.

A common scheme to protect the system from decoherence is dynamical decoupling (DD), which has been first introduced in nuclear magnetic resonance (NMR) [61] and essentially eliminates decoherence by modulating the slow-varying interaction with the environment [143, 144]. While DD attains a great success in extending coherence time, it fails against fast-varying (Markovian) noise that ultimately limits the coherence time. Several schemes to overcome Markovian noise such as quantum error correction (QEC) and decoherence free subspace (DFS) have been explored,

however they require large overheads. On the other hand, with the goal of performing quantum computation and quantum metrology, the system needs to be decoupled from the environment while still being sensitive to the control field or the unknown field to be estimated. Meeting these conflicting demands is a non-trivial task and has not been fully explored and it is the unifying theme of this thesis work.

The criteria for an ideal platform capable of reaching the goal of quantum computing were clearly identified by David DiVicenzo [35]: (i) a system is a scalable physical system with well-defined qubits i.e. two level systems encoding a bit of quantum information, (ii) the system is able to be initialized into a simple fiducial state, (iii) the system exhibits a long coherence time, enabling implementation of multiple quantum gate operations, (iv) a universal set of quantum gates (one-qubit gates and two-qubits (C-NOT) gates) are implementable, (v) states of the specific qubit can be measured. Many physical systems have been investigated as potential qubits. For example, ionized (or neutral) atoms can be trapped by electromagnetic field (or optical lattice) and controlled by microwave. While isolated atoms exhibit long coherence time (few seconds), the controllability degrades as the system gets larger. On the other hand, solid-state spin system, such as the phosphorus donors in silicon, hold promise for scalability by exploiting full-fledged semiconductor fabrication techniques. While the phosphorus spin can be coherently manipulated and read out by means of conventional electron spin resonance (ESR) techniques, since the phosphorus lies close to the conduction band, the phosphorus spin needs to be cooled down below few K to suppress the thermal excitations, thereby limiting working conditions. Also, the ESR measurement requires ensemble of spins and thus accessibility to single spin system is difficult to achieve.

The nitrogen vacancy (NV) center in diamond is another promising platform of quantum information as it can be isolated and readout individually while exhibiting long coherence time even at room temperature. Also, its unique spin dependent relaxation process from the optically excited state enables a polarization and readout of the spin state. In addition, nuclear spins close-by to the NV center can be controlled by the NV center and provide local quantum registers.

In this thesis, we develop novel control methods to protect qubits from decoherence by two distinct approaches. The first method rests on an open loop control scheme and it is tailored to improve quantum sensing tasks. We develop a continuous dynamical decoupling (CoDD) method which can be used to tune the degree of the protection from an environment. Exploiting this flexibility, we show that the CoDD can be used to measure magnetic fields with sensitivity comparable to existing methods while providing superior flexibility in practical experimental settings e.g., measurement time and frequency. This protocol can adapt to various sensing conditions that might occur in biological science and materials science. The second method exploits a coherent feedback protocol. We take advantage of a long-lived nuclear spin as an ancillary spin to protect the qubit of interest from the decoherence. We show that the protocol protects the qubit as long as the open loop control scheme and it can be used against more general types of noise than the open-loop protocol covers. This method thus offers an alternative protocol to protect the qubit from decoherence in quantum computation and quantum metrology applications.

1.2 Overview of the Thesis

In chapter 2, spin qubit system in diamond is described. The former part of the chapter 2 addresses the structure and properties of the NV center in diamond. Then, the experimental methods to isolate, manipulate and measure a single NV center are described along with experiment data. In the latter part, we investigate a polarization, a coherent control and detection of a single nitrogen nuclear spin. Chapter 3 and 4 contains the main result of this thesis. In chapter 3, we apply an open-loop control scheme to enhance the sensitivity of the single spin magnetometry. Specifically, we consider a continuous dynamical decoupling (e.g., rotary echo sequence) for sensing DC/AC magnetic fields. We show that the continuous dynamical decoupling magnetometry provides the comparable sensitivity for DC field while attaining better compromise between the measurement time and the sensitivity. Also, for sensing the AC field, we show that the continuous dynamical decoupling offers better sensitivity and compro-

mise between bandwidth and sensitivity than pulsed dynamical decoupling does. In the chapter 4, we implement a feedback control algorithm that protects an electronic spin associated with the NV center in diamond against dephasing noise. We exploit a long-lived nuclear spin qubit as an auxiliary system to implement a coherent feedback scheme that achieves long protection time, while avoiding active decoupling control on the protected qubit. We further explore an interesting trade-off between information gain and decoherence protection, as measurement of the auxiliary qubit state after the feedback algorithm voids the protection, even if the rest of the dynamics is unchanged.

Chapter 2

Spin Qubits in Diamond

2.1 Introduction

Diamond is a semiconductor with a wide band gap of 5.5 eV (225nm, UV). While a perfect diamond should be transparent in a wide range, diamond hosts more than than 100 color centers within its wide band gap and possess a unique optical property which is used to classify diamonds [157]. The nitrogen-vacancy (NV) center is one of the nitrogen-related color centers and a point defect which consists of the substitutional nitrogen-vacancy pair in diamond. The existence of the NV center was firstly reported in 1965 by du Preez [40] by conducting an absorption measurements of an irradiated diamond which contains large quantities of nitrogen. The symmetry of the center (trigonal) was confirmed by photoluminescence measurement [27] and uniaxial stress measurements [31]. The negative charge state and the electronic structure of the NV cener based on molecular orbitals (MOs) were proposed through electron spin resonance (ESR) measurements [93]. Thanks to advancement of single molecule spectroscopy, the NV center was later individually addressed by scanning confocal microscopy [56]. As it was found to be a stable single-photon source at room temperature [87], it was subsequently applied to quantum optics experiments [12]. In addition, the electronic spin of the NV center exhibits long coherence time even at room temperature as confirmed by optically-detected magnetic resonance (ODMR) [74] and the NV center was recognized as a promising system for magnetometry [139]

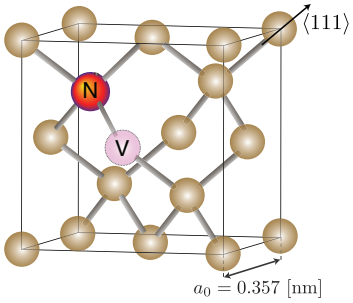

Figure 2-1: The nitrogen vacancy center in diamond. The NV center has the trigonal symmetry of point group C_{3v} in which its principal axis is along the crystallographic $\langle 111 \rangle$ direction.

and also a qubit for quantum information processing [153]x.

2.2 The Nitrogen Vacancy Center in Diamond

2.2.1 Orbital Structure

The electronic structure of the NV center is confirmed to be localized around the vacancy site by ESR measurements [68, 69] and thus can be modelled by a molecular orbital in which the wavefunction is given by a linear combination of atomic orbitals (LCAO). The basis function of the molecular orbitals (MOs) is given by tetrahedrally coordinated sp^3 orbitals of dangling bonds of nearest three carbon atoms ($\phi_{C_{1,2,3}}$) and the adjacent nitrogen atom (ϕ_N). [1] Ab initio calculation studies have determined a number of MOs, their symmetry and energy ordering and confirmed that the LCAOs of these basis function form three MOs in the band gap (a_1, e_x, e_y) and one MO in

[1]The orbits of unsatisfied dangling electrons are not exactly given by the sp^3 hybridization of its each atomic orbitals. The orbit of the carbon atoms ($\phi_{C_{1,2,3}}$) possess a strong p-orbital nature ($p/s = 9.8$) extending toward the vacancy site whereas that of the nitrogen (ϕ_N) has a equal mixture of the s-orbital and the p-orbital ($p/s = 1.2$) [47].

the valence band (a_1') which are given by

$$a_1 = \phi_N, a_1' = \frac{1}{\sqrt{3}S_1}(\phi_{C_1} + \phi_{C_2} + \phi_{C_3} - 3\beta\phi_N)$$
$$e_x = \frac{1}{\sqrt{3}S_2}(-\phi_{C_1} - \phi_{C_2} + 2\phi_{C_3}), e_y = \frac{1}{S_2}(\phi_{C_1} - \phi_{C_2}) \tag{2.1}$$

where $S_1 = \sqrt{1 + 2\alpha - 3\beta^2}, S_2 = \sqrt{2 - 2\alpha}, \alpha = \langle\phi_{C_1}|\phi_{C_2}\rangle$, and $\beta = \langle\phi_{C_3}|\phi_N\rangle$ [47, 71]. Note that the orbits $e_{x,y}$ are degenerate and do not include the nitrogen dangling bond. The NV center consists of six electrons in which two of them fill the a_1 orbital and do not contribute to observable properties. Thus, electronic configuration is represented by a configuration of four electrons filling the $a_1, e_{x,y}$ orbitals. Then, the symmetry of the NV center (C_{3v}) has to be considered to construct the electronic structure. [2] The trigonal symmetry (C_{3v}) has three irreducible representations [3] A_1, A_2, E and the electronic structure can be constructed by a direct product of linear combination of these MOs and its spin function which belong to one of these irreducible representations. [4] We consider the ground state electronic configuration $a_1^2e^2$ and the first excited configuration a_1e^3. Due to the exchange interaction of two unpaired electrons, there exists the spin-triplet ($S = 1$) state and the spin-singlet ($S = 0$) state. The ground state of the NV center is confirmed to be the spin-triplet state indicated by the Hund's rule and thus provides an effective spin.

[2] Symmetry elements of the NV center consist of 3-fold rotation symmetry around the [111] axis with the addition of a mirror reflection plane parallel to the rotation axis ([111]). These elements of the trigonal point group which are common in molecules (e.g. NH_3) and defects in solids (e.g. B-H in Si) are often represented by C_{3v} in the Schönflies notation where C_n stands for n-fold cyclic (rotational) symmetry and v stands for a (vertical) mirror plane containing a rotation axis.

[3] An irreducible representation of a point group is often described by the Mulliken symbols. A/B stands for symmetric/anti-symmetric with respect to rotation around the principal axis (one dimensional representation) while E stands for degenerate.

[4] The orbital and spin part can be constructed independently as long as they satisfy the symmetry and this is based on the assumption that the spin-orbit coupling is not considered. This is found to be the case in the ground state, but not in the excited state and then the spin-orbit coupling needs to be included as a perturbation.

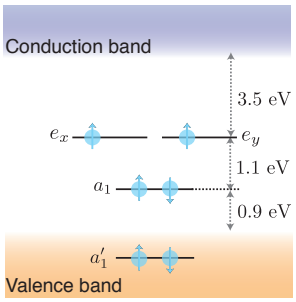

Figure 2-2: Molecular orbital models of the negatively charged NV center (six-electron model). The figure shows the configuration of the ground state ${}^3A_2(a_1^2e^2)$. All of the MOs are located far from conduction and valence bands and are well separated from each other. These properties enable the spin decoupled from the thermal excitations and optical transitions without ionization.

2.2.2 Spin Structures

So far, only coulomb potential in the local lattice and the orbital interactions ($10^2 - 10^5$GHz) are considered. In addition, the spin-orbit interaction and the spin-spin interaction (MHz-GHz) need to be considered as a perturbation.

Ground triplet state ${}^3A_2$

The ground state of the NV center is given by the electronic configuration ${}^3A_2(a_1^2e^2)$ with the spin-triplet state and the orbital singlet. The small anisotropy of the g-factor in the ground state implies that the spin-orbit coupling is negligible [43] and thus the system can be described effectively only by the spin operators of two unpaired electrons filling the $e_{x,y}$ orbitals. The dipole interaction between these two electrons induces an energy splitting (2.87 GHz) between the $m_s = 0$ and the $m_s = \pm 1$ fine structure levels which quantizes the NV system along the [111] axis. [5] The Hamilto-

[5]The full description of the zero field splitting is given by $\mathcal{H}_{ss} = D_x S_x^2 + D_y S_y^2 + D_z S_z^2$ where $D_{x,y,z}$ are the principal values of the fine structure tensor. Since it holds that $D_x + D_y + D_z = 0$ and $S_x^2 + S_y^2 + S_z^2 = S(S+1)$, the Hamiltonian of the zero-field splitting is reduced to

$$\mathcal{H} = DS_z^2 + E(S_x^2 - S_y^2) - \frac{1}{3}DS(S+1) \tag{2.2}$$

where $D = 3/2D_z$ and $E = (D_x - D_y)/2$. The last term is usually dropped. The E term which further splits $m_s = \pm 1$ is due to the lack of inversion symmetry.

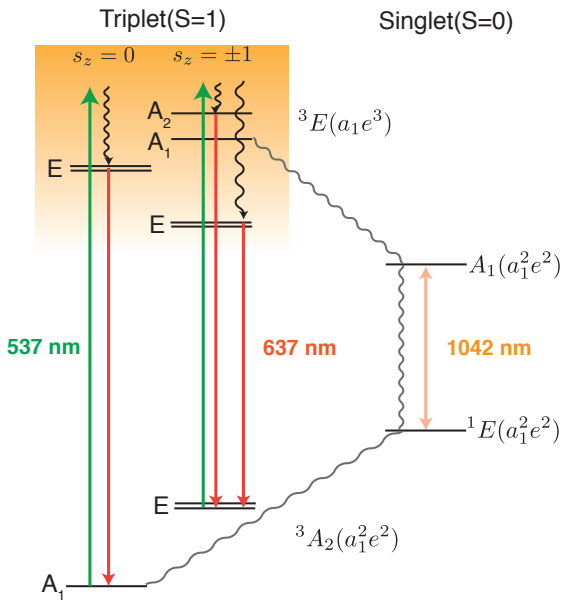

Figure 2-3: The electronic structure of the NV center. It consists of a ground triplet state ($^3A_2(a_1^2e^2)$), an excited triplet ($^3E(a_1e^3)$) and two intermediate singlet states (A_1,^1E). The singlet state of the first excited MO configuration which exists above ^3E is omitted. The gray wavy lines indicate non-radiative transition in which the relaxation of the electron is driven by a local phonon mode whereas the colored lines show radiative transition. In the transition between A_1 and ^1E, the radiative/non-radiative relaxation progresses at the same time while the radiative relaxation is much weaker than the other.

nian of the ground state NV center under a static magnetic field is given by

$$\mathcal{H} = DS_z^2 + g\mu_B \boldsymbol{BS} \tag{2.3}$$

where $D \sim 2.87$ GHz is a zero-field splitting constant, $\boldsymbol{B}$ is a static magnetic field typically applied along [111] , and $g_e = 2.0028$ is the effective g-factor [69, 68]. The ground state is quantized along the principal axis of the fine structure tensor, i.e. [111] direction. Thus, the eigenstate is given by $|m_s\rangle$ where $m_s = 0, \pm 1$ indicate a projective component of the total spin along [111]. The static magnetic field along the crystal axis can lift up degeneracy in $|\pm 1\rangle$ by Zeeman interaction. (Fig.2-7(a))

Excited triplet state ^3E

The first excited state of the NV center is given by the electronic configuration $^3E(a_1e^3)$ with the spin-triplet state and, unlike the ground state, has an orbital doublet consisting of two unpaired electrons occupying a_1 and $e_{x,y}$. The fine structure of the excited state is experimentally confirmed to be very different for every NV center at low temperature and this is ascribed to the orbital structure being very sensitive to local strain which indeed splits the doubly degenerate orbitals [9]. However, at room temperature, the phonon-related thermal excitations mix the orbital doublet without affecting spin projection component and thus the orbitals are averaged out into the singlet with zero orbital angular momentum [121]. This quenching of the orbital angular momentum significantly simplifies the fine structure, enabling a model of the spin Hamiltonian with few parameters which has no variations among the NV centers.

Thus, the Hamiltonian of the excited triplet spin at zero field is given by

$$\mathcal{H}_e = D_e S_z^2 + E(S_x^2 - S_y^2) + \lambda_\parallel L_z S_z + \lambda_\perp (L_x S_x + L_y S_y) \tag{2.4}$$

where $D_e = 1.42$ GHz is the zero-field splitting, $E(\sim$ MHz-GHz) is the fine structure constant proportional to the local strain field [9, 46], and $\lambda_\parallel = 4.4$GHz and $\lambda_\perp = 0.2$GHz are the spin-orbit coupling constants [137]. The spin-orbit coupling in the excited state plays a crucial role in intersystem crossing between the singlet and the triplet states, leading to spin polarization and spin detection of the NV center [98, 97]. The axial part of the spin-orbit coupling lifts the degeneracy of the spin triplet E states, which is then splitted into three double degenerate states ($E_{x,y}(m_s = \pm 1), E_{1,2}(0), A_1(\pm 1), A_2(\pm 1)$) [9]. Then, the local strain E splits the degeneracy of A_1 and A_2. The non-axial part of the spin-orbit coupling induces an intersystem crossing transition between states with the same irreducible representation [98]. Thus, only part of the triplet excited state ($A_1(a_1e^3)$) is allowed to decay to the singlet state ($A_1(a_1^2e^2)$).

Intermediate singlet state $^1A_1$ and ^1E

There exist two singlet states with energy between the ground and the first excited states which both have the same orbital structure as the ground state. The energy ordering of these two states had been in question for some time [99] and has been recently determined [120]. The transition between these two states are mainly driven by coupling to phonon vibrations associated with a weak infrared emission at 1042 nm (1.19 eV/9597 cm^{-1}) [119, 120]. The intermediate states are weakly connected to the triplet ground and excited states via the spin-orbit coupling and phonon coupling and this relaxation process preferably occurs at the excited states with $m_s = \pm 1$, which then relaxes into the ground state with $m_s = 0$. Thus, the intermediate states play a crucial role in polarizing the state of the NV center.

2.2.3 Charge State

It has been known that the NV center has different charge states which can be distinguished by their unique optical zero phonon lines, which directly refer to the electronic transitions, characterized by the ZPL at 637nm (1.945 eV) for (NV^-) and at 575 nm (2.156eV) for (NV^0). The charge state affects the electronic configuration which leads to a different spin configuration. The negatively charged NV center (NV^-) is formed by six electrons in which five of them are provided by the dangling bonds of the nearest carbons and nitrogen atom while the sixth electron is presumed to be donated from a nearby substitutional nitrogen (P1 center) [93]. The neutral charge state of the NV center is formed by five electrons and it is also photostable state. The charge state depends on its transition energy with respect to the Fermi energy which is determined by the local environment of the NV center, i.e. the existence of nearby nitrogen donors. The NV^- state has been observed to be turning into the neutral state under various kinds of illuminations [146]. The charge states can be stabilized and switched by manipulating the Fermi energy of the surface [54]. The switching of the charge states can be applied for decoupling from magnetic noise of the environment [100] and diffraction-unlimited resolution microscopy [63]. The NV^- exhibits

attractive properties as quantum system since it can be initialized and readout as we will explain later. Thus, in this thesis, we address only the negatively charged NV center which is referred to as NV unless specified.

2.2.4 Optical Properties

Off-resonant illumination at 532 nm excites the ground state NV center to the first excited state. After losing energy to vibrational (phonon) excitations, the state is rearranged to ${}^3E(a_1e^3)$ and then decays into the ground state by spontaneous emission of photons at 637 nm. At room temperature, the orbital part of the excited state is thermally mixed and the spin projection is preserved like the ground state. Thus, the rearrangement of the spin projection does not occur during the optical cycle. As a result, this off-resonant illumination between the spin triplets completely conserves the spin projection at room temperature. [6] However, spin-orbit coupling in the excited state gives rise to intersystem crossing, i.e., transition between the triplet and the singlet states. The intersystem crossing preferably (six times more likely [118]) occurs in the $m_s = \pm 1$ manifolds in the excited state. The intersystem crossing from the singlet to the ground triplet state occurs via coupling with phonons [97] and experiment indicates that the spin preferably decays to $m_s = 0$ state. This spin-dependent and non-spin preserving relaxation process leads to polarization of the spin state into the $m_s = 0$ state ($P \sim 80\%$) after a few optical cycles [65]. The incomplete polarization is ascribed to the non-spin preserving transition between the two triplet states due to the spin-orbit coupling and a local strain [98]. In addition, the transitions associated with the singlet states are not accompanied by emission of photons because they are driven by the spin-orbit coupling and the electron-phonon coupling. Since this non-radiative decay process depends on the initial spin state, the spin state can be correlated with the subsequent emission of photons after optical excitations. This spin-dependent fluorescence is fully exploited to distinguish the NV

[6] The excited state has an orbital branch which mixes the spin projection. At low temperature, this level is clearly present and thus optical cycle is no longer spin-preserving. This leads to a disappearance of the ESR signal of the excited state at low temperature [9]

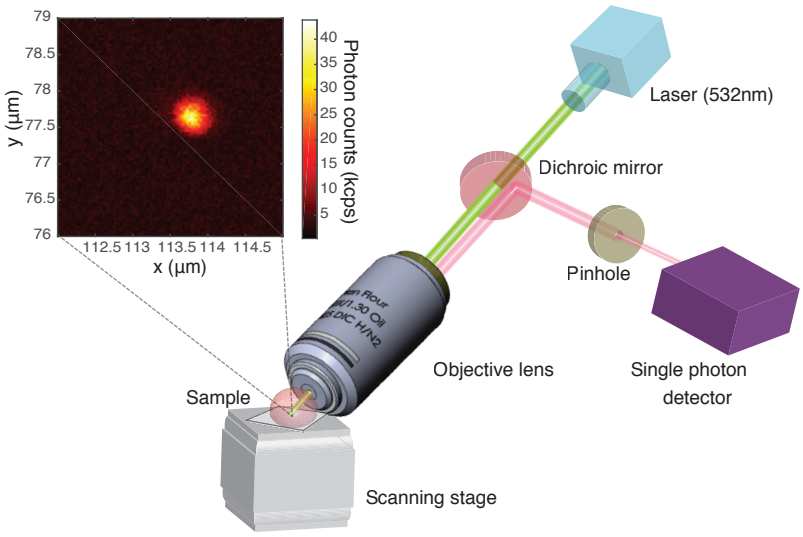

Figure 2-4: A scanning confocal microscope and its image of a single NV center. The diamond sample attached to the scanning stage is shined by the excitation laser at 532nm which is focused by the objective lens. The photoluminescence from the NV center is collected by the same objective, isolated from the excitation light by the dichroic mirror and then spatially filtered by the pinhole placed in front of the detector. In the experiment, the intensity of fluorescence (the number of photons) is measured as a function of positions of the scanning stage.

spin state in experiments.

2.3 Control of a Single NV Center

2.3.1 Optical Isolation of a Single NV Center

The optical properties of the NV center enables isolating a single NV center by fluorescence microscopy in which photoluminescence from a sample under illumination is monitored. In order to enhance the optical resolution in the sample depth direction, a confocal imaging technique in which a pin-hole to eliminate light from the off-focal plane is installed in front of a detector is employed (Fig.2-4). [7] A single NV center

[7] In confocal microscopy, the lateral resolution is also enhanced with respect to a wide-field microscopy, because the point spread function in the confocal case is the product of the point spread functions of the illumination and the detection. The lateral resolution of the confocal microscope is given by $\sim 0.61\lambda/(\sqrt{2}\mathrm{NA})$ where λ is a wavelength of the excitation light and NA is the numerical aperture of a objective while the axial resolution is given by $\sim 2n\lambda/(\mathrm{NA}^2)$ where n is the refractive index of the sample ($n = 2.4$ for diamond) [108].

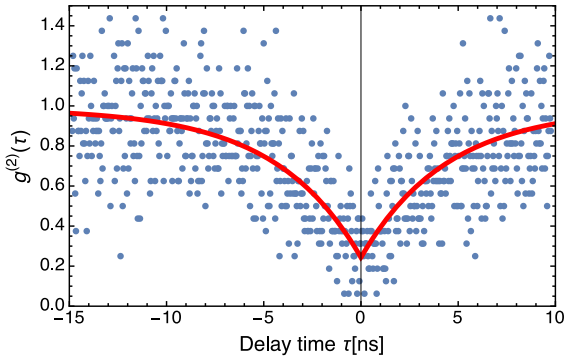

Figure 2-5: Photon correlation measurement. $g^{(2)}(0) < 1/2$ indicates that the NV center is an individual photon emitter .

can be isolated in a diamond sample with low NV center concentration. To decide if the NV center is single or not, the intensity of the fluorescence and the spot size in the confocal figures are checked. For more rigorous diagnosis, we exploit a property of a single photon source which does not emit more than one photon at a time and then we measure the correlation of a number of detected photons with a delay time τ ($g^{(2)}(\tau) = \langle N(0)N(\tau)\langle/\langle N^2(0)\rangle\rangle$) which leads to $g^{(2)}(0) < 1/2$ for the single NV center.

2.3.2 Magnetic Resonance

The ground state NV center spin can be manipulated by magnetic resonance techniques. Toward this purpose, in addition to a static magnetic field B_z along the [111] axis, an oscillating magnetic field B_1 with frequency ω is applied along the x direction. [8]

Then, the Hamiltonian of the NV center is

$$\mathcal{H} = DS_z^2 + g\mu_B B_z S_z + 2g\mu_B B_1 S_x \cos(\omega t) \tag{2.5}$$

[8]The definition of the x direction in the lab frame is arbitrary as long as defined perpendicular to the [111] axis because of the rotational symmetry of the NV center.

where the oscillating field [9] strength B_1 is much weaker than the transition frequency $(D \pm g\mu_B B_z S_z)$. In order to obtain the time evolution of this time-dependent Hamiltonian, we describe the Hamiltonian in the frame rotating with frequency ω along the quantization axis (the so-called "*rotating frame*") [10] by using the unitary transformation $U(t) = \exp(-i\omega S_z t)$:

$$\begin{aligned} \mathcal{H}_R &= U^\dagger(t)\mathcal{H}U(t) - i\frac{dU^\dagger(t)}{dt}U(t) \sim DS_z^2 + (g\mu_B B_z - \omega)S_z + g\mu_B B_1 S_x \\ &= \begin{pmatrix} D + g\mu_B B_z - \omega & \frac{1}{\sqrt{2}}g\mu_B B_1 & 0 \\ \frac{1}{\sqrt{2}}g\mu_B B_1 & 0 & \frac{1}{\sqrt{2}}g\mu_B B_1 \\ 0 & \frac{1}{\sqrt{2}}g\mu_B B_1 & D - g\mu_B B_z + \omega \end{pmatrix} \end{aligned} \tag{2.6}$$

where in the first line we neglect the fast-varying component originating from the counter rotating component of the oscillating field (Rotating wave approximation (RWA)) because, given that $\omega \ll g\mu_B B_1$, the effect is averaged out in the relevant time scale [29]. Assuming that ω is close to the resonant frequency between $|0\rangle$ and $|+1\rangle$, the transition between $|0\rangle$ and $|-1\rangle$ is neglected and the Hamiltonian $\mathcal{H}_R$ is then written as follows.

$$\mathcal{H}_R = \frac{1}{2}(D + g\mu_B B_z - \omega)\sigma_z + \frac{1}{\sqrt{2}}g\mu_B B_1 \sigma_x \tag{2.7}$$

where σ_z and σ_x are the Pauli matrices. Then, the state initially being $|0\rangle$ evolves after an evolution during τ under $\mathcal{H}_R$ becomes

$$\exp(-i\mathcal{H}_R\tau)U^\dagger(t)|0\rangle = \left\{ \cos(\Omega'_e\tau) + i\frac{\Delta}{2\Omega'_e}\sin(\Omega'_e\tau) \right\}|0\rangle - i\frac{\Omega_e}{\sqrt{2}\Omega'_e}\sin(\Omega'_e\tau)|1\rangle \tag{2.8}$$

where $\Omega'_e = \sqrt{(\Delta/2)^2 + (\Omega_e/\sqrt{2})^2}$, $\Omega_e = g\mu_B B_1$ is the Rabi frequency and $\Delta = D + g\mu_B B_z - \omega$ is the detuning from the resonant frequency. The transition probability

[9] Most of experiments of magnetic resonance employs linearly polarized fields rather than circularly polarized fields. The latter case is exactly solvable while it is difficult to generate in the experiment.

[10] The rotating frame is commonly used in the Atomic physics and NMR/ESR communities [133, 1] and is similar to the interaction picture in the Quantum mechanics which describes the Hamiltonian in the frame of the non-perturbative part. [126].

$p(\tau)$ is then given by

$$\begin{aligned} p(\tau) &= |\langle 1| U(t) \exp(-i\mathcal{H}_R\tau) U^\dagger(t) |0\rangle|^2 \\ &= \frac{1}{1+(\frac{\Delta}{\sqrt{2}\Omega_e})^2} \sin^2\Big(\sqrt{(\frac{\Delta}{2})^2+(\frac{\Omega_e}{\sqrt{2}})^2}\tau\Big). \end{aligned} \tag{2.9}$$

The transition probability is maximized on resonance $\Delta = 0$ and suppressed when far off-resonant ($\Delta \gg \Omega$). Thus, the smaller driving power (Ω_e) yields the narrower excitation profile and vice versa. This property is exploited for the selective excitation when the NV spin has several resonant frequencies due to the coupling to other electronic or nuclear spins.

2.3.3 Optically Detected Magnetic Resonance

In order to determine the resonance line, we employ continuous wave optically detected magnetic resonance (CW-ODMR). In the CW-ODMR measurement, the fluorescence is measured while a microwave (MW) field is continuously applied during the optical excitation at 532 nm. (Fig.2-6(b)). When the MW field is on resonance, the $m_s = 0$ state is mixed with the $m_s = \pm 1$ states, resulting in a reduction of the fluorescence intensity. However, because of the overlap of the excitation and the detection processes, the linewidth is broadened ($\sim$ 10MHz) by the optical excitation and long excitation duration (few ms) and the sensitivity is limited [145]. To sharpen the linewidth, the excitation process is isolated from the detection process. In addition, to enhance the selectivity of the resonance lines, a pulse-shaped MW field with a weak driving power is employed [39]. This pulsed optically detected magnetic resonance (Pulsed-ODMR) technique attains much sharper line-width (few hundreds kHz) depending on the power of the MW field and the best contrast is obtained when the pulse length corresponds to a π rotation of the NV spin.

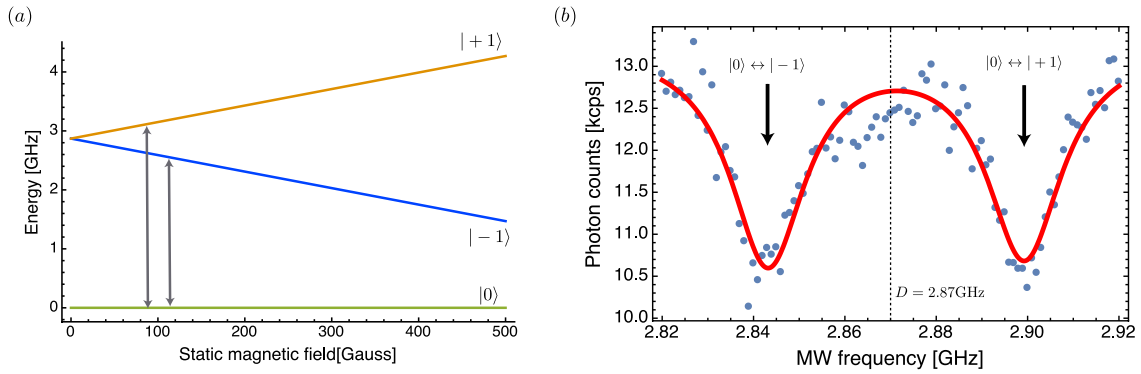

Figure 2-6: (a) Energy level of the ground state of the NV center. The ground state is triple and the degeneracy is lifted up by the zero field splitting ($D \sim 2.87$ GHz). By applying a static magnetic field along the crystal axis ([111]), the degeneracy between the $m_s = \pm 1$ sublevels is also lifted up due to the Zeeman splitting. The gray arrows show the allowed transitions in electron magnetic resonance ($\Delta m_s = \pm 1$). (b) Continuous-wave optically detected magnetic resonance (CW-ODMR) under the magnetic field ($\sim$ 10 G). The two peaks correspond to the transitions between $|0\rangle$ and $|\pm 1\rangle$ sublevels and the splitting originates from the Zeeman interaction with the external magnetic field ($\sim 2\gamma_e B$). The spetcral line is fitted by the Lorenzian curve.

2.3.4 Rabi Oscillations

After the resonant frequency is identified, the spin state can be coherently manipulated by the oscillating MW field at the resonant frequency. By sweeping the length of the resonant MW pulse, Rabi nutations between $|0\rangle$ and $|\pm 1\rangle$ states can be observed (Fig.2-7-(b)). From Eq.(2.8), a resonant MW pulse with a duration τ transforms the initial state $|0\rangle$ to superposition state of the two eigenstates $\cos(\frac{\Omega_e \tau}{\sqrt{2}})|0\rangle - i \sin(\frac{\Omega_e \tau}{\sqrt{2}})|1\rangle$, where Ω_e is the Rabi frequency describing the coupling strength of the spin to the MW field. [11] On resonance ($\Delta = 0$) yielding $\mathcal{H}_R = \frac{\Omega_e}{\sqrt{2}}\sigma_x$, the operation is described by $R_\theta = \cos\theta\sigma_z - i \sin\theta\sigma_x$ where $\theta = \frac{\Omega_e}{\sqrt{2}}\tau$. Therefore, by adjusting the duration of the resonant MW pulse, the rotation around the x (or y) axis can be implemented.

[11] Dynamics of a two level system can be geometrically understood in the vector model in the Bloch sphere. In this model, transformation of the Rabi nutations corresponds to a rotation by an angle $\theta(= \Omega_e \tau)$ around an axis in $x - y$ plane. A rotation axis is called a "phase" of a pulse which can be tuned by the phase of the MW field. The phase of the first pulse can be chosen arbitrarily and a phase needs to be considered only when more than two pulses are associated.

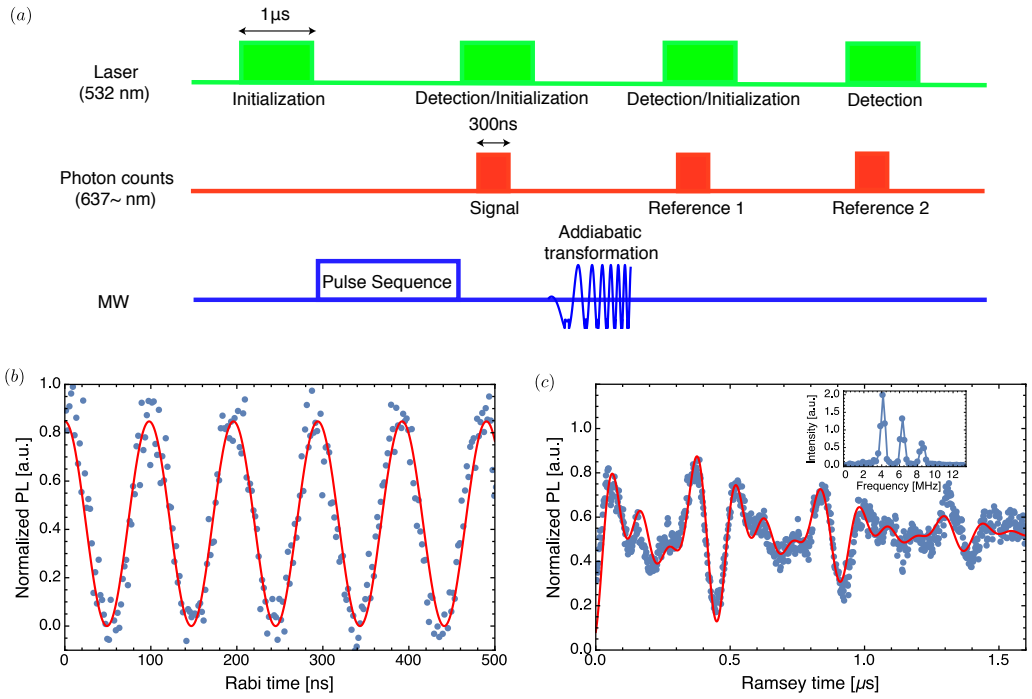

Figure 2-7: (a) Experimental procedure of pulse electron spin resonance. In each experimental run, in an addition to a state after microwave (MW) pulses (S), the PL from two eigenstates $|0\rangle(S_0)$ and $|+1\rangle(S_1)$ are also measured and used to normalize the data by $(S-S_1)/(S_0-S_1)$ which directly indicates the population at the $m_s=0$ state. We transform the initial state $|0\rangle$ to the $|+1\rangle$ state by changing the frequency of MW at the adiabatic rate. (b) Rabi nutations of a single NV center. The NV spin is continuously driven by the MW. It shows a coherent oscillation between $|0\rangle$ and $|+1\rangle$. (c) Ramsey fringes of the single NV center. The MW sequence is $\pi/2-\tau-\pi/2$ where τ is the free evolution time (Ramsey time). The NV center is coupled to a thermally mixed nitrogen nuclear spin (I=1) which shifts the resonance line by the three-fold hyperfine fields, as it can be confirmed as the three peaks in Fourier spectrum of this signal (inset figure).

2.3.5 Ramsey Interferometry

More precise determination of the resonant frequency is attained by Ramsey interferometry [115]. In this measurement, we first create a superposition state of the NV center, which subsequently evolves under the Hamiltonian in the rotating frame and then measure the "coherence" [12] of the evolved state. The experimental procedure of the Ramsey interferometry is $\pi/2-\tau-\pi/2$. The last $\pi/2$ pulse is to convert

[12]The coherence in quantum mechanics refers to a relative phase among distinct eigenstates. For instance, in two-level system, a superposition state is given by $\alpha|0\rangle+\beta e^{-i\theta}|1\rangle$ where $\alpha,\beta\in\mathcal{C}$ and θ is the "coherence" of this state.

the coherence into population difference which can be optically detected. Given the frequency of the MW pulses, $\omega = D + g\mu_B + \Delta$ with a detuning Δ , the signal $S(\tau, \Delta)$ is calculated to be

$$S(\tau,\Delta) = |\langle 0| U^{\dagger}(\tau) R_{\pi/2} e^{-i\Delta(\mathbf{1}/2+\sigma_z)\tau} R_{\pi/2} U(\tau) |0\rangle]^2 = \frac{1}{2}\Big(1 - \cos(\frac{\Delta\tau}{2})\Big) \qquad (2.10)$$

The measured signal, called the Ramsey fringes in atomic physics or the free induction decay in EPR/NMR experiments, oscillates at the detuning Δ. Therefore, the Fourier transform of the Ramsey fringes directly indicates the detuning from the true resonant frequency. In addition, the Ramsey fringes show the loss of coherence (dephasing) by interactions with its magnetic environment. Dephasing is induced due to a inhomogeneous magnetic field which shifts resonance line of the NV center by $\delta(t)$. For example, in a typical experiment with the NV center, we repeat the experiment 5×10^5 times. In each experiment run, the NV center is subjected to an additional static local field b which dynamically changes between experiments. In type IIa diamond, which is devoid of substitutional nitrogen impurites, this inhomogeneous noise b is mainly attributed to carbon nuclear spins in the lattice which rearrange their configuration slower than a typical one experiment run time but faster than the whole measurement time. Let b follow the Gaussian distribution with a zero mean and a standard deviation σ, the measured signal $S(\tau)$ is given by the statistical average of the Eq. 2.10 over δ:

$$\begin{aligned} \mathcal{S}(\tau) &= \frac{1}{\sqrt{2\pi}\sigma} \int db S(\tau, \Delta + b) e^{-\frac{b^2}{2\sigma^2}} \\ &= \frac{1}{2} - \frac{1}{2}\langle \cos(\frac{(b+\Delta)t}{2}) \rangle = \frac{1}{2} - \frac{1}{2} e^{-\sigma^2\tau^2/4} \cos(\frac{\Delta\tau}{2}). \end{aligned} \qquad (2.11)$$

The calculation is simplified by using a cumulant expansion [85]. [13] Thus, the Ramsey fringes decays in a time scale $T_2^\star = 4/\sigma^2 \sim 2 - 3\mu s$.

2.4 Nuclear Spins in Diamond

There are mainly two nuclear species with spins in diamond (Table 2.1). One is a carbon atom in the lattice and ^{13}C with 1.1 % natural abundance has a spin 1/2. The other is a nitrogen atom and ^{14}N and ^{15}N have spin 1 and spin 1/2 respectively. The nuclear spin can be distinguished by a hyperfine coupling with the NV center which is measured by the pulsed-ESR measurements.(Fig.2-8)

	Natural abundance (%)	Total spin number	Gyromagnetic ratio (kHz/G)
^{14}N	99.63	1	0.307
^{15}N	0.37	1/2	-0.431
^{13}C	1.1	1/2	1.07

Table 2.1: Isotopes with nuclear spins in diamond.

The ^{13}C nuclear spin spreads randomly over the diamond lattice. The ^{13}C in the vicinity of the NV center is strongly coupled [26] and thus can be coherently controlled [138], while others generate a random noise at the site of the NV center, leading to decoherence [102, 105]. The coupling nature between ^{13}C nuclear spins and the NV center depends on the location on the lattice and thus to find a ^{13}C with a desired coupling strength is probabilistic. On the other hand, the nitrogen is a constituent of the NV center and coupled to the electronic spin in a well-defined way. Especially, ^{14}N with 99.6% natural abundance is mostly likely found in the NV center. In the following section, we describe how to control a single ^{14}N nuclear spin.

[13] Remind that the characteristic function $\langle e^{i\xi} \rangle$ of the Gaussian variables ξ is expand by only its first and second Cumulants:

$$\langle e^{i\xi} \rangle = \exp\Big(i\langle \xi \rangle - \frac{\langle \xi^2 \rangle - (\langle \xi \rangle)^2}{2} \Big). \tag{2.12}$$

Thus, by taking a real part of the both side, we obtain: $\langle \cos \xi \rangle = e^{-\frac{\sigma^2}{2}} \cos(i\langle \xi \rangle)$.

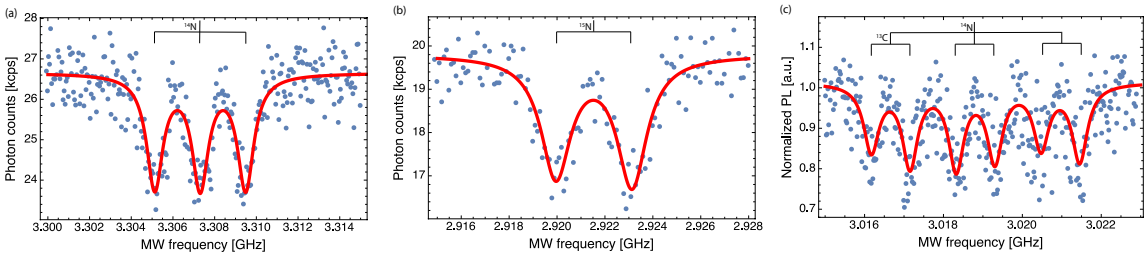

Figure 2-8: Hyperfine structures of the pulse-CW ESR spectrum. (a)NV-^{14}N (b)NV-^{15}N (c)NV-^{14}N-^{13}C

2.5 Control of a Single Nuclear Spin

2.5.1 The Nitrogen Nuclear Spin

The nitrogen atoms are main impurities in type I diamond and form several kinds of point defects (e.g. N(P1 (or C) center), N-N(A center)).

		$A_\parallel$ [MHz]	$A_\perp$ [MHz]	Q [MHz]	Reference
^{14}N	GS	-2.162±0.002	-2.70±0.07	-4.945 ±0.005	[134, 42]
	ES	(±)40	(±)40	-	[136]
^{15}N	GS	3.03 ± 0.03	3.65 ± 0.03	NA	[?]
	ES	(±)61	(±)61	NA	[46]

Table 2.2: Hyperfine structure constants of the nitrogen nuclear spin. The constants are well-determined in the ground state except the transverse coupling of ^{15}N which differs in experiments [46, 42, 114]. The accurate constants in the excited states are still not available, but the strength is confirmed to be much stronger than in the ground state due to the fact that the excited state has the a_1' orbital which extends over the nitrogen atom site, leading to an enhancement of the Fermi contact term of the hyperfine constant.

The nitrogen lies adjacent to the vacancy site and constitutes the electronic structure of the NV center. The ^{14}N has a spin 1 and since it exists in the vicinity of the NV center, it interacts strongly (MHz) with the NV spin via a hyperfine coupling. The coupling can be exploited to control the nitrogen nuclear spin. The Hamiltonian of the system composed of a single nitrogen nuclear spin and the NV spin (^{14}N-NV) is given by

$$\mathcal{H} = \Delta S_z^2 + \gamma_e B S_z + Q I_z^2 + \gamma_n B I_z + A_\parallel S_z I_z + A_\perp (S_x I_x + S_y I_y), \tag{2.13}$$

where S and I are the electron and nuclear spin-1 operators respectively. $Q = -4.945$ MHz is the nuclear quadrupole interaction which is the interaction of a quadrupole moment of the nuclei with the electric field gradient of the electrons, leading to lift the degeneracy of the nuclear spin levels. This is the leading term of the nuclear spin and quantizes the nuclear spin along the [111] direction which is then chosen as the quantization axis of the nuclear spin. The two spins are coupled by an isotropic hyperfine interaction with $A = -2.15$ MHz and a transverse component $B = -2.62$ MHz. [14] The hyperfine coupling is mainly due to the Fermi contact term and thus subjected to the electronic spin density at the nitrogen atom site. Thus, it changes significantly in the excited state of the NV spin (Table.2.2). A magnetic field B is applied along the NV crystal axis [111] to lift the degeneracy of the $m_s = \pm 1$ level, yielding the electron and nuclear Zeeman frequencies $\gamma_e B$ and $\gamma_n B$.

2.5.2 Polarization of the Nuclear Spins

Initializing nuclear spins is a prerequisite for using them as quantum resources. The polarization of nuclear spins has been also studied as one of the central problems in nuclear magnetic resonance because it limits the detection sensitivity. Dynamic nuclear polarization (DNP) is one approach to enhance the polarization of nuclear spins by the larger polarization of electronic spins, which is transferred to the nuclear spins. Similarly, here, we take advantage of the optically polarized NV spin to polarize the nearby nitrogen nuclear spin. The exchange of the spin angular momentum (flip-flop transition) can be driven by the transverse hyperfine coupling. However, it is forbidden because of the large energy mismatch between the electronic and nuclear spin. Thanks to the zero-field splitting of the NV spin yielding the transition frequency

[14] In this thesis, we define a sign of D, γ_e positive while they are negative if we stick to the sign of physical constants ($e < 0$). Then, γ_n is assigned a negative sign. The sign of $A_{\parallel,\perp}$ and Q are confirmed to be the same as that of γ_n [23, 43] and thus assigned a negative sign in this thesis.

between $m_s = 0, -1$, $D - \gamma_e B$, setting a magnetic field close to $D_e/\gamma_e \sim 510$ G decreases the energy splitting and thus the rate of the flip-flop transition can be enhanced. While the flip-flop transition alone can not achieve polarization, by preparing the polarized NV state, the directional transfer process takes place. In our experiment, we use the hyperfine coupling in the excited state because the coupling strength is much larger than in the ground state due to enhancement of the Fermi contact term and in addition the polarization process is isolated from operations of controls of the NV spin and the nuclear spin performed in the ground state. The Hamiltonian of the excited state of the NV spin and the nuclear spin at zero strain is described by

$$\mathcal{H}_e = D_e S_z^2 + \gamma_e B S_z + A_\parallel S_z I_z + A_\perp (S_x I_x + S_y I_y) \tag{2.14}$$

where all of orbital-related interactions are thermally mixed and averaged out and the nuclear Zeeman interaction and the quadrupole interactions are negligible. We consider only the $m_s = 0, -1$ electronic manifolds which can be close to the level crossing. Due to the transverse coupling, eigenstates of the Zeeman interactions are mixed:

$$|\xi_+\rangle = \cos\theta_+ |0,-1\rangle + \sin\theta_+ |-1,0\rangle \tag{2.15}$$

$$|\xi_-\rangle = \sin\theta_- |0,-1\rangle + \cos\theta_- |-1,0\rangle \tag{2.16}$$

$$|\eta_+\rangle = \cos\phi_+ |0,0\rangle + \sin\phi_+ |-1,1\rangle \tag{2.17}$$

$$|\eta_-\rangle = \sin\phi_- |0,0\rangle + \cos\phi_- |-1,1\rangle \tag{2.18}$$

where

$$\theta_\pm = \mathrm{Tan}^{-1}\left[\frac{-2A_\perp}{(D_e - \gamma_e B - A_\perp) \pm \sqrt{(D_e - \gamma_e B - A_\perp)^2 + 4A_\perp^2}}\right] \tag{2.19}$$

$$\phi_\pm = \mathrm{Tan}^{-1}\left[\frac{-2A_\perp}{(D_e - \gamma_e B + A_\perp) \pm \sqrt{(D_e - \gamma_e B + A_\perp)^2 + 4A_\perp^2}}\right]. \tag{2.20}$$

The state mixing is maximized in the vicinity of the level anticrossing where $D_e - \gamma_e B \sim 0$ (at 510G).(See Fig.2-10) Due to the intersystem crossing process, the NV

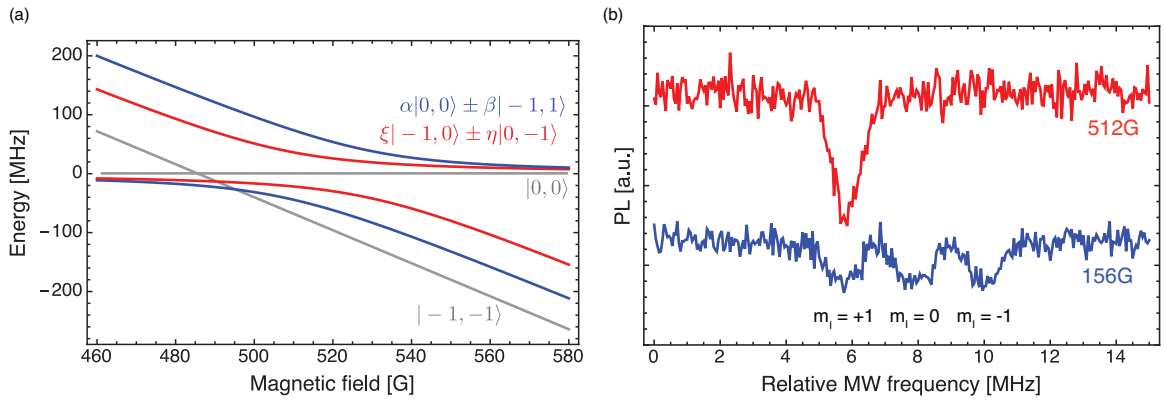

Figure 2-9: (a) The excited state of the NV-N system. The states connected by the transverse hyperfine coupling avoid crossing. The transition between this coupled states is strong in the vicinity of the anti-crossing point. (b) The Pulsed-CW spectrum of the NV center. At low field, three peaks of the ESR signal indicates the thermally mixed nitrogen nuclear spin. At magnetic field close to ESLAC, the nuclear spin is polarized to $m_I = +1$ state.

spin is populated in $m_s = 0$ and when excited by the laser its spin state is preserved. Assume for example that the state $|0,-1\rangle$ is prepared in the excited state, due to the hyperfine coupling, a transition to the $|-1,0\rangle$ state can occur with the transition probability:

$$\begin{aligned} P_{-1\to 0}(\tau, B) &= |\langle -1,0| e^{-i\mathcal{H}_e \tau} |0,-1\rangle|^2 \\ &= |e^{-i\xi_+\tau}\cos^2\theta_+ \sin^2\theta_+ + e^{-i\xi_-\tau}\cos^2\theta_- \sin^2\theta_-|^2 \\ &= \cos^2\left(\frac{\sqrt{4A_\perp^2 + (D_e - \gamma_e B)}\tau}{2}\right)\frac{A_\perp^2}{A_\perp^2 + (D_e - \gamma_e B)^2/4}. \end{aligned} \quad (2.21)$$

This process progresses incoherently since spontaneous emission and optical driving occur in the similar time scale (∼MHz). $P_{0\to+1}(B)$ can be obtained in the same way. The dependence of the transition probability on the static magnetic field is experimentally confirmed by the lattice relaxation of the nitrogen nuclear spin T_{1n} which is indeed governed by the flip-flop transition in the excited state during the optical excitation [111]. The transition rate is maximized when a static field is close to the level crossing ($B \sim D_e/gamma_e$). This transition process in the excited state continues until the nuclear spin state reaches the $m_I = +1$ state. Thus, after a long enough optical excitation, the NV-N system can be polarized into the $|0,+1\rangle$ state.

The polarization of the nitrogen nuclear spin can be confirmed by pulsed-ODMR measurements (See fig.2-10(b)). This technique can be also used to polarize other close-by carbon nuclear spins [147] and electronic spins (P1 centers) [64]. Also, the flip-flip transition occurs from $m_s = 0$ state to $m_s = -1$ state which then decays via the singlet state without an emission of photons and enhances the contrast of the NV spin state [136]. On the other hand, population exchange with the nuclear spin renders the relaxation process of the NV spin correlated with the nuclear spin state, leading to a optical contrast among the nuclear spin states. This property can be exploited to measure the nuclear spin state later (see chapter 4).

2.5.3 Coherent Control of the Nuclear spin

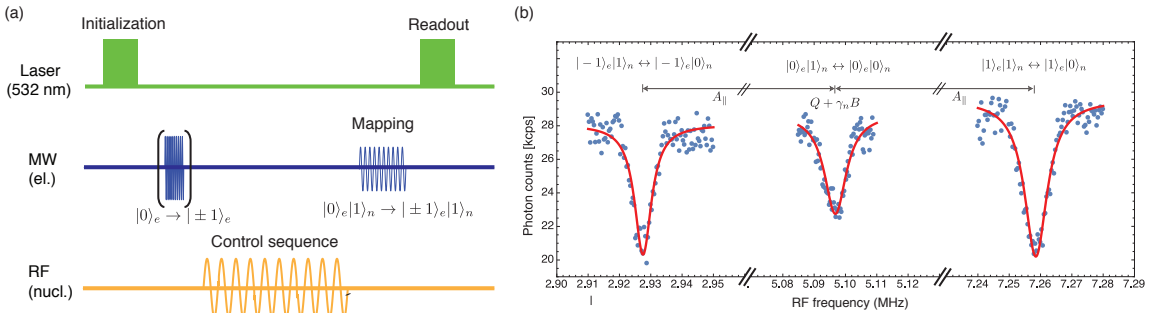

Figure 2-10: (a) Experimental sequence used to measure the nuclear ^{14}N resonance line. The first MW π pulse is used to drive the electronic spin state to the desired manifold. The second MW π pulse is applied conditioned on the nuclear spin state, leading to map the nuclear spin state to the electronic spin state which is then optically detected. (b) Pulsed-ODMR for the nuclear ^{14}N spin. The splitting is due to the hyperfine coupling of the NV center.

Fast and reliable control of the nuclear spin is of great importance to use it as a quantum memory or an ancillary qubit for quantum algorithms. The most common way is to drive the spin by a resonant field by means of the nuclear magnetic resonance (NMR) technique [133, 128]. An alternative scheme is to use the the electronic spin as a spin actuator to drive the coupled nuclear spin via the anisotropic hyperfine interaction [70] or to resort to the Landau-Zener (LZ) transition at the anti-level crossing level [45]. For the nitrogen nuclear spin, since it does not have anisotropic

hyperfine coupling and is strongly quantized by the quadrupole interaction, it does not possess the resolvable anisotropic interaction at the aligned magnetic field. Thus, it can not be driven by exploiting the interaction between the NV spin and the nuclear spin [70]. Also, the LZ transition requires the specific setting in the magnetic field and is not flexible. Here, we control the nitrogen nuclear spin by the direct radio-frequency (RF) field driving because the transition probability is significantly enhanced by the transverse hyperfine coupling [23] (see Appendix). The experimental procedure of the control of the nuclear spin is found in Fig.2-10-(a). Firstly, the nuclear spin state can be initialized to the state $|0\rangle_e |+1\rangle_n$ by optical excitation at close to the LAC level. Due to the hyperfine coupling (2.15 MHz) which is much stronger than a typical driving rate (100∼10 kHz), the nuclear spin has a different resonant frequency in each electronic manifold which can not be addressed at the same time. To read out the nuclear spin, we map the nuclear spin state into the electronic spin state by the selective MW pulse, even though there is the optical contrast among the nuclear spin states. In order to identify the resonant frequency, we employ the pulsed-ODMR measurement in which a frequency of a RF pulse is swept while the length of the pulse is fixed. (See Fig.2-10(b)) Once the resonant frequency is identified, we measure the nuclear Rabi oscillation (Fig.2-11).

2.5.4 Coherence Property of the Nuclear Spins

The ^{14}N nuclear spin has the small gyromagnetic ratio with respect to the electronic spin ($\gamma_n/\gamma_e \sim 1/9000$) and thus interacts weakly with its magnetic environment, leading to a long coherence time. However, it is coupled strongly to the NV spin via the hyperfine interaction ($A_\parallel = 2.15$ MHz) and the NV center rearranges its spin state by the spin lattice relaxation time T_{1e}(∼ few ms), which limits the coherence time of the nitrogen nuclear spin. The couplings to the NV spin and its relaxation creates a random telegraph noise acting on the nuclear spin. Because of the strong coupling ($A_\parallel T_{1e} > 1$), the random telegraph noise has Markovian nature [22, 24, 48, 11] and

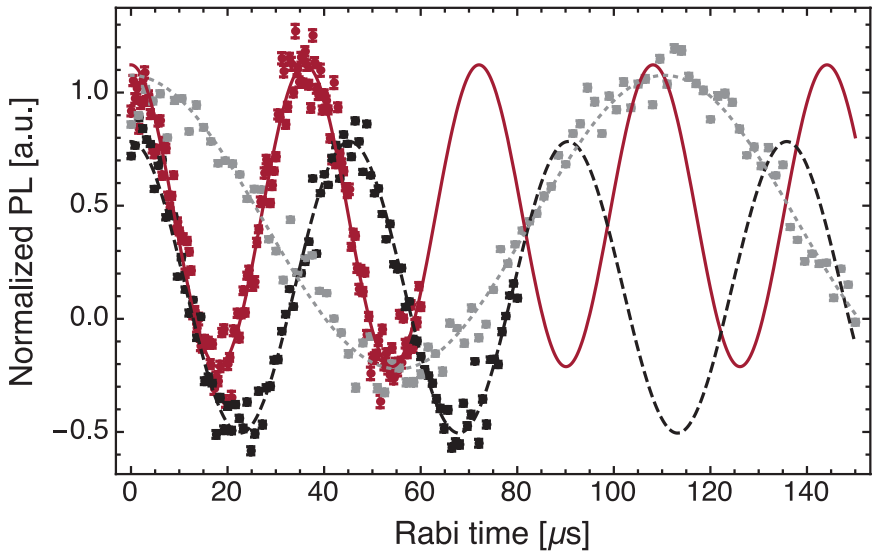

Figure 2-11: ^{14}N Rabi oscillations at $B = 450$G, $B_1 \approx 3.3$G in the three NV manifold (Red, solid line $m_s = 0$. Black, dashed line, $m_s = -1$. Gray, dotted line $m_s = +1$). Here the dots are the experimental results, while the lines are fitting curves of cosine oscillations. The different baseline of the $m_s = -1$ curve is due to small differences in the fluorescence emission of different nuclear manifolds [73]. The difference in rabi oscillation can be explained by considering Rabi enhancement effects (see Appendix).

thus conventional dynamical decoupling schemes (e.g., spin echo) are not effective. [15]

[15]The similar case is found in the phosphorus nuclear spin ($I = 1/2$) in silicon. The coherence time of the phosphorus nuclear spin is limited by the lattice relaxation of the donor electronic spin ($S = 1/2$) $T_{2n} = 2T_{1e}$ [107]. The nuclear-electronic interaction is eliminated by ionizing the donor electron and the coherence time is significantly extended [125]. For the NV center, unlike Si:P system, the ionized state NV^0 still possesses a spin ($S = 1/2$) and interacts with the nitrogen nuclear spin and thus this ionization technique is not directly applicable. However, by switching the charge state of the NV center much faster than a coupling between the NV spin and a distant ^{13}C nuclear spin in the motional averaging regime in NMR, the coupling is effectively decoupled [100].

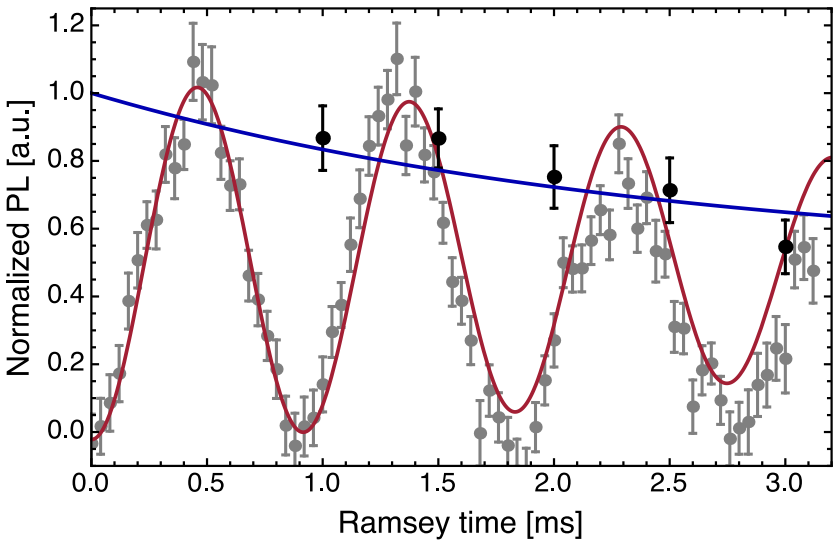

Figure 2-12: ^{14}N nuclear Ramsey fringes. We employ the sequence $\pi/2 - \tau - \pi/2$, where τ is a free evolution time. We measure a dephasing time of the nuclear spin $T_{2n}^{\star} = 3.2$ ms, which is limited by the NV electronic spin lattice relaxation process ($T_1 = 4.5$ ms, filled black circles and blue line)

Chapter 3

Continuous Dynamical Decoupling Magnetometry

3.1 Introduction

Sensing magnetic fields with nanoscale resolution is a pivotal issue in biological science and materials science [10]. Detection of single atoms would enable unfolding the structure and the interaction of proteins, which can't be crystallized for X-ray analysis.

Magnetic resonance imaging (MRI) is a widely used technique to detect a magnetic field with resolution down to micrometer range. In MRI, to attain better signal-to-noise ratio, a larger sample volume is required and thus, the resolution is fundamentally limited by the sensitivity and can't be enhanced into the realm of nano-scale sensing.

A precursor in nano-scale magnetometry is magnetic resonance force microscopy (MRFM) in which a probe (micro-cantilever) is scanned over a sample and a magnetic field is read out by the detection of mechanical oscillations of a micro-cantilever [123, 72]. The architecture of the scanning probe enables positioning close to the field to be detected and thus achieves better resolution (90 nm) than the conventional MRI and detection of single electronic spins has been achieved [123, 72]. However, MRFM requires vacuum conditions at low temperature (mK) and thus can't be adapted to

ambient conditions of biological samples.

As an alternative nano-scale probe, solid-state qubits have emerged as promising quantum sensors, as they can be fabricated in small volumes and brought close to the field to be detected. Inspired by optically detected magnetic resonance experiment on single spins [155, 154], a single molecule with fluorescence property was proposed as a magnetic field probe [129, 25]. Most notably, nitrogen-vacancy (NV) centers in nano-crystals of diamond [75] have been applied for high sensitivity detection of magnetic [139, 101, 7] and electric fields [38] and could be used either as nano-scale scanning tips [96] or even in-vivo due their small dimensions and low cytotoxicity [103]. Unfortunately, solid-state qubits are also sensitive probes of their environmental noise [18, 8, 156] and this leads to rapid signal decay, which limits the sensor interrogation time and thus its sensitivity. In this chapter, we consider magnetometry using the NV center spin as a probe and introduce a novel technique to sense constant (DC) and alternating (AC) magnetic field.

3.2 Sensitivity of Single Spin Magnetometry

Here, we briefly describe the sensitivity of NV-based magnetometry using the NV center. A static magnetic field to be estimated (δB) shifts the resonant frequency by Zeeman energy ($\delta\omega = \gamma_e \delta B$). The standard way to detect the detuning of the resonant frequency is Ramsey interferometry, which is widely implemented in atomic or molecular systems for precision measurement of time [122]. First, prepare a superposition state $(|0\rangle + |1\rangle)/\sqrt{2}$ which is then evolved into $|\Psi(\delta\phi)\rangle = (|0\rangle + e^{-i\delta\phi}|1\rangle)/\sqrt{2}$ where $\delta\phi = \delta\omega\tau$ with evolution time for Ramsey interferometry τ. Thus, the magnetic field is estimated by measuring the phase of the NV spin. The readout of the NV spin state is done by the measurement of the fluorescence with finite contrast and collection efficiency, which can be modeled by the measurement operator

$$M = n_0 |0\rangle\langle 0| + n_1 |1\rangle\langle 1| \tag{3.1}$$

where $n_{0,1}$ indicates the number of photons arriving at the detector during the measurement time t_M. $n_{0,1}$ follows the poisson distribution : $\langle n_{0,1}\rangle = N_{0,1}, \langle n_{0,1}^2\rangle - \langle n_{0,1}\rangle^2 = N_{0,1}$, where $N_{0,1}$ is the average photon number. In order to reduce the shot noise, the measurement needs to be repeated N times, which reduces the uncertainties by a factor $1/\sqrt{N}$. Letting $\rho(\delta\phi) = R_{\pi/2}\,|\Psi(\delta\phi)\rangle\,\langle\Psi(\delta\phi)|\,R_{\pi/2}^{\dagger}$ be a state to be measured, the signal is given by

$$S(\delta\phi) = \left\langle \mathrm{Tr}\Big[M\rho(\delta\phi)\Big]\right\rangle = \frac{1}{2}(N_0+N_1) + \frac{1}{2}(N_1-N_0)\cos(\delta\omega\tau-\theta). \tag{3.2}$$

In order to maximize the sensitivity, we shift the phase of the last $\pi/2$ pulse by $\theta = \pi/2$ with respect to the first pulse. The measurement entails spin projection noise and thus the uncertainty of the measurement is given by

$$\begin{aligned}\Delta S(\delta\phi)^2 &= \left\langle \mathrm{Tr}\Big[M^2\rho(\delta\phi)\Big]\right\rangle - \left\langle \mathrm{Tr}\Big[M\rho(\delta\phi)\Big]^2\right\rangle \\ &= \frac{1}{4}\frac{1}{\sqrt{N}}\left\langle (n_1-n_0)^2\right\rangle \cos^2(\delta\omega\tau).\end{aligned} \tag{3.3}$$

The minimum detectable phase $\delta\phi_{\min}$ is obtained by comparing the displacement of the signal $S(\delta\phi)$ from $S(0)$ with uncertainties of measurement as follows

$$\begin{aligned}S(\delta\phi_{\min}) - S(0) &\sim \left.\frac{\partial S}{\partial\phi}\right|_{\phi=0}\delta\phi_{\min} \\ &= \frac{1}{2}\Delta S(\delta\phi) + \frac{1}{2}\Delta S(0) \sim \Delta S(0)\end{aligned} \tag{3.4}$$

where we assume that $S(\phi)$ has a non-zero first derivative and $\delta\phi$ is small enough to be approximated in the linear regime and, since the leading order of the uncertainty of the signal is $\sim \delta\phi^2$, it holds true that $\Delta S(0) \sim \Delta S(\delta\phi)$. Thus, the minimum detectable field is given by

$$\delta B_{\min} = \frac{1}{\gamma_e\sqrt{\tau}}\frac{\Delta S(0)}{\frac{\partial S}{\partial\phi}|_{\phi=0}} = \frac{1}{\gamma_e\tau C\sqrt{N}} \tag{3.5}$$

where C represents inefficiency associated with optical measurements such as shot noise, finite contrast, and collection efficiency : $1/C = \sqrt{1 + (N_0 + N_1)/(N_0 - N_1)^2}$. The large mismatch of refractive index between air and diamond ($n = 2.4$) leads to total internal reflection of fluorescence, resulting in a poor collection efficiency ($< 10\%$) even with a large N.A. (=1.49) objective lens. The collection efficiency can be further improved by fabricating nano-wires or solid immersion lens yielding better efficiency ($> 40\%$).[1] Also, the contrast can be enhanced by using a close-by nuclear spin or mapping the spin state to different charge states of the NV center. To evaluate the sensing method, we define the sensitivity

$$\eta = \delta B_{\min} \sqrt{T_{\text{tot}}} = \frac{1}{\gamma_e C \sqrt{\tau}} \sqrt{1 + \frac{\tau_d}{\tau}} \tag{3.6}$$

where $T_{\text{tot}} = N(\tau + \tau_d)$ is the total measurement time consisting of the interrogation time τ and the dead time τ_d, which is broken into the detection and initialization time. The sensitivity can be improved by increasing the interrogation time τ which is, however, limited by the decoherence of the spin probe. The probe coherence typically decays as $e^{-(\tau/T)^n}$ where T is the spin decoherence time and n depends on noise nature and filtering profile of control schemes [13, 33]. To optimize the sensitivity, the compromise between the gain by reducing the shot noise $1/\sqrt{\tau}$ and the loss by decreasing the contrast of signal due to the decoherence $e^{-(\tau/T)^n}$ needs to be considered and the best sensitivity is attained when $\tau = (\frac{1}{2n})^{1/n} T$. Thus, the decoherence time restricts the measurement time with the best sensitivity and this constraint makes Ramsey sequence less attractive because of short coherence time.

3.3 Continuous Dynamical Decoupling

Dynamical decoupling (DD) methods [20, 144, 142, 81, 13, 4] have been adopted to prolong the coherence time of the sensor qubits [139, 32, 8, 113, 84]. The principle of DD schemes rests on the spin echo sequence, which refocuses unwanted phase

[1] For ensemble measurement, the side collection scheme is also employed to enhance the collection efficiency ($anincreaseof \sim 47\%$).

accumulation due to a slow bath by reversing the system evolution with control pulses. More complex DD sequences can in principle extend the coherence time indefinitely, by increasing the number of pulses. Although DD techniques prevent measuring constant, DC fields, they provide superior sensitivity to oscillating AC fields, as they can increase the sensor coherence time by orders of magnitude. The sensitivity is maximized by carefully matching the decoupling period to the AC field; conversely, one can study the response of a decoupling scheme to fields of various frequencies, thus mapping out their bandwidth. In practice, however, a large number of imperfect, finite-width pulses provokes the accumulation of error and degrades DD performance [81, 80, 149]. Thus, the refocusing power of pulsed DD techniques is ultimately limited by pulse errors and bounds in the driving power.

Here we investigate an alternative strategy, based on continuous dynamical decoupling (CoDD), that has the potential to overcome these limitations. CoDD has been first introduced in the context of NMR to mitigate pulse errors [17, 16] and it has then led to many schemes, such as composite pulses [130, 89], dynamically corrected gates [82] and optimized modulations [28, 41]. In general, phase and amplitude modulation of the continuous driving allows great flexibility and CoDD can achieve high decoupling power [52].

We consider the problem of measuring a small external field, coupled to the sensor by the Hamiltonian $\mathcal{H}_b = \gamma b(t) S_z$, where S_z is the spin operator of the quantum sensor. For example, $b(t)$ can be an external magnetic field and γ the spin's gyromagnetic ratio. We use the sensitivity introduced in the previous section as a metric to compare pulsed and continuous DD schemes and show how CoDD can offer an advantage for some noise regimes. We consider two type of magnetic fields such as DC and AC fields. For sensing DC field, we compare the Ramsey sequence with two CoDD scheme (constant continuous driving(C) and Rotary Echo). For sensing AC field, we consider two CoDD schemes, Rabi driving (either constant continuous driving (C) or spin locking (S)) and Rotary Echo (RE) [135, 2, 88], as their periodicity allows an easier use for AC magnetometry (see Fig. 4-2); we further compare these schemes to the simplest pulsed DD scheme, periodic dynamical decoupling (PDD).

3.3.1 Rotary Echo

The rotary echo (RE) sequence was originally introduced in NMR in order to mitigate an inhomogeneity of the driving field [135]. The RE sequence consists of a continuous on-resonance driving field of constant amplitude Ω and phase inverted at periodic intervals (see Fig. 4-2). RE is parametrized by the angle $\vartheta = \Omega T/2$, where T is the sequence period. While RE has been specifically designed to refocus errors in the driving field, for $\vartheta = 2\pi k$ the sequence also refocuses dephasing noise, with performance depending on both k and the Rabi frequency Ω.

3.3.2 Dynamics under Rotary Echo

We consider the evolution of a sensor qubit under a sequence of θ-RE and in the presence of an external magnetic field $b(t)$ and then show how it can be applied for other continuous decoupling magnetometry schemes. The Hamiltonian in the lab frame is given by

$$\mathcal{H}(t) = \Omega \mathbb{SW}(t) S_x + \gamma_e b(t) S_z \tag{3.7}$$

where $\mathbb{SW}(t)$ is the square wave of period $T = 2\theta/\Omega$ given by

$$\mathbb{SW}(t) = \frac{4}{\pi} \sum_{n=1}^{\infty} \frac{1}{(2n-1)} \sin[\frac{2\pi(2n-1)t}{T}]$$

In order to analyze the dynamics under periodic perturbation, the Hamiltonian is transformed into a time-dependent interaction frame defined by the driving terms (so-called *toggling frame*) [60]. The transformation is completed by the unitary operation $U(t)$:

$$\begin{aligned} U(t) &= \mathcal{T} \exp\Big(-i \int_0^t \Omega \mathbb{SW}(t') S_x dt' \Big) = \exp\Big(-i \int_0^t \Omega \mathbb{SW}(t') S_x dt' \Big) \\ &= \exp\Big(-\frac{4\theta i}{\pi^2} \sum_{n=1}^{\infty} \frac{1}{(2n-1)^2} (1 - \cos[\frac{2\pi(2n-1)t}{T}]) S_x \Big) \\ &= \exp\Big(-i\theta \mathbb{TW}(t) S_x \Big) = \exp\Big(-i \frac{\theta}{\pi} \arccos[\cos(\frac{2\pi t}{T})] S_x \Big) \end{aligned} \tag{3.8}$$

where $\mathcal{T}$ is a time-ordering operator and $\mathbb{TW}(t)$ is the triangular wave of period T defined by

$$\mathbb{TW}(t) = \frac{1}{2} - \frac{4}{\pi^2}\sum_{n=1}^{\infty}\frac{1}{(2n-1)^2}\cos[\frac{2\pi(2n-1)t}{T}].$$

Then, the Hamiltonian in the toggling frame $\widetilde{\mathcal{H}}(t)$ is given by

$$\begin{aligned}\widetilde{\mathcal{H}}(t) &= U^{\dagger}(t)\mathcal{H}(t)U(t) - i\frac{\partial U^{\dagger}(t)}{\partial t}U(t) \\ &= \gamma_e b(t)[\cos(\theta\mathbb{TW}(t))S_z + \sin(\theta\mathbb{TW}(t))S_y] \end{aligned} \tag{3.9}$$

In what follows, we compute the signal and sensitivity of DC and AC magnetometry under RE, but similar derivations apply for other schemes.

3.4 DC Magnetometry

We consider a static magnetic field $b(t) = b$. Under the assumption that $\tilde{\mathcal{H}}(t)$ is periodic with period T and the static field is small, the operator for stroboscopic evolution can be approximated by employing the Magus expansion [95]

$$\begin{aligned}\mathcal{T}\exp\Big(-i\int_0^{nT}\widetilde{\mathcal{H}}(t')dt'\Big) &= \Big\{\mathcal{T}\exp\Big(-i\int_0^{T}\widetilde{\mathcal{H}}(t')dt'\Big)\Big\}^n \\ &\sim \Big\{\exp(-i\overline{\mathcal{H}}T)\Big\}^n = \exp(-i\overline{\mathcal{H}}nT) \end{aligned} \tag{3.10}$$

where $\overline{\mathcal{H}}$ is *Average Hamiltonian* [60, 59]) where first two orders are given by

$$\overline{\mathcal{H}}^{(1)} = \frac{1}{T}\int_0^T\tilde{\mathcal{H}}(t)dt = \frac{2\gamma_e b}{\theta}\sin(\frac{\theta}{2})\Big(\cos(\frac{\theta}{2})S_z + \sin(\frac{\theta}{2})S_y\Big). \tag{3.11}$$

and

$$\begin{aligned}\overline{\mathcal{H}}^{(2)} &= \frac{i}{2T}\int_0^T dt_1\int_0^t dt_2[\widetilde{\mathcal{H}}(t_1),\widetilde{\mathcal{H}}(t_2)] \\ &= \frac{-2(\gamma_e b)^2}{T}\int_0^T dt_1\int_0^t dt_2\sin(\theta(\mathbb{TW}(t_1)-\mathbb{TW}(t_2)))S_x \\ &= (\frac{\gamma_e b}{\theta})^2(1-\cos\theta)S_x. \end{aligned} \tag{3.12}$$

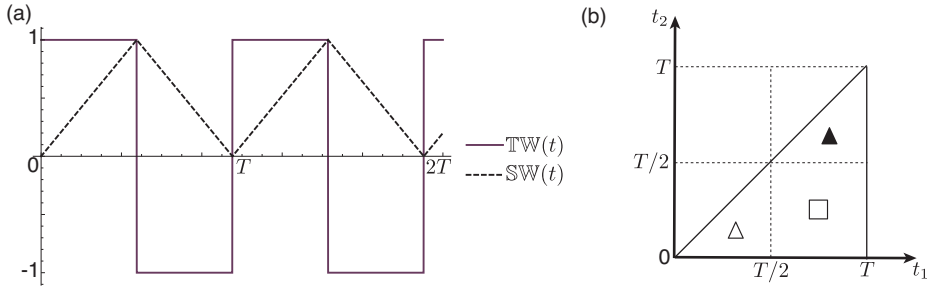

Figure 3-1: (a) The waveform of $\mathbb{SW}(t)$ and $\mathbb{TW}(t)$. (b) Integration domain for calculations of the second order of Magnus expansion. $\mathbb{TW}(t_1)$ and $\mathbb{TW}(t_2)$ take $(2t_1/T, 2t_2/T)$ in the domain $\triangle$, $(2-2t_1/T, 2t_2/T)$ in the domain $\square$, and $(2-2t_1/T, 2-2t_2/T)$ in the domain $\blacktriangle$ respectively.

The effect of the second order is negligible when the static field to be measured is very small. Then, the signal is well approximated by the first order of average Hamiltonian

$$S(nT) = |\langle 0| e^{-i\overline{\mathcal{H}}_1 nT} |0\rangle|^2 = 1 - \sin^2(\frac{\theta}{2}) \sin^2\Big(\frac{\gamma_e b n T |\sin(\frac{\theta}{2})|}{2\theta}\Big). \tag{3.13}$$

We can extend this formula to a general time t by adding a Rabi modulation term $\cos(\Omega t)$ as follows.

$$S(t) = \frac{1}{2} + \frac{1}{2}\cos(\Omega t)\Big(1 - \sin^2(\frac{\theta}{2}) \sin^2\Big(\frac{\gamma_e b t |\sin(\frac{\theta}{2})|}{2\theta}\Big)\Big) \tag{3.14}$$

3.4.1 Sensitivity

The sensitivity of the DC magnetometry calculated for Eq.(3.6) is given by

$$\eta_{\mathrm{RE}} = \frac{1}{C\sqrt{\tau}\frac{\partial S(\tau)}{\partial b}|_{b=0}} = \frac{\theta}{2\gamma_e \sin^2(\theta/2)} \frac{1}{\sqrt{\tau}}. \tag{3.15}$$

Here, we neglect the decoherence of the NV spin and a dead time t_d which is a good approximation when $\tau \ll t_d$. The scheme attains the best sensitivity $\eta_{\mathrm{RE}} \sim 1.38/\gamma_e/\sqrt{\tau}$ at $\theta = 3\pi/4$ which is comparable to the Ramsey sequence yielding $\eta_{\mathrm{Ram}} = 1/\gamma_e/\sqrt{\tau}$. The sensitivity is ultimately limited by the spin decoherence. We model the effect of the spin bath by a static gaussian noise with zero mean and a dispersion

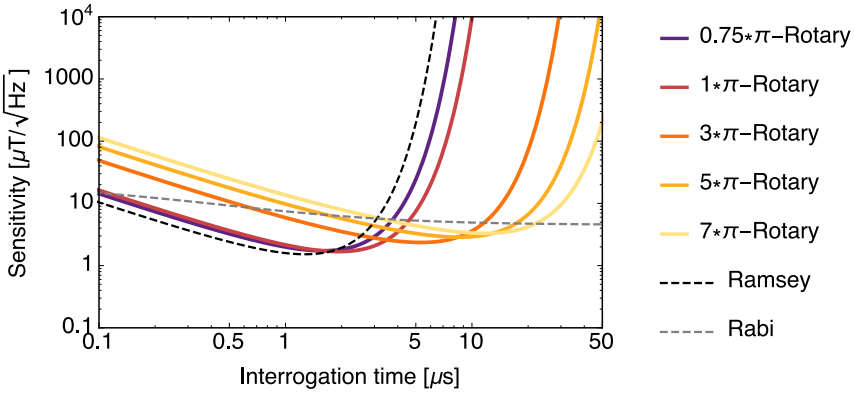

Figure 3-2: (a) Simulation of magnetomerty sensitivity of RE, Rabi and Ramsey sequence. The sensitivity of the RE sequence can be tuned with half-echo rotation angle θ. The Rabi magnetometry is limited by a driving power Ω (= 20 MHz for simulation).

σ, resulting in a decay $e^{-(\tau/T_2^\star)^2}$ where $T_2^\star$ is the dephasing time. The dephasing time of the RE is given by $T_2^\star = \frac{\theta}{\sqrt{2}\sigma|\sin(\theta/2)|}$ while that of the Ramsey is given by $T_2^\star = \frac{\sqrt{2}}{\sigma}$. The RE enables adjusting the dephasing time by changing θ and thus offers more flexibility in measurement time over the Ramsey sequence.

3.5 AC Magnetometry

We consider the evolution of a sensor qubit under a sequence of $2\pi k$-RE and in the presence of an external AC magnetic field of frequency ω and phase φ whose magnitude b is to be sensed. [2] The Hamiltonian in the toggling frame $\widetilde{\mathcal{H}}(t)$ is then given by

$$\widetilde{\mathcal{H}}(t) \;=\; \gamma_e b\cos(\omega t+\varphi)[\cos(4\pi kt)S_z + \mathbb{SW}(t)\sin(4\pi kt)S_y] \tag{3.16}$$

[2] The choice of $\theta = 2\pi k$ makes the Hamiltonian in the toggling frame relatively simple by noticing that

$$\cos(2\pi k\mathbb{TW}(t)) = \cos(4\pi kt), \sin(2\pi k\mathbb{TW}(t)) = \mathbb{SW}(t)\sin(4\pi kt)$$

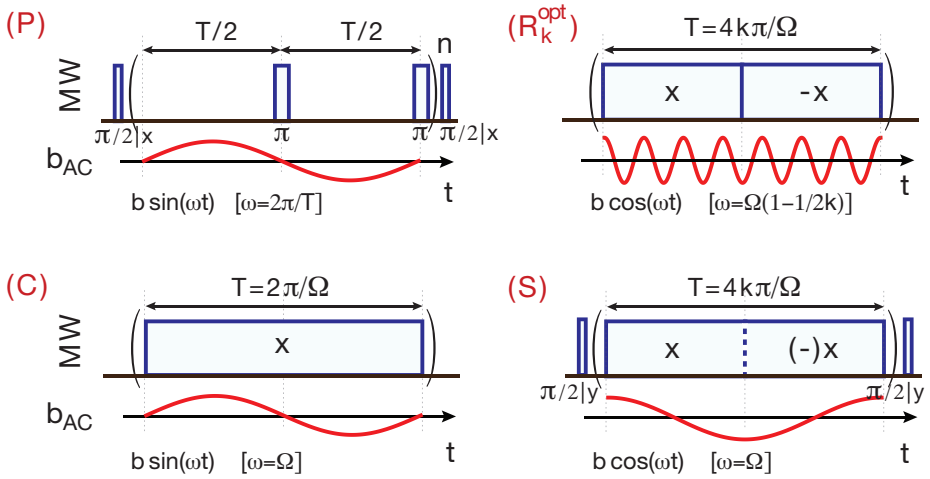

Figure 3-3: Pulse sequences for four AC magnetometry schemes: PDD (P), constant driving (C), RE with optimal frequency (R_k^{opt}) and spin-locking (S). Blue boxes represent microwave driving, with phase (x and y) as indicated.

We consider only the cases where $\varphi = 0$ and $\omega T = 2m\pi$, with m an odd integer, since as we show below this yields good sensitivities. Under this assumption $\tilde{\mathcal{H}}(t)$ is periodic with period T and for small fields b the operator for stroboscopic evolution can be approximated by the first order of the Magus expansion $\overline{\mathcal{H}}^{(0)}$

$$\overline{\mathcal{H}}^{(0)} \approx \frac{1}{T}\int_0^T \tilde{\mathcal{H}}(t)dt = \gamma_e \bar{b}\, S_y. \tag{3.17}$$

When measuring AC field oscillating ω, the RE magnetometry allows adjusting two parameters: the phase alteration cycle (T) and the driving power (Ω) under the constraints of $T = 2m\pi/\omega$ and $\Omega = 4\pi k/T$ respectively.

3.5.1 Sensitivity

The phase acquired during the evolution is thus linear in the magnetic field b to be measured. We note that this effect is true also for other RE angles ϑ; indeed, while under a continuous irradiation (C) the magnetic field contributes only to second order to the acquired phase, here the phase alternation of the driving field refocuses the effect of Rabi oscillation, enhancing the contribution of the magnetic field. Thus, the sensitivity of RE is superior to that of the constant modulation and comparable to

that of PDD (or Ramsey for $\vartheta \neq 2k\pi$ [2]).

If the period of the magnetic field and the RE coincide ($m = 1$), we define $\omega_{low} = \frac{\Omega}{2k}$, which, for a fixed Ω, is easily adjustable by changing the echo angle $2\pi k$. Setting instead $m = (2k-1)$, we define $\omega_{opt} = \frac{\Omega(2k-1)}{2k}$, which yields $\bar{b} = 4bk/[\pi(4k-1)]$ and attains the best sensitivity of the method. The sensitivity, obtained as $\eta(t) = \lim_{b\to 0} \frac{\Delta\mathcal{S}}{|\frac{\partial\mathcal{S}}{\partial b}|}\sqrt{t}$, where $\mathcal{S}$ is the signal and $\Delta\mathcal{S}$ its shot-noise limited uncertainty, depends on $\bar{b}$, that is, on the averaging of the AC field over the sequence period due to the DD modulation. $\bar{b}$ is the Walsh coefficient associated with the DD modulation, if the modulation sequence is a Walsh sequence [30]. We compare the performance of both $2\pi k$-RE schemes to PDD (optimum $\omega = 2\pi/T$, $\varphi = \pi/2$) and a constant modulation with $\omega = \Omega$ (see Fig. 4-2). We obtain for the schemes considered:

$$\eta_{R_k}^{opt} = \eta\tfrac{4k-1}{2k} \qquad (3.18.a) \qquad \eta_P = \eta \qquad (3.18.b)$$

$$\eta_{R_k}^{low} = \eta\tfrac{4k^2-1}{2k} \qquad (3.18.c) \qquad \eta_C = \tfrac{4}{\pi}\eta \qquad (3.18.d),$$

where $\eta = \frac{\pi}{2\gamma\mathcal{C}\sqrt{t}}$, with $\mathcal{C}$ a parameter capturing inefficiencies in the sensor read-out [139]. Here R_k labels a $2k\pi$-RE scheme, P the PDD scheme and C the constant modulation (see Figure 4-2). A fourth operating scheme can be obtained by a "spin-locking" sequence [116], where the spin is first rotated to the transverse plane before applying a driving field in the same direction; choosing $\varphi = 0$ and $\omega = \Omega$ yields the same sensitivity as for the constant modulation, $\eta_S = \eta_C$, even when the driving phase is inverted periodically.

We note that if the phase φ of the AC field is not optimized, the sensitivities are reduced by a factor $\varphi(\varphi)$, with $\varphi_P = \varphi_C = \csc(\varphi)$ and $\varphi_{R_k} = \sec\varphi$. If in addition the phase of the AC field cannot be fixed, $\varphi(\varphi) = \sqrt{2}$ when considering the average signal over many realizations.

These ideal sensitivities are degraded in the presence of noise and whenever the frequency of the AC field is not matched to the DD period. In the following we analyze these two contributions, showing that they lead to a sensitivity $\eta \to \eta\mathcal{D}(t)/W(\omega)$,

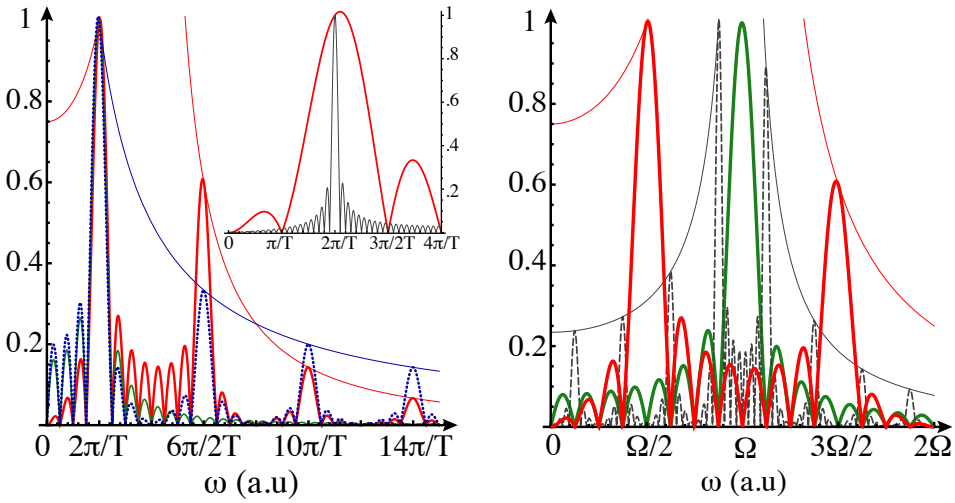

Figure 3-4: Bandwidth for AC magnetometry. We plot the weight functions $W(\omega)$ that scale the phase acquired during DD magnetometry for AC fields of frequency ω. Left: $W(\omega)$ for PDD (blue dotted), RE ($k = 1$, red thick) and constant driving (green, thin line) for $n = 2$ cycles, expressing the frequency in terms of the sequence period. We also plot the envelope of the passband decay for PDD (blue thin) and RE(red thin), given by $\sim 1/\omega$ and $\sim \Omega^2/|\omega^2 - \Omega^2|$ respectively. In the inset: we compare the main peak for $n = 1$ (red, thick) and $n = 10$ (gray) for RE ($k = 1$) showing the reduction in bandwidth. Right: we compare $W(\omega)$ for continuous driving (green) and for RE with $k = 1$ (red, thick) and $k = 4$ (gray, dashed), plotting as a function of ω in units of the Rabi frequency Ω. The thin lines represent the passband decay envelopes for RE.

where $\mathcal{D}(t)$ describes the decay under DD sequences and $W(\omega)$ is the reduction in the accumulated phase when the field frequency ω is suboptimal.

3.5.2 Frequency Response

Optimal sensitivities are obtained by carefully matching the period of the DD schemes to the oscillating field. In practice, however, when field frequencies are either unknown or known to a finite precision, it is of relevance to determine the bandwidth of the scheme and the deviation from optimum sensitivities. We estimate the bandwidth by calculating the phase accumulated by the sensor over the total interrogation time $t = nT$, $\overline{B}t = \int_0^t b(t)f(t)\mathrm{d}t$, and examining the frequency dependence of its absolute value. For PDD, the filter function is $f_P(t) = \mathbb{SW}_P(t)$, the square wave with the period of the modulation. For continuous driving schemes such as RE and Rabi, $f(t)$ is the strength of the toggling frame Hamiltonian. In particular, $f_{R_k}(t) = \mathbb{SW}(t)\sin(\Omega t)$

yielding the weight function $W_{R_k}(\omega) = |\overline{B}_{R_k}(\omega)|/|\overline{B}_{R_k}(\omega^{opt})|$:

$$W_{R_k}(\omega) = \frac{(4k-1)/n}{\left|(4k)^2 - \left(\frac{T\omega}{\pi}\right)^2\right|} \left|\sin(nT\omega)\tan\left(\frac{T\omega}{4}\right)\right|. \tag{3.19}$$

W_{R_k} has peaks (*pass-bands*) at $\omega = 2\pi(2(k+p)-1)/T$, where p is an integer satisfying $p \geq 1-k$. The lowest pass-band occurs for $p = 1-k$, corresponding to $\omega_{low} = \Omega/2k$. The strongest peak is for $p = 0$ at ω_{opt}. Subsequent periodic peaks are attenuated from the symmetry point $\omega = \Omega$ as $\sim \frac{\Omega^2}{|\omega^2-\Omega^2|}$. The FWHM of the optimum peak in $W_{R_k}(\omega)$ decays as $\approx \frac{7.58}{2nT}$, where $7.58 \approx$ FWHM of the squared sinc function, a result common to the other DD schemes.

A similar calculation for the accumulated phase during a PDD sequence indicates the existence of peaks at $\omega = m\pi/T$, with m odd, whose intensity decays as $1/m$. This slower decay than for the RE pass-bands could be beneficial if the goal is to detect fields of unknown frequencies. On the other hand, AC magnetometry under continuous driving or spin locking could be used for frequency-selective detection because $W_C(\omega)$ has a unique peak at $\omega = 2\pi/T$ with FWHM on the same order of that for RE. A comparison of the different weight functions is depicted in Fig. 3-4.

We note that while $W(\omega)$ describes the poor performance of DD schemes at detecting AC fields with unmatched frequencies, this property could in turn be used for frequency-selective measurements and even spectroscopy, by scanning the sequence period. While constant driving provides the best selectivity (canceling out higher octaves), RE provides more flexibility by changing both the period time and the angle $2\pi k$, which allows more uniform noise cancellation. Similarly, noise spectroscopy [18, 8, 156] can be implemented with CoDD [58] and analyzed with a method, close to the weight function, based on the filter function [13, 52], which describes the DD sequence response to the noise.

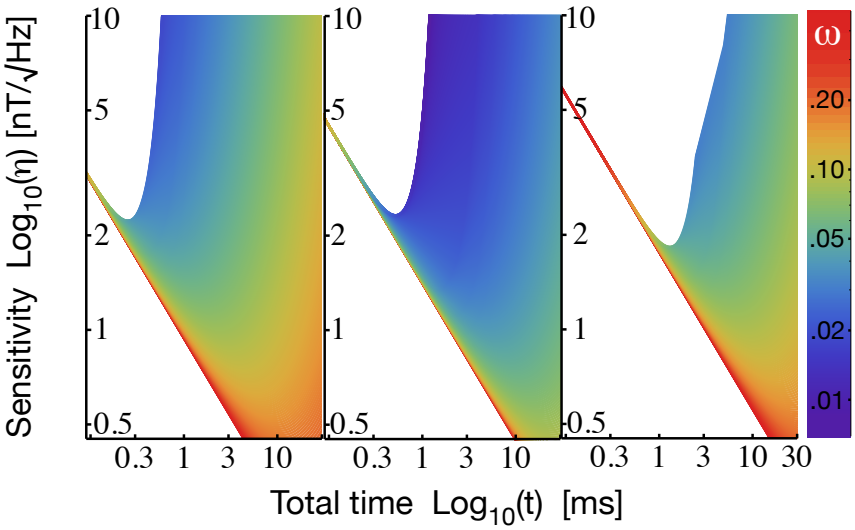

Figure 3-5: Sensitivity for AC magnetometry. We compare the magnetic field sensitivity of a single NV center for PDD (left) and RE ($k=1$ center; $k=4$ right). We assumed $T_2 = 500\mu$s under OU noise (comparable to a ^{13}C bath), yielding a decay $\propto e^{-T^3/(n^2T_2^3)}$, and a single readout with $\mathcal{C} = 0.03$. A larger number of refocusing cycles (with shorter periods) achieves better sensitivity, but can only detect higher frequencies, as shown by the color of the curves (right bar, MHz).

3.6 Decoupling Performance and Robustness

The sensitivities in Eq. (3.18) are further limited by the signal decay $\mathcal{D}(t)$ under the DD sequences. The achievable sensitivity is then a compromise between the refocusing power of the sequence used and the frequency that it allows detecting (Fig. 3-5). While the decay for pulsed DD has been widely studied, evolution under continuous DD is more complex [36]. Here, we study the decoupling performance of the continuous DD scheme against noises of nuclear spins in the diamond lattice.

3.6.1 Modeling of Nuclear Spin Bath

The decoherence of the NV center spin in high quality (electronic grade) sample is attributed to carbon (^{13}C) nuclear spins ($I = 1/2$) with 1.1% natural abundance.[105] The ^{13}C nuclear spin is isolated from phonons of lattice environment [3], however is weakly coupled to other ^{13}C spins via dipole interactions and it rearranges its states

[3]For ^{13}C spin, the phonon-electron coupling is quite weak and it leads to a long spin lattice relaxation time ($T_1 \sim 36$) hours at room temperature [140].

slowly [4]. Then, it gives rise to a local field at the site of the NV center and leads to the spin decoherence of the NV spin. Here, in order to evaluate the decoupling performance of CoDD, we model the decoherence effect induced by ^{13}C nuclear spins. Then, the Hamiltonian of the single NV spin coupled to ^{13}C nuclear spins in the rotating frame is given by

$$\mathcal{H}(t) = \Omega\,\mathbb{SW}_k(t)S_x + S_z\sum_j \boldsymbol{A_j}\boldsymbol{I}^j + \sum_{i>j}\boldsymbol{I}^i\boldsymbol{C}_{ij}\boldsymbol{I}^j \tag{3.20}$$

where I is a spin operator of the ^{13}C nuclear spin, $\boldsymbol{A}$ is the hyperfine coupling tensor between the NV spin and the ^{13}C nuclear spin, $\boldsymbol{C}_{ij}$ is the dipole coupling tensor between two ^{13}C nuclear spins. Due to a large energy mismatch between the NV spin and the nuclear spin, the coupling which does not conserve the energy of the NV spin is dropped. Also, we neglect the nuclear Zeeman interaction. In the interaction frame of the intra-bath coupling $\mathcal{H}_B = \sum_{i>j}\boldsymbol{I}^i\boldsymbol{C}_{ij}\boldsymbol{I}^j$, the hyperfine coupling is described by $\mathcal{H}(t) = \Omega\,\mathbb{SW}_k(t)S_x + S_z\delta(t)$ where $\delta(t) = \sum_j \boldsymbol{A}_j e^{-i\mathcal{H}_B t}\boldsymbol{I}^j e^{i\mathcal{H}_B t}$. The full treatment of dipolar-coupled nuclear spins is not accessible to analytical calculation or exact numerical calculation. Instead, we describe the effect of ^{13}C nuclear spin bath as a Ornstein-Uhlenbeck (OU) process. The OU process has been used in the NMR/ESR field to explain spectral diffusion [5, 83] and the decay of Rabi oscillation [36]. It represents a phenomenological model in which the coupling strength $\delta(t)$ is given by a sum of local fields ($\pm A_j$) generated by nuclear spins which rearrange their spin state for a finite correlation time τ_c [5]. Such $\delta(t)$ can be defined by noise with zero mean and autocorrelation function $G(\tau) = \sigma^2 e^{-\frac{\tau}{\tau_c}}$, with σ the dispersion of coupling strength A_j.

[4] In natural diamond sample, the average distance between ^{13}C nuclear spins is ~ 0.8 nm, leading to a coupling of 14.7 kHz.

[5] This model fails in capturing two-pair correlations or higher order correlation which is not relevant in the natural diamond sample. The analytical treatment of two pair correlation can be found in e.g., [34].

3.6.2 Cumulant Expansion

The time evolution under the stochastic Hamiltonian can be computed by using a cumulant expansion [86, 19, 44]. We can estimate the RE decay to first leading order using the cumulant expansion. The signal decay can be calculated from the average of the superoperator

$$\langle \mathcal{S}_{R_k} \rangle = \left\langle \langle \widehat{0} | \mathcal{T} e^{-i \int_0^t \widehat{H} dt'} | \widehat{0} \rangle \right\rangle$$

where we indicate by a hat the superoperators $\widehat{A} = A \otimes \mathbf{1} - \mathbf{1} \otimes A$, $|\widehat{0}\rangle$ is a polarized state in the Liouville space and $\mathcal{T}$ the time ordering operator. The basic idea of the cumulant expansion is to express the stochastic average of time-ordered operators in terms of cumulants

$$\left\langle \mathcal{T} e^{-i \int_0^t \widehat{H} dt'} \right\rangle = \exp\left[\sum_{n=1}^{\infty} \frac{(-it)^n}{n!} K_n\right] \sim \exp\left[-iK_1 t - \frac{t^2}{2} K_2\right] \tag{3.21}$$

with the first cumulant given by

$$K_1 = \frac{1}{t} \int_0^t \left\langle \widehat{H}(t') \right\rangle dt' \tag{3.22}$$

and the second cumulant given by [6]

$$\begin{aligned}
K_2 &= \frac{1}{t^2}\Big(\left\langle \mathcal{T} \int_0^t dt_1 \int_0^t dt_2 \widehat{H}(t_1)\widehat{H}(t_2) \right\rangle - \left\langle \int_0^t dt \widehat{H}(t) \right\rangle^2 \Big) \\
&= \frac{1}{t^2}\Big(2 \int_0^t dt_1 \int_1^t dt_2 \left\langle \widehat{H}(t_1)\widehat{H}(t_2) \right\rangle - \int_0^t dt_1 \int_0^t dt_2 \left\langle \widehat{H}(t_1)\widehat{H}(t_2) \right\rangle \Big) \\
&= \frac{1}{t^2}\Big(\int_0^t dt_1 \int_1^t dt_2 \left\langle \widehat{H}(t_1)\widehat{H}(t_2) \right\rangle - \int_0^t dt_1 \int_{t_1}^t dt_2 \left\langle \widehat{H}(t_1)\widehat{H}(t_2) \right\rangle \Big) \\
&= \frac{1}{t^2} \int_0^t dt_1 \int_1^t dt_2 \left\langle [\widehat{H}(t_1), \widehat{H}(t_2)] \right\rangle .
\end{aligned} \tag{3.23}$$

[6] In the third line, we use

$$\int_0^t dt_1 \int_{t_1}^t dt_2 \left\langle \widehat{H}(t_1)\widehat{H}(t_2) \right\rangle = \int_0^t dt_1 \int_0^{t_1} dt_2 \left\langle \widehat{H}(t_1)\widehat{H}(t_2) - [\widehat{H}(t_1), \widehat{H}(t_2)] \right\rangle .$$

In the toggling frame of the driving field, the stochastic Hamiltonian is

$$\tilde{\mathcal{H}}(t) = \delta(t)N(t) \equiv \delta(t)\left[\cos(\Omega t)S_z + \mathbb{SW}\sin(\Omega t)S_y\right].$$

The first cumulant is given by

$$K_1 = \frac{1}{t}\int_0^t dt' \left\langle \delta(t')\right\rangle N(t') = 0 \tag{3.24}$$

due to the assumption $\langle\delta(t)\rangle = 0$. The second cumulant for n cycles is $K_2 = n\triangle + \square\sum_{j=1}^{n}(n-j)G_j$ [19], with $G_j = e^{-\frac{4k\pi j}{\Omega\tau_c}}$ and

$$\triangle = \int_0^{4k\pi/\Omega} dt_1 \int_0^{t_1} dt_2 \widehat{N}(t_1)\widehat{N}(t_2)G(t_1-t_2),$$

$$\square = \int_0^{4k\pi/\Omega} dt_1 \int_0^{2k\pi/\Omega} dt_2 \widehat{N}(t_1)\widehat{N}(t_2)G(t_1-t_2).$$

The second cumulant can be written as

$$K_2 = \frac{\alpha+\beta}{2}\hat{S}_z^2 + \frac{\alpha-\beta}{2}\hat{S}_y^2 + \frac{\sqrt{\zeta^2-\beta^2}}{2}(\hat{S}_y\hat{S}_z + \hat{S}_z\hat{S}_y), \tag{3.25}$$

yielding the signal

$$\langle\mathcal{S}_{R_k}\rangle = \frac{1}{2}\left[1 + e^{-\alpha}(\cosh(\zeta) + \frac{\beta}{\zeta}\sinh(\zeta))\right]$$

with

$$\begin{aligned}\alpha = \; & \frac{\sigma^2T^2\tau_c e^{-\frac{nT}{\tau_c}}}{\left(e^{\frac{T}{2\tau_c}}+1\right)^2(16\pi^2k^2\tau_c^2+T^2)^2}\left[2n\left(e^{\frac{T}{2\tau_c}}+1\right)^2 e^{\frac{nT}{\tau_c}}\left(16\pi^2k^2T\tau_c^2 + 64\pi^2k^2\tau_c^3\tanh\left(\frac{T}{4\tau_c}\right)+T^3\right)\right. \\ & \left. -8\tau_c e^{\frac{(n+1)T}{2\tau_c}}\left((T^2-16\pi^2k^2\tau_c^2)+(16\pi^2k^2\tau_c^2+T^2)\cosh\left(\frac{T}{2\tau_c}\right)\right)\sinh\left(\frac{nT}{2\tau_c}\right)\right],\end{aligned} \tag{3.26}$$

$$\begin{aligned}\beta = \; & -\frac{2\sigma^2T^2\tau_c^2e^{-\frac{nT}{\tau_c}}}{\left(e^{\frac{T}{2\tau_c}}+1\right)^2(16\pi^2k^2\tau_c^2+T^2)^2}\times \\ & \left[16\pi^2k^2\tau_c^2\left(e^{\frac{T}{2\tau_c}}-1\right)\left(e^{\frac{nT}{\tau_c}}\left((4n-1)e^{\frac{T}{2\tau_c}}+4n+1\right)+e^{\frac{T}{2\tau_c}}-1\right)+\right. \\ & \left. T^2\left(e^{\frac{T}{2\tau_c}}+1\right)^2\left(e^{\frac{nT}{\tau_c}}-1\right)\right]\end{aligned} \tag{3.27}$$

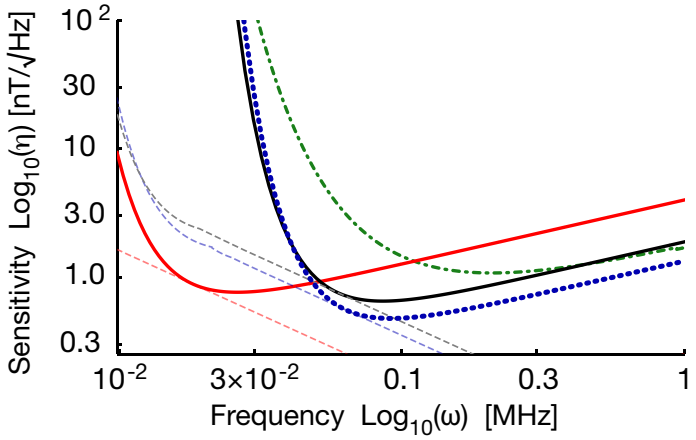

Figure 3-6: Sensitivity for AC magnetometry. We compare the achievable sensitivity for constant driving (green, dash-dotted), PDD of $n = 50$ echoes (blue, dotted) and RE (2π-RE, red, achieving the same sensitivity of PDD at a lower frequency and 8π-RE, black, achieving better sensitivity than PDD at the same frequency). The chosen cycle number is experimentally achievable in the NV center system [124, 113]. The period T is adjusted to match the bandwidth with the frequency of the fields. We assumed $T_2 = 500\mu$s under OU noise, yielding a super-exponential decay $\propto e^{-T^3/(n^2T_2^3)}$, and a readout with $\mathcal{C} = 0.03$. The decay of the constant (Rabi) driving was calculated following Ref. [36] for long τ_c. In addition, the dashed, thin lines correspond to the optimal sensitivity at each frequency, obtained by optimizing the cycle time n (here we assumed no driving or pulse errors).

and

$$\zeta = -\frac{2\sigma^2T^2\tau_c^2e^{-\frac{nT}{\tau_c}}}{\left(e^{\frac{T}{2\tau_c}}+1\right)^2(16\pi^2k^2\tau_c^2+T^2)^2}\Big[64\pi^2k^2T^2\tau_c^2\left(e^{\frac{T}{2\tau_c}}+1\right)^4\left(e^{\frac{nT}{\tau_c}}-1\right)^2\tanh\left(\frac{T}{4\tau_c}\right)^2+\left(16\pi^2k^2\tau_c^2\left(e^{\frac{T}{2\tau_c}}-1\right)\left(e^{\frac{nT}{\tau_c}}\left((4n-1)e^{\frac{T}{2\tau_c}}+4n+1\right)+e^{\frac{T}{2\tau_c}}-1\right)+T^2\left(e^{\frac{T}{2\tau_c}}+1\right)^2\left(e^{\frac{nT}{\tau_c}}-1\right)\right)^2\Big]^{1/2}. \tag{3.28}$$

Consider for example a noise with long correlation time τ_c: In this limit, the signal decays as $\langle\mathcal{S}_{R_k}(t)\rangle = e^{-(\Gamma_{2R}t)^3/n^2}$, with $\Gamma_{2R}^3 = \frac{3\sigma^2}{8k^2\pi^2\tau_c}$. Numerical simulations match well with these approximate analytical results for various noise regimes. The refocusing power of RE can surpass that of pulsed schemes. Using a similar derivation as above [86, 19], the decay under a PDD sequence is instead found to be $\langle\mathcal{S}_P(t)\rangle = e^{-(\Gamma_{2P}t)^3/n^2}$, with $\Gamma_{2P}^3 = \frac{2\sigma^2}{3\tau_c}$ for long correlation noise.

The longer coherence time under the RE sequence can be exploited either to reach

a better sensitivity for a given frequency or to measure lower frequency fields at a given sensitivity, as shown in Fig 3-6. The achievable improvement depends on the ratio of the effective coherence time, $\tau = T_{2R}/T_{2P}$, obtained from the two schemes. Because of the improved refocusing of RE with respect to PDD, the sensitivity can be improved for some noise regimes. In addition, RE-AC magnetometry provides the flexibility of using larger angles (larger k) to allow for longer interrogation times (Fig 3-5) at lower frequencies, which could be beneficial in practical cases in combination with repeated readout schemes [111, 2].

3.6.3 Robustness against Fluctuations of Driving Field

We remark that besides the decay functions obtained above in the presence of dephasing noise, other sources of decay can arise from imperfect pulses or fluctuations in the driving power. The sensitivity is thus limited not only by the coherence time, but also by pulse errors or fluctuations in the driving field. Another notable feature of the RE scheme is to improve the robustness to fluctuations of driving fields [135], which limit the sensitivity of a constant driving scheme. Thus, RE magnetometry is expected to achieve better overall sensitivities than a constant driving. In particular, RE corrects for noise varying more slowly than the RE echo time, as it has been shown experimentally [2]. Therefore, it completely refocuses the effect of static driving field errors. In contrast, simple sequences such as PDD are sensitive even to static pulse errors [149]. There exist however many strategies to correct for these errors, such as XY4-type sequences [57] or composite pulses [89], a full comparison of the limits due to imperfection in the control fields for all these schemes would be an interesting extension of the work.

3.7 Conclusions

In conclusion, we analyzed a novel scheme for DC and AC magnetometry based on continuous dynamical decoupling. While we focused on the simplest DD sequences, we note that more complex driving, such as composite pulses [89], could achieve even

better refocusing of driving field instability and inhomogeneity while still providing comparable sensitivity to existing methods. To sense the DC field, CoDD provides a comparable sensitivity to the Ramsey sequence while providing longer measurement time. We further analyzed the response of AC magnetometry to fields of unknown frequencies, finding that some CoDD schemes (such as continuous driving or spin locking with alternating phases) are advantageous for spectroscopy. In addition, the flexibility of CoDD schemes in modulating both phase and amplitude of the driving field can provide practical advantages, yielding a better compromise between the DD refocusing power and the frequencies of the field to be measured.

Chapter 4

Coherent Feedback Protection

4.1 Introduction

Engineering desired operations on qubits subjected to the deleterious effects of their environment is a critical task in quantum information processing [112] and quantum simulation [91]. The most common approach is to rely on open-loop quantum control techniques, including optimal control algorithms, based on analytical [15, 79, 49] or numerical [127, 78] solutions, Lyapunov design [148] and Hamiltonian engineering [3, 67]. An alternative strategy, inspired by the success of classical control, is feedback control [152, 150]. Because of the complications introduced by quantum measurements [37], closed-loop control is less pervasive in the quantum settings and its experimental implementations have been mainly limited to quantum optics experiments [151, 94, 62].

Here we implement a feedback control algorithm with a solid-state spin qubit system associated with the Nitrogen Vacancy (NV) center in diamond, using coherent feedback [92, 51, 109] to overcome limitations of measurement-based feedback. In particular, we exploit coherent feedback to protect a qubit from dephasing noise, using a second, long-lived qubit as an auxiliary system. In contrast to open-loop dynamical decoupling (DD) techniques [144], the feedback scheme can protect the qubit even against Markovian noise and for an arbitrary period of time (limited only by the auxiliary qubit coherence time) and it is thus more closely related to QEC

schemes [131, 77, 6]. Besides achieving long protection times, the feedback scheme allows us to explore an interesting tradeoff between information gain and decoherence protection, as measurement of the auxiliary qubit state after the feedback algorithm voids the protection, even if the rest of the dynamics is unchanged.

We first describe the feedback-based protection algorithm and its experimental implementation. We then present the experimental results, showing protection of the spin qubit from dephasing noise, and compare the feedback scheme to alternative strategies. Finally, we analyze the tradeoff between qubit protection and measurement of the auxiliary qubit.

4.2 Coherent Feedback Protocol

To demonstrate a coherent feedback protocol with spin qubits, we choose one of the simplest tasks, implementing the no-operation (NOOP) gate on the single qubit. This implies canceling the effects of noise acting on the qubit during the gate time, exploiting the action of an auxiliary qubit (ancilla). A simple, measurement-based feedback scheme was proposed in [141]. Let $|\phi\rangle_q$ be the qubit state to be protected and $|\xi\rangle_b$ the initial state of the bath. We assume that the ancilla is not affected by the bath, thus giving a free evolution $U_{qb}(t) \otimes \mathbf{1}_a$ (where we neglected the bath-only evolution).

First, we prepare superposition state of the ancilla and entangle the qubit and the ancilla by performing a conditional gate U_c.

$$(U_c \otimes |1\rangle \langle 1|_a) |\phi\rangle_q \frac{1}{\sqrt{2}}(|0\rangle_a + |1\rangle_a) = \frac{1}{\sqrt{2}}(|\phi\rangle_q |0\rangle_a + U_c |\phi\rangle_q |1\rangle_a)$$

Then, the qubit evolves in the presence of the bath for a time t and subsequently the conditional gate $U_c^\dagger$ is employed:

$$(U_c^\dagger \otimes |1\rangle \langle 1|_a) U_{qb}(t) \frac{1}{\sqrt{2}}(|\phi\rangle_q |0\rangle_a + U_c |\phi\rangle_q |1\rangle_a) = \frac{1}{\sqrt{2}}(U_{qb}(t) |\phi\rangle_q |0\rangle_a + U_c^\dagger U_{qb}(t) U_c |\phi\rangle_q |1\rangle_a) \tag{4.1}$$

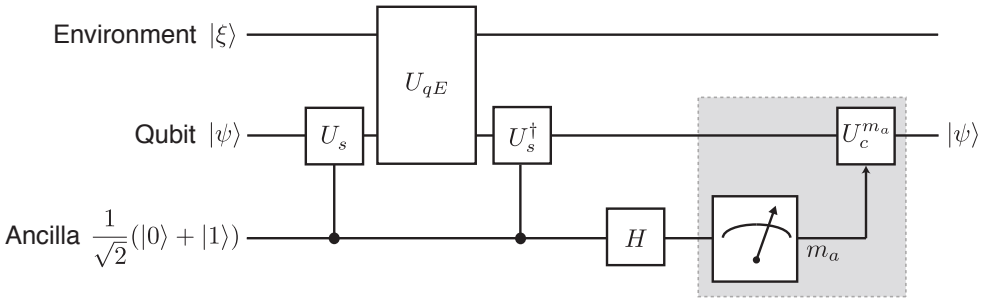

Figure 4-1: Single-bit feedback-based protection scheme. The qubit is protected against noise from the environment. The protocol requires a well-isolated ancilla system. The measurement is applied to the ancilla. Thanks to the deferred measurement principle, the measurement part (shaded region) is replaced by coherent feedback (controlled qubit gate).

Then, the Hadamard gate H is applied on the ancilla to obtain the state $|\Psi(t)\rangle$

$$|\Psi(t)\rangle = \frac{1}{\sqrt{2}}(A_+(t)\,|\phi\rangle_q\,|0\rangle_a + A_-(t)\,|\phi\rangle_q\,|1\rangle_a)\,|\xi\rangle_b\,, \tag{4.2}$$

where $A_\pm(t) = U_{qb}(t) \pm U_c^\dagger U_{qb}(t) U_c$. The conditional gate U_c acting on the qubit is designed such that $A_+ = \mathbf{1}_q \otimes \chi_b^+(t)$ and $A_- = U_q^\dagger \otimes \chi_b^-(t)$, where $\chi_b^\pm(t)$ are operators acting on the bath only. The existence of the desired unitary U_c for qubits under dephasing noise has been proved in Ref. [141]. The feedback protocol is completed by measuring the auxiliary system and applying a correction operation U_q to the qubit based on the measurement result. If the ancilla state is projected into $|1\rangle_a$, then the state would be $(U_q^\dagger \otimes \chi_b^-(t))\,|\phi\rangle_q\,|\xi\rangle_b$ and thus the correction gate U_q would be applied to the qubit to correct the error. Otherwise, the resultant qubit state $|\phi\rangle_q\,\chi_b^+(t)\,|\xi\rangle_b$ would be intact and no correction gate would be needed.

The proposed scheme entails the measurement of the ancilla state, however, by exploiting the entanglement between the qubit and the ancilla, we can circumvent the measurement. Thanks to the principle of deferred measurements [151, 53] we can replace these correction steps by coherent operations. The final state of the combined system is then $\frac{1}{\sqrt{2}}(\chi_b^+(t)\,|0\rangle_a + \chi_b^-(t)\,|1\rangle_a)\,|\phi\rangle_q\,|\xi\rangle_b$, which reveals how the qubit state is completely decoupled from the bath effects, which are instead imposed on the auxiliary qubit. We note that, while we implemented the NOOP gate in

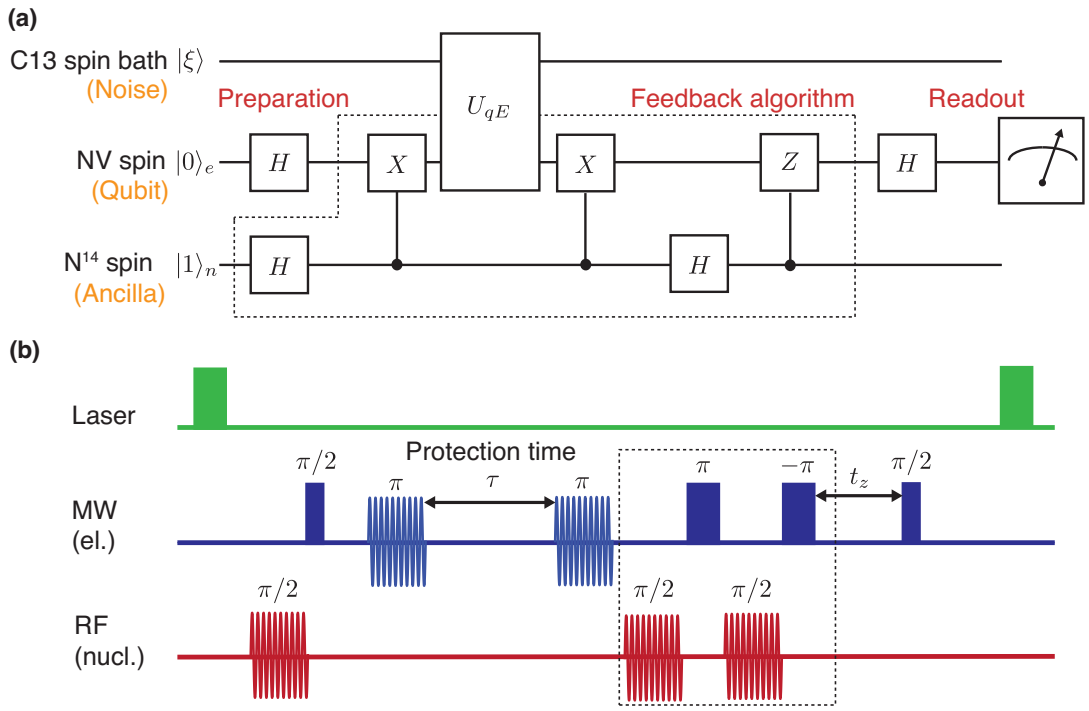

Figure 4-2: (a) Quantum circuit diagram of the feedback-based protection algorithm. A coherent state of the qubit is prepared and read-out after the algorithm by Hadamard gates. In between conditional-NOT gate, the qubit is subjected to noise (and possibly unitary gates U). The ancilla measurement is replaced by coherent feedback (shaded region). (b) Experimental implementation of the the feedback-based protection algorithm with the NV spin system. In the diagram describing the MW excitation, the sinusoidal lines refer to selective pulses acting on the $m_I = 1$ manifold while the solid bars indicate non-selective pulses. The RF excitation describes selective pulse on the $m_s = 0$ manifold. To implement a nonselective RF $\pi/2$ gate (dashed box) we embed a nonselective MW π pulse into the two consecutive RF $\pi/2$ pulses. The controlled-rotation gate to the NV spin is implemented by free evolution (t_Z) under the hyperfine coupling.

the experiments, the scheme is in principle compatible with any gate that commutes with U_c applied before the protecting time, thus potentially making this scheme more flexible than DD techniques. Another advantage with respect to DD techniques is that this scheme is valid independently of the characteristic time scale of the bath and thus it can be used even in the presence of a Markovian bath.

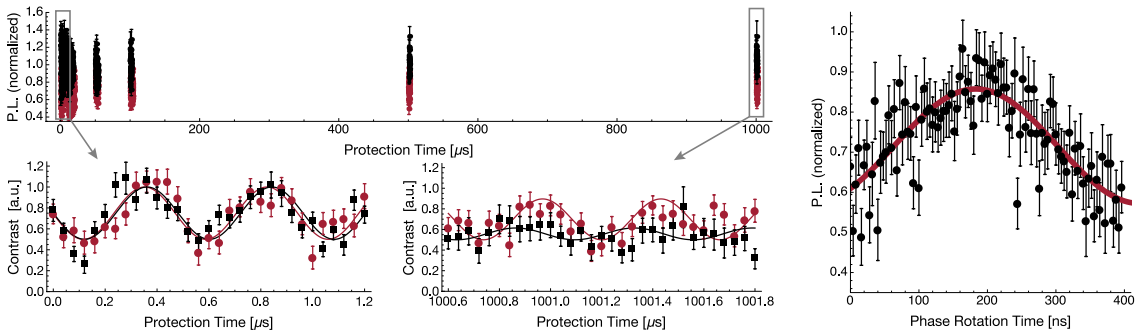

Figure 4-3: Left: Demonstration of the coherent feedback protection algorithm at 386G and 514G. The signal (normalized photoluminescence intensity, top panel) oscillates at the hyperfine coupling frequency, $A = 2.16$ MHz. The initial coherent superposition state of the qubit is preserved for a time $\tau > 1$ ms at 390 G, while we observe a sharp decrease in the signal amplitude at 514 G, where the ancilla state is partly measured. This is evident in the lower panels, where we compare the signal (fidelity) at short (left) and long (right) times, for $B = 390$G (red dots) and 514G (black square). To highlight the differences while taking into account different P.L. intensities and normalizations in the two fields (see methods), we normalized all the data so that at short times the signal has the same (maximum) contrast. Right panel: Weak measurement experiment. Here we plot the signal after a short protection time when applying a weak measurement of the ancilla. In the experiment, we vary the ancilla measurement strength by changing the angle of the last controlled phase rotation gate.

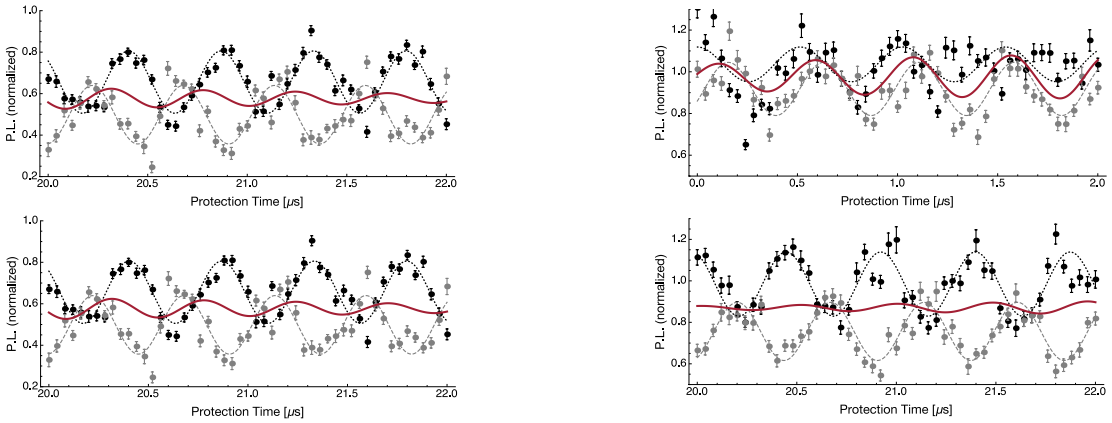

Figure 4-4: Comparison of the fidelity signal with (gray) and without (black) a π-pulse on the qubit at $B = 390$ G (left) and 514 G (right). The upper plots show signals measured at short protection time, $\tau < T_{2e}^{\star}$ $(0 - 2\ \mu\text{s})$ while the lower plots show signals measured at longer times, $\tau > T_{2e}^{\star}$ $(20 - 22\ \mu\text{s})$. The data is fitted (solid lines) with the model shown in the section 4.3. At the lower magnetic field (left), the average of signals (red lines, obtained from the data fits) presents only weak oscillations, indicating that at this field the measurement only carries very little information about the ancilla state. For magnetic field close to the level anti-crossing, the oscillation of the average signal is more pronounced and can be observed until $\tau < T_{2e}^{\star}$, while it disappears at longer times. This is an indication that the ancillary spin effectively decoheres on the $T_{2e}^{\star}$ scale as a result of the feedback algorithm.

4.3 Modeling of Experiment

4.3.1 Hamiltonian of Qubit-Ancilla System

We experimentally demonstrate the algorithm described in Sec.4.2 this feedback-based protection algorithm with a spin system associated with the Nitrogen Vacancy (NV) center in diamond [93, 56]. Here we use an auxiliary qubit associated with the ^{14}N nuclear spin-1 of the NV center to protect the coherence of the NV electronic spin against dephasing noise. The Hamiltonian of the electronic-nuclear spin system is given by Eq. (2.13)

$$\mathcal{H} = D_e S_z^2 + \gamma_e B S_z + Q I_z^2 + \gamma_n B I_z + A_{\parallel} S_z I_z + A_{\perp}(S_x I_x + S_y I_y), \tag{4.3}$$

Due to the large quadrupole splitting ($Q = -4.945$ MHz), a transverse component of the hyperfine coupling $A_{\perp} = -2.62$ MHz is neglected to first order [23, 134]. A magnetic field is applied along the NV crystal axis [111] to lift the degeneracy of the $m_s = \pm 1$ level, yielding the electron and nuclear Zeeman frequencies $\gamma_e B = \omega_e$ and $\gamma_n B = \omega_n$. In the experiment we only use a subspace of the total system representing a two-qubit system. For convenience, we choose the space spanned by the four levels $\{|m_s, m_I\rangle = |0,1\rangle, |0,0\rangle, |-1,1\rangle, |-1,0\rangle\}$ which are mapped to the logical qubit states as follows:$|0,1\rangle \rightarrow |1\rangle_e |1\rangle_n, |0,0\rangle \rightarrow |1\rangle_e |0\rangle_n, |-1,1\rangle \rightarrow |0\rangle_e |1\rangle_n, |-1,0\rangle \rightarrow |0\rangle_e |0\rangle_n$. The effective Hamiltonian can then be simplified by using spin-1/2 operators (Pauli matrices) and transforming to a rotating frame at the resonant frequency of the qubit ($\Delta - \omega_e$) and the ancilla ($\omega_n + Q$):

$$\mathcal{H}' = \frac{A}{4}(-\sigma_z^e + \sigma_z^n - \sigma_z^e \sigma_z^n). \tag{4.4}$$

In high-purity samples, decoherence processes of the electronic spin can be mainly attributed to a bath of spin-1/2 ^{13}C nuclei (1.1% natural abundance) in the lattice. Then, the total Hamiltonian is given by $\mathcal{H}_{tot.} = \mathcal{H}' + \mathcal{H}_{ec} + \mathcal{H}_c$ where $\mathcal{H}_c$ is the bath Hamiltonian, while $\mathcal{H}_{ec}$ denotes the interaction Hamiltonian between the electronic

spin and the ^{13}C bath, yielding a short dephasing time $T^{\star}_{2e} \sim 4\mu s$. We can neglect the interaction between the bath and the ancillary spin, which couples very weakly to any source of magnetic field noise; indeed the much longer coherence time of the ^{14}N spin, $T^{\star}_{2n} \sim 5$ ms, is limited by the NV electronic spin relaxation and not by the ^{13}C bath. Because the noise is dephasing in nature, the feedback-based protection algorithm requires the control gate to be $U_c = \sigma^e_x$ (Pauli-X gate), yielding $A_+ = \mathbf{1}_q \otimes \chi^+_E(t)$ and $A_- = \sigma^e_z \otimes \chi^-_E(t)$. Then, the correction gate should be $U_q = \sigma^e_z$ (Pauli-Z gate).

4.3.2 Time Evolution under Markovian Spin Bath

In order to understand the action of the feedback-based protection algorithm and obtain insights on the limit of its performance, we model the time evolution of the qubit subjected to a spin bath. While in the experiment the actual spin bath has non-Markovian nature, we can employ the simpler model of a Markovian bath, which yields an easier analytical solution, since the results are similar up to a different exponential behavior.

In the model, we consider dephasing of the qubit and ancilla, and the lattice relaxation of the qubit, characterized by the time scales $T^{\star}_{2e}$, $T^{\star}_{2n}$ and T_{1e} respectively. Letting ρ be a state of the qubit and the ancilla, the time evolution under the Markovian environment is determined by the Lindblad equation [90]:

$$\frac{d}{dt}\rho = i[\rho, \mathcal{H}] + \sum_k (L_k \rho L_k^\dagger - \frac{1}{2}\rho L_k^\dagger L_k - \frac{1}{2} L_k^\dagger L_k \rho), \tag{4.5}$$

where $L_1 = \sqrt{\frac{1}{2T^{\star}_{2e}}}\sigma^e_z$, $L_2 = \sqrt{\frac{1}{T_{1e}}}\sigma^e_+$, $L_3 = \sqrt{\frac{1}{T_{1e}}}\sigma^e_-$ and $L_4 = \sqrt{\frac{1}{2T^{\star}_{2n}}}\sigma^e_n$. Given an initial state $\rho_0 = |0\rangle\langle 0|_e \otimes |1\rangle\langle 1|_n$, the state after the NOOP gate is given by

$$\begin{aligned}
&\rho(\tau) = \tfrac{1}{4}\mathbf{1} - \tfrac{1}{4}e^{-\frac{\tau}{T_{1e}}}\cos^2(\tfrac{A\tau}{2})\left[e^{-(\frac{1}{4T^*_{2e}}+\frac{1}{4T^*_{2n}})\tau}\sigma^n_z + e^{-\frac{\tau}{4T^*_{2n}}}\sigma^e_z + e^{-\frac{\tau}{4T^*_{2e}}}\sigma^e_z\sigma^n_z\right] + \\
&\tfrac{1}{8}e^{-(\frac{1}{T_{1e}}+\frac{1}{4T^*_{2e}}+\frac{1}{4T^*_{2n}})\tau}\sin(A\tau)(\sigma^n_x - \sigma^e_x\sigma^n_x) + \tfrac{1}{8}e^{-(\frac{1}{T_{1e}}+\frac{1}{4T^*_{2n}})\tau}\sin(A\tau)(-\sigma^e_y + \sigma^e_y\sigma^n_y) + \\
&\tfrac{1}{8}e^{-(\frac{1}{T_{1e}}+\frac{1}{4T^*_{2e}})\tau}\sin(A\tau)(-\sigma^e_z\sigma^n_x + \sigma^e_y\sigma^n_z) - \\
&\tfrac{1}{4}e^{-\frac{\tau}{T_{1e}}}\sin^2(\tfrac{A\tau}{2})\left[e^{-(\frac{1}{4T^*_{2e}}+\frac{1}{4T^*_{2n}})\tau}\sigma^e_x\sigma^n_z + e^{-\frac{\tau}{4T^*_{2n}}}\sigma^e_z\sigma^n_y + e^{-\frac{\tau}{4T^*_{2e}}}\sigma^e_y\sigma^n_x\right]
\end{aligned} \tag{4.6}$$

where τ is the protection time. Here, we assume the implementation of perfect gate operations and neglect the time evolution during gate operations.

4.3.3 Measurement of the Qubit State

Measurement of the NV spin state is achieved by monitoring the photoluminescence (PL) under laser excitation at 532 nm. Thanks to spin-dependent photo-dynamics in the excited state, the PL intensity is correlated with the NV electronic spin population. In an addition, at magnetic fields close to the excited state level anticrossing, the PL intensity becomes modulated by the nuclear spin state as well, due to the strong hyperfine coupling between the electronic and the nuclear spins in the excited state [110, 73]. Thus the observable in the experiment can be modeled by the operator:

$$M = n_{1,1} \left|1,1\right\rangle \left\langle 1,1\right| + n_{1,0} \left|1,0\right\rangle \left\langle 1,0\right| + n_{0,1} \left|0,1\right\rangle \left\langle 0,1\right| + n_{0,0} \left|0,0\right\rangle \left\langle 0,0\right| \tag{4.7}$$

where the set of $\{n_{ij}\}$ are Poisson-distributed stochastic variables denoting the total number of photons detected during the measurement time (300 ns). Here we neglect the $m_s = +1$ and $m_I = +1$ states that are never populated in the experiment. In order to reduce photon shot noise, we repeat the measurements 5×10^5 times. The raw PL signal S at each measured point of the sequence is normalized by the PL collected from the states ($\left|1,1\right\rangle$ and $\left|0,1\right\rangle$), yielding the normalized signal $\overline{S}$

$$\bar{S} = \frac{\mathrm{Tr}\left\{M\rho\right\} - \langle n_{0,1}\rangle}{\langle n_{1,1}\rangle - \langle n_{0,1}\rangle} = \mathrm{Tr}\left\{\bar{M}\rho\right\} \tag{4.8}$$

where we define the normalized measurement operator $\bar{M}$:

$$\overline{M} = \begin{bmatrix} 1 & 0 & 0 & 0 \\ 0 & 1-\epsilon & 0 & 0 \\ 0 & 0 & 0 & 0 \\ 0 & 0 & 0 & -\eta \end{bmatrix}, \tag{4.9}$$

where $\epsilon = (\langle n_{1,1}\rangle - \langle n_{1,0}\rangle)/(\langle n_{1,1}\rangle - \langle n_{0,1}\rangle)$ and $\eta = (\langle n_{0,1}\rangle - \langle n_{0,0}\rangle)/(\langle n_{1,1}\rangle - \langle n_{0,1}\rangle)$ describe the optical distinguishability of the nuclear spin states in each electronic manifold. Processes driven by the strong hyperfine coupling in the excited state of the NV spin become important when the applied static magnetic field is close to the excited state avoided crossing [136]. Population exchange with the nuclear spin renders the relaxation process of the NV spin correlated with the nuclear spin state, leading to a optical contrast among the nuclear spin states.

From this expression, we obtain the expected signal of the feedback-based protection algorithm:

$$\begin{aligned} S(\tau) = \mathrm{Tr}[\rho(\tau)\bar{M}] = \tfrac{1}{2} - \tfrac{1}{4}(\epsilon+\eta) - \tfrac{1}{2}e^{-(\frac{1}{T_{1e}^{\star}}+\frac{1}{4T_{2n}^{\star}})\tau}\cos^2\left(\tfrac{A\tau}{2}\right) + \\ \tfrac{1}{4}e^{-\frac{\tau}{T_{1e}}}\cos^2\left(\tfrac{A\tau}{2}\right)\left[(\epsilon-\eta)(e^{-\frac{\tau}{4T_{2e}^{\star}}}+e^{-\frac{\tau}{4T_{2n}^{\star}}}) - (\epsilon+\eta)e^{-(\frac{1}{4T_{2e}^{\star}}+\frac{1}{4T_{2n}^{\star}})\tau}\right] \end{aligned} \tag{4.10}$$

When $\epsilon = \eta = 0$ (that is, the nuclear spin is not measured) the signal, which measures the electronic spin state fidelity, is no longer limited by the dephasing of the qubit $T_2^{\star}$, but by that of the ancillary spin and the T_1 process of the qubit. The third factor, which decays at the rate of $T_{2e}^{\star}$, originates from the measurement of the ancilla spin and can be observed as a reduction of the oscillations of the signal in the experiment.

4.4 Implementation of the Feedback-based Protection Gate

In the experiment, the qubit is initialized into the $m_s = 0$ state by optical excitation at 532 nm. At the chosen magnetic field strengths (350G-500G), optical pumping also polarizes the nuclear spin into the $m_I = +1$ state [73], thanks to resonant polarization exchange with the electronic spin in the excited state [73]. After initializing the qubit in the superposition state $|\phi\rangle_e = (|0\rangle_e + |1\rangle_e)/\sqrt{2}$, we implement the feedback-based protection algorithm using the control operations shown in Fig. (4-2). Gate operations on the qubit and ancillary spins are performed by external microwave (MW) and radio frequency (RF) fields, respectively. In order to confirm the performance of the

coherent protection gate, we measure the fidelity of the NOOP gate while varying the protection time τ. As shown in Fig. (B-1.a), the feedback algorithm protects the qubit coherence against the dephasing noise created by the ^{13}C nuclear spin bath for times $\tau > 1$ ms, much longer than the dephasing time. While the spin-bath in this experimental system is non-Markovian [102] and thus DD techniques have reached similar protection times [124], unlike DD this method would also be effective in the Markovian noise regime, with its ultimate limit set only by the coherence time of the ancillary spin and the qubit relaxation. Moreover, compared to other protection schemes, including coherent transfer to the ancilla qubit [106], our scheme is more flexible, as it still allows applying some gate operations on the qubit [141]. For example, in our implementation the qubit was still evolving under the action of the hyperfine coupling, as indicated by the coherent oscillations of the fidelity (these oscillations could be removed e.g., by an adequate timing choice).

4.5 Partial Measurement of the Ancilla

The success of the feedback-based protection algorithm rests on the fact that the increased qubit entropy, due to the coupling to the environment, is dumped on the ancilla. Thus, if information on the ancilla state is collected along the qubit, the protection fails. Here, we investigate this trade-off between the protection power and information gain of the ancilla in two different experiments.

4.5.1 Weak Measurement of the Ancilla

First, we transfer a part of the ancilla entropy back to the qubit by employing a conditional gate that maps the state of the ancilla onto the qubit. As shown in Fig. 4-5.(a), the weak measurement could be obtained by applying a conditional rotation of the NV electronic spin, after that spin has been rotated back to its population state by a $\pi/2$ pulse. The rotation angle φ determines the strength of the measurement. These additional gates can however be avoided, by noting that the circuit is equivalent to replacing the conditional π Z-gate with a conditional θ Z-gate, where $\theta = \pi/2 - \varphi$

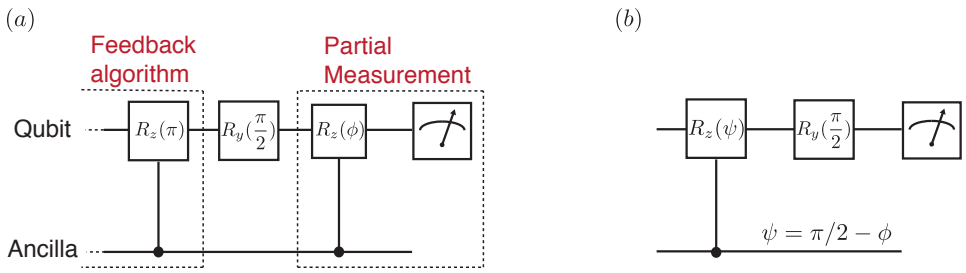

Figure 4-5: Weak measurement circuit. (a) After the feedback algorithm is completed, we employ a controlled X rotation to entangle the qubit with the ancilla by which we can perform a partial measurement of the ancilla: $|\psi\rangle_e(\alpha|1\rangle_n + \beta|0\rangle_n) \rightarrow (\alpha\cos\phi|\psi\rangle_e|1\rangle_n + \beta\sin\phi\sigma_x|\psi\rangle_e|0\rangle_n)$ where the strength of the measurement can be adjusted by choosing the angle ϕ. (b) Equivalent circuit to (a). Due to equivalence of quantum circuits, a sequence (a) can be simplified. In the experiment, we perform a controlled phase (θ) rotation gate instead of the controlled Z rotation in the feedback algorithm.

sets the measurement strength, see Fig.4-5-(b).

The state after the feedback algorithm is given by

$$\rho_\theta(\tau) = \tfrac{1}{4}\mathbf{1} - \tfrac{1}{4}e^{-\frac{\tau}{T_{1e}}}\cos^2(\tfrac{A\tau}{2})\left[e^{-(\frac{1}{4T_{2e}^*}+\frac{1}{4T_{2n}^*})\tau}\sigma_z^n + e^{-\frac{\tau}{4T_{2n}^*}}\sigma_z^e + e^{-\frac{\tau}{4T_{2e}^*}}\sigma_z^e\sigma_z^n\right] + \tfrac{1}{8}e^{-\frac{\tau}{T_{1e}}}(e^{-\frac{\tau}{T_{2n}^\star}} - e^{-\frac{\tau}{T_{2e}^\star}})\cos^2(\tfrac{A\tau}{2})\alpha(\theta)(\sigma_z^e + \sigma_z^e\sigma_z^n) + \ldots$$

where $\alpha(\theta) = 1 + \frac{\cos(A\tau/2+\theta)}{\cos(A\tau/2)}$. Assuming no contrast of the measurement of the nuclear spin ($\epsilon = \eta = 0$), the signal is then given by

$$S_\theta(\tau) = \frac{1}{2} - \frac{1}{2}e^{-(\frac{1}{T_{1e}^\star}+\frac{1}{4T_{2n}^\star})\tau}\cos^2\left(\frac{A\tau}{2}\right) + \frac{1}{2}e^{-\frac{\tau}{T_{1e}}}(e^{-\frac{\tau}{T_{2n}^\star}} - e^{-\frac{\tau}{T_{2e}^\star}})\cos^2\left(\frac{A\tau}{2}\right)\alpha(\theta) \quad (4.11)$$

where we assume there is no contrast among nuclear spin states in measurement.

By changing the angle of rotation of the conditional gate we can vary the strength of the ancilla measurement, from a weak measurement to a strong one. As more information about the state of the ancilla is acquired, the fidelity of the protection gate decreases (see Fig. B-1.b). Note that we can integrate the conditional gate performing the weak measurement of the ancilla state with the last conditional Z-gate of the algorithm, thus in practice performing a conditional phase-shift gate. The

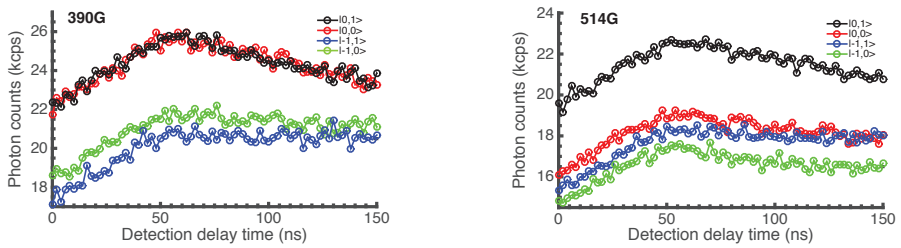

Figure 4-6: Electronic and nuclear-spin dependent fluorescence at different magnetic field strengths. In the experiments, the detection time delay and window were optimized to obtain the maximum contrast of the state. At the lower magnetic field (left), the PL intensity shows only a weak dependence on the nuclear spin state in the $m_s = -1$ manifold, whereas at 514 G, which is very close to the ESLAC, a strong dependence on the nuclear spin state is observed in both manifolds (right panel). From these PL measurements, we obtained the parameters (ϵ, η) to construct the measurement operator.

qubit fidelity is maximized when the conditional gate performs the required π-rotation on the qubit, whereas it decreases when a different phase rotation is employed.

4.5.2 Nuclear Spin Dependent Fluorescence Measurements

While this experiment clearly shows that the effectiveness of the protection is related to the measurement of the ancilla, it is still limited by the fact that we only measured the ancilla via the qubit. To overcome this limitation, we repeated the experiment at a different magnetic fields, where our signal, the fluorescence intensity, carries information about the state of both the qubit and the ancilla. Usually, the nuclear spin state does not affect the PL intensity, i.e. $\epsilon = \eta = 0$ in (Eq.4.7), since it does not affect the relaxation process of the NV center. However, processes driven by the strong hyperfine coupling in the excited state of the NV spin become important when the applied static magnetic field is close to the excited state avoided crossing [136]. Population exchange with the nuclear spin renders the relaxation process of the NV spin correlated with the nuclear spin state, leading to a optical contrast among the nuclear spin states. Thus, the measurement strength of the nuclear spin can be varied by changing a static magnetic field. In our experiments we choose two working conditions that while still allowing nuclear spin polarization ($P > 0.9$) by

optical pumping, could highlight differences due to partial measurement of the ancilla spin. We thus performed the experiment at two different magnetic field (390/514 G) characterized by different strengths of the nuclear spin optical contrast ($\epsilon = 0.14$, $\eta = 0.16$ at $B = 390$G and $\epsilon = 0.86$, $\eta = 0.25$, for $B = 514$G). These values were estimated by measuring the PL intensity for all four states (see Fig. 4-6). Because of the partial measurement of the ancilla state at this magnetic field, the qubit fidelity at long times is reduced (Fig. B-1.a), reflecting the effects of the noise acting on the qubit. We thus reveal a tradeoff between the amount of information acquired about the ancillary system and the protection that it provides to the qubit. To confirm this analysis, we can single out the information about the ancilla state gained in the measurement, by comparing the signal acquired so far with the signal after the qubit is rotated by a π pulse. If the measurement were independent of the state of the ancilla, the average of the two measurements should not vary in time (since it corresponds to measuring the identity operator). Indeed, this is what is observed in experiments performed at the lower magnetic field (Fig.4-4.a); for a magnetic field close to the level anti-crossing, instead, oscillations indicate that we can extract information about the ancilla state. However, at times longer than the qubit dephasing time, the state of ancilla has completely decohered (Fig.4-4.b), thus completely quenching the signal oscillations.

4.6 Conclusions

We performed coherent feedback control on a single solid-state qubit associated with the NV center in diamond. The feedback algorithm was applied to protecting the qubit coherence, thanks to its interaction with an ancillary spin qubit, but it is more broadly compatible with application of other control gates on the qubit during the protection time. We showed that this feedback-based protection algorithm can protect the qubit coherence far beyond the dephasing time of the qubit, even if no active control is applied to decouple it from the noise. As we applied a coherent feedback protocol, thus avoiding measuring the state of the ancilla, the decoherent effects of the

bath are effectively stored in the ancilla. We were thus able to explore an interesting compromise between the amount of information gained about the state of the ancilla and the effectiveness of the protection algorithm.

Appendix A

Modeling of Photoluminescence of the NV Center

A.1 Model Description

We consider the dynamics of the NV spin and the nitrogen nuclear spin under optical excitation at room temperature. At room temperature, the orbital angular momentum is quenched in all the relevant states and thus the dynamics of each states can be approximated by the spin Hamiltonian. Also, the decay rate between the two singlets is very fast and thus they can be treated as one level [97]. Therefore, the optical dynamics of the system can be effectively approximated by the 3-level system consisting of the ground triplet state ($^3A_2$) and the excited triplet state (^3E) and the intermediate state (A_1) [97, 159].

A.2 The Master Equation

The eigenstates and the dynamics of the system having the same orbit and spin configuration is determined by the spin Hamiltonian. On the other hand, transitions between different spin and orbit configurations are driven by an interaction with photons and phonons. In order to incorporate these two different dynamics, we model the time evolution by the Master equation.

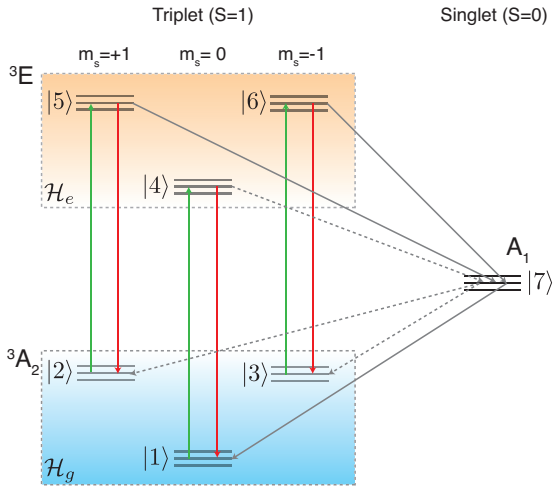

Figure A-1: Level structure of the NV center. There are two fine structures and one singlet which are connected by an optical transition and phonon-assisted transition. In addition, there are hyperfine structures because of the nitrogen nuclear spin.

The Hamiltonian in the ground state $\mathcal{H}_g$ is

$$\mathcal{H}_g = \Delta_g S_z^2 + g\mu_B \boldsymbol{B}\cdot\boldsymbol{S} + QI_z^2 + g_n\mu_n \boldsymbol{B}\cdot\boldsymbol{I} + A_\parallel^g S_z I_z + A_\perp^g (S_x I_x + S_y I_y) \quad \text{(A.1)}$$

while one in the excited state $\mathcal{H}_e$ is

$$\mathcal{H}_e = \Delta_e S_z^2 + E(S_x^2 - S_y^2) + g\mu_B \boldsymbol{B}\cdot\boldsymbol{S} + QI_z^2 + g_n\mu_n \boldsymbol{B}\cdot\boldsymbol{I} + A_\parallel^e S_z I_z + A_\perp^e (S_x I_x + S_y I_y) \quad \text{(A.2)}$$

The Hamiltonian in the singlet level is not considered because it only contains the Hamiltonian of the nuclear spin whose evolution is negligible in the relevant time scale. Then, we consider a time evolution of the whole system which is described by the density operator ρ represented by a matrix of 21×21 entries consisting of 9 states in the ground state, 9 states in the excited state, and the 3 states in the singlet state. $\mathcal{H}_g$ and $\mathcal{H}_e$ decide the eigenstates of the system and also the time evolution in each state during the optical excitation and thus the time evolutions are treated as coherent dynamics. On the other hand, the transitions between different orbital or spin configurations such as the spontaneous and stimulated emissions and the intersystem crossing stem from the coupling with photons and phonons and thus can be treated as a Markov process. In order to consider the time evolution of the system

Transition		Rate [MHz]
Optical pumping	$\gamma_{14}, \gamma_{25}, \gamma_{36}$	64
Spontaneous emission	$\gamma_{41}, \gamma_{52}, \gamma_{63}$	64
Intersystem crossing from ^3E to A_1	γ_{57}, γ_{67}	79.8
	γ_{47}	11.8
Intersystem crossing from A_1 to $^3A_2$	γ_{71}	5.6

Table A.1: Table of transition rates of the NV center in the bulk diamond at the room temperature. All are calculated from the experimentally determined values [117]. The stimulated emission is neglected because of the non-resonant excitation. We also neglect γ_{72} and γ_{73}. In order to include the spin non-conserving transition, a parameter $\epsilon \sim 0.01$ which indicates a ratio of the spin non-conserving transition associated with optical pumping and the spontaneous emission is introduced [98, 117]

ρ subjected to the coherent process by the Hamiltonians with Markov processes, we employ the Master equation in the Lindblad form

$$\frac{d\rho(t)}{dt} = -i[\mathcal{H}, \rho(t)] + \sum_{k=1}^{N} \left(L_k \rho(t) L_k^\dagger - \frac{1}{2} L_k^\dagger L_k \rho(t) - \frac{1}{2} \rho(t) L_k^\dagger L_k \right) \tag{A.3}$$

where $\mathcal{H} = \mathcal{H}_g \otimes \mathbf{1}_e \otimes \mathbf{1}_s + \mathbf{1}_g \otimes \mathcal{H}_e \otimes \mathbf{1}_s$, $L_k = \sqrt{\gamma_{ml}} \left| m \right\rangle \left\langle l \right|$ is a jump operator to describe a transition between $|m\rangle$ and $|l\rangle$ which occurs at a rate γ_{ml}. All of parameters γ are found in table A.1. For numerical calculation, the vectorized form of the Master equation is useful.

$$\frac{d\hat{\rho}(t)}{dt} = \mathcal{L}\hat{\rho}(t) \tag{A.4}$$

where the Lindblabian $\mathcal{L}$ for the vectorized density matrix $\hat{\rho}(t)$ is described as follows [66]

$$\mathcal{L} = -i(\mathcal{H} \otimes \mathbf{1} - \mathbf{1} \otimes \mathcal{H}) + \sum_{k=0}^{N} L_k^\star \otimes L_k - \frac{1}{2} \mathbf{1} \otimes (L_k^\dagger L_k) - \frac{1}{2} (L_k^T L_k^\star) \otimes \mathbf{1}. \tag{A.5}$$

The observable in the experiment is the number of photons associated with the spontaneous emission, which is proportional to the population of the excited states weighted by the decay probability. Therefore, the measurement operator M is given

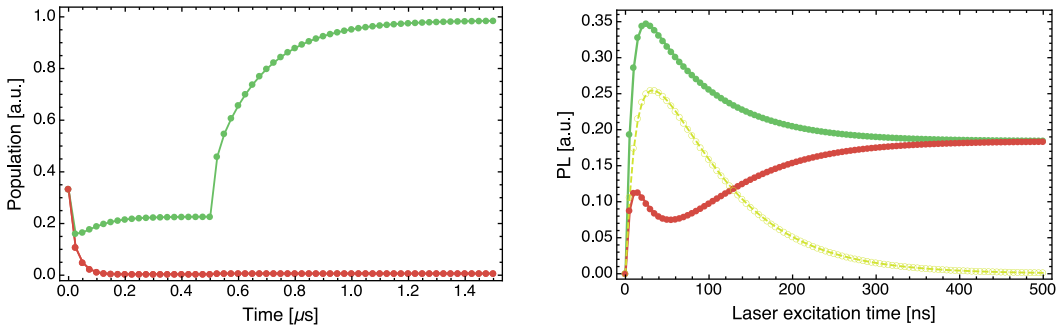

Figure A-2: Left: Population of the ground state under the optical excitation at 100G. Population of $|m_s = 0\rangle$ and $|m_s = \pm 1\rangle$ are indicated by green and red colored curves respectively. In order for the electron to relax from the metastable state, 1 μs wait time follows the laser excitation (500ns). The NV state is polarized to the $|0\rangle$ state. Right: Spin-dependent photoluminescence. The initial state is prepared to be a polarized state $|0\rangle$ (Red) or $|\pm 1\rangle$ before the laser excitation. It shows the PL depends on the initial state. The yellow curve shows the contrast between two states and photon detection should be employed when the maximum contrast is obtained.

by

$$M = k\left(\frac{\gamma_{41}(1+2\epsilon)}{\sum_i \gamma_{4i}}|4\rangle\langle 4| + \frac{\gamma_{51}(1+2\epsilon)}{\sum_i \gamma_{5i}}|5\rangle\langle 5| + \frac{\gamma_{61}(1+2\epsilon)}{\sum_i \gamma_{6i}}|6\rangle\langle 6|\right) \tag{A.6}$$

where a constant k indicates a number of photons arriving to the detector which depends on an integration time, the internal reflection of light inside the diamond sample, the optical system and so on. In the simulation, we set $k = 1$ for simplicity. In reality, a dark count of photons is always measured independent of the state and thus needs to be considered when comparing simulation results with real experiment data.

A.3 Results of Simulations

Due to the state-dependent intersystem crossing which occurs in the excited states and the intermediate state, the optical excitation polarizes the NV spin state into the $m_s = 0$ state. After the laser excitation, the relaxation from the excited state and the intermediate states occurs at the rate of γ_{71} and thus a wait time should be

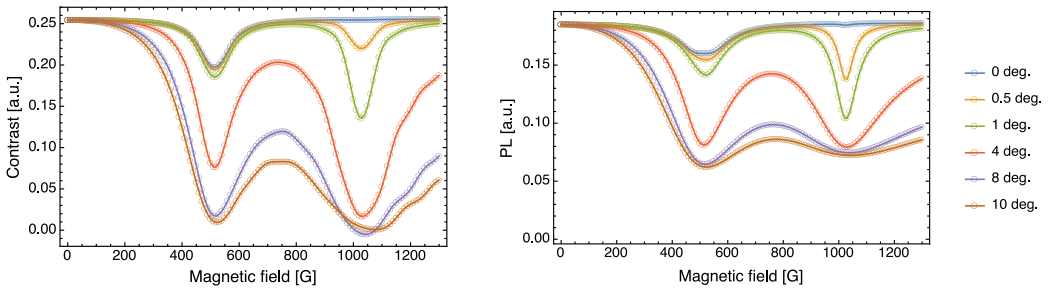

Figure A-3: Dependence of the optical contrast (left) and the PL from the steady state (right) on the magnetic field. The angle of the magnetic field is defined from the crystal axis of the NV center. The PL is collected from the steady states under optical excitation. The PL strongly depends on the angle of the magnetic field around ESLAC and GSLAC because the NV state can be easily mixed by a misaligned field in the excited state and the ground state respectively.

needed to complete the polarization (Fig.A-2). Also, these intersystem crossing do not accompany an emission of photons and thus the PL depends on the initial spin state.(Fig.A-2) The measurement should be performed during the optical excitation when the optical contrast between $|0\rangle$ and $|\pm 1\rangle$ is the largest. In experiments, a static magnetic field is often applied in order to modify the Hamiltonian of the ground state. The magnetic field misaligned from the crystal axis (quantization axis) mixes a spin projection component and thus the optical properties such as the optical contrast between rearranged eigenstates and the PL from the steady state is reconfigured. Particularly, under a magnetic field at the level-crossing in the excited state ($\sim$ 510 G) and in the ground state ($\sim$ 1020 G), the PL is significantly reduced even at a small angle ($\sim$ 0.5 deg) of the misalignment (A-3). This strong dependence of the PL on the magnetic field is fully exploited to align a magnetic field in our experiment. The optical contrast is a good indicator for the alignment of the magnetic field. However, since it requires a pulse measurement and a preparation of two different states, it is not useful. On the other hand, the measurement of the PL from the steady state which is also affected by the magnetic field is a continuous measurement and thus compatible with magnet scanning. Thus, in our experiment, the alignment of the magnetic field is proceeded by monitoring the PL from the steady state.

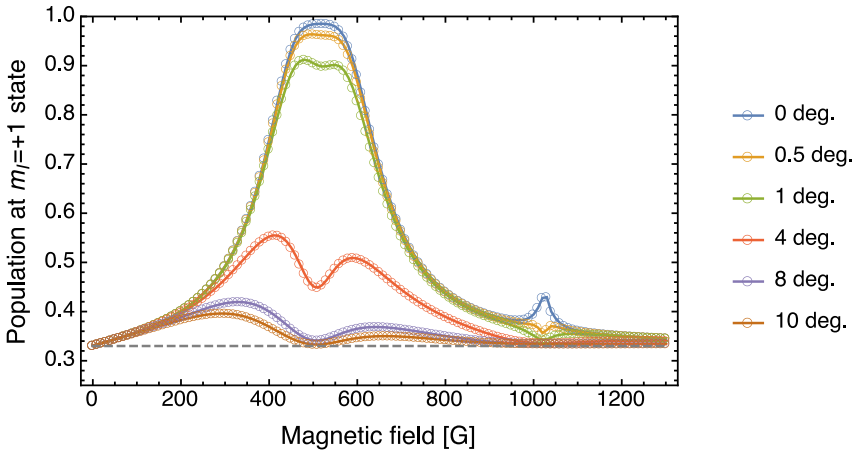

Figure A-4: Polarization of the nitrogen nuclear spin obtained by 2 μs laser excitation followed by 1 μs wait time. The angle of the magnetic field is defined from the crystal axis of the NV center. The PL is collected from the steady states under optical excitation. The nuclear spin is polarized (> 80 %) around the ESLAC (400-600 G). (The dashed line indicates a population in thermal equilibrium.) The PL strongly depends on the angle of the magnetic field around ESLAC and GSLAC because the NV state can be easily mixed by a misaligned field in the excited state and the ground state respectively.

Close to the ESLAC, the NV eigenstate at $ms = 0, -1$ can exchange a spin momentum with the nuclear spin because of the strong hyperfine coupling in the excited state. As a result, the nuclear spin can be polarized.(A-4) Also, the nuclear spin dependent relaxation process impinges on the optical contrast among different nuclear spin states.

Appendix B

Rabi Enhancement

The NV ground state is a two-spin system given by the electronic spin of the NV center ($S = 1$) and the nuclear spin ($I = 1$) of the substitutional ^{14}N adjacent to the vacancy that comprise the defect. In the experiments, we are only interested in two of the nuclear spin levels ($m_I = +1, 0$) that we drive on-resonance, while the third level can be neglected. Then, the Hamiltonian of the reduced system is given by $\mathcal{H} = \mathcal{H}_\parallel + \mathcal{H}_\perp$, where the secular, $\mathcal{H}_\parallel$, and nonsecular, $\mathcal{H}_\perp$, terms are:

$$\begin{aligned} \mathcal{H}_\parallel &= \Delta S_z^2 + (\gamma_e B_z + \frac{A_\parallel}{2}) S_z + (Q + \gamma_n B_z) I_z + A_\parallel S_z I_z, \\ \mathcal{H}_\perp &= \sqrt{2} A_\perp (S_x I_x + S_y I_y). \end{aligned} \tag{B.1}$$

Here S and I are the electron spin-1 and nuclear spin-1/2 operator respectively. $\Delta = 2.87$ GHz is the zero-field splitting and $Q = -4.945$ MHz [134] the nuclear quadrupolar interaction. The NV spin is coupled to the nuclear spin by a hyperfine interaction with a longitudinal component $A_\parallel = -2.162$ MHz [134] and a transverse component $A_\perp$ which we want to estimate. A magnetic field B_z is applied along the NV crystal axis [111] to lift the degeneracy of the $m_s = \pm 1$ level, yielding the electron and nuclear Zeeman frequencies $\gamma_e B_z$ and $\gamma_n B_z$ where $\gamma_e = 2.8$ MHz/G and $\gamma_n = -0.308$ kHz/G.

Let $|m_s, m_I\rangle$ be eigenstates of $\mathcal{H}_\parallel$. The transverse coupling $A_\perp$ mixes states connected via zero-quantum (ZQ) transitions, $|+1, 0\rangle \leftrightarrow |0, 1\rangle$ and $|0, 0\rangle \leftrightarrow |-1, 1\rangle$.

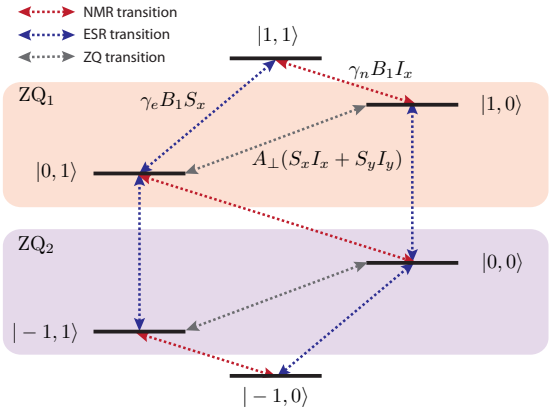

Figure B-1: Energy levels of the reduced NV-^{14}N spin system, showing the transitions that are mixed by the transverse hyperfine coupling.

Diagonalization of the total Hamiltonian can then be achieved by rotating the two ZQ subspaces with a unitary transformation $U_{\mathrm{ZQ}} = e^{-i(\sigma_y^- \vartheta^- + \sigma_y^+ \vartheta^+)}$, where we defined $\sigma_y^+ = i(|+1,0\rangle\langle 0,1| - |0,1\rangle\langle +1,0|)$; $\sigma_y^- = i(|0,0\rangle\langle -1,1| - |-1,1\rangle\langle 0,0|)$ and the rotation angles are

$$\begin{aligned} \tan(2\vartheta^+) &= \frac{2A_\perp}{\Delta + \gamma_e B_z - \gamma_n B_z - Q}, \\ \tan(2\vartheta^-) &= \frac{-2A_\perp}{\Delta - \gamma_e B_z - A_\parallel + \gamma_n B_z + Q}. \end{aligned} \tag{B.2}$$

Because of this level mixing, a field on resonance with the nuclear spin transition also drives electronic transitions. Although the electronic spin state is unchanged to first order, as long as the mixing is small, the nominally forbidden transitions result in an enhancement of the nuclear state nutation frequency, as we explain below. When applying a radio frequency (RF) field to drive the nuclear spin, the interaction

Hamiltonian of the NV-^{14}N system with the RF field is:

$$\mathcal{H}_{\mathrm{rf}}(t) = 2B_1 \cos(\omega t)(\gamma_e S_x + \sqrt{2}\gamma_n I_x), \tag{B.3}$$

where B_1 is the RF field strength. The Hamiltonian can be simplified by going into a rotating picture at the RF frequency ω and applying the rotating wave approximation (RWA), to obtain $\mathcal{H}_{\mathrm{rf}} = B_1(\gamma_e S_x + \sqrt{2}\gamma_n I_x)$. We note that since we might have $\gamma_e B_1 \gg \omega$, effects from the counter-rotating fields, such as Bloch-Siegert shifts of the electronic energies, might be present. These effects were however negligible at the fields and Rabi strengths used in the experiments. Transforming $\mathcal{H}_{\mathrm{rf}}$ with the unitary U_{ZQ} and denoting states and operators in the new frame by a hat, we obtain $\hat{\mathcal{H}}_{\mathrm{rf}} = U_{\mathrm{ZQ}}\mathcal{H}_{\mathrm{rf}}(t)U_{\mathrm{ZQ}}^{\dagger} = \mathcal{H}_n + \mathcal{H}_e$, with

$$\mathcal{H}_n = \sqrt{2}\gamma_n B_1 \left(\alpha_1 \left|\hat{1}\right\rangle\left\langle\hat{1}\right|_e + \alpha_0 \left|\hat{0}\right\rangle\left\langle\hat{0}\right|_e + \alpha_{-1} \left|-\hat{1}\right\rangle\left\langle-\hat{1}\right|_e\right) \hat{I}_x \tag{B.4}$$

Here α_{m_s} denote the enhancement factors in each manifold of the NV spin:

$$\alpha_{+1} \approx 1 \quad + \quad \frac{\gamma_e}{\gamma_n}\frac{A_\perp}{\Delta + \gamma_e B_z - \gamma_n B_z - Q}, \tag{B.5}$$

$$\alpha_0 \approx 1 \quad - \quad \frac{\gamma_e}{\gamma_n}\Big(\frac{A_\perp}{\Delta + \gamma_e B_z - \gamma_n B_z - Q} + \frac{A_\perp}{\Delta - \gamma_e B_z - A_\parallel + \gamma_n B_z + Q}\Big), \tag{B.6}$$

$$\alpha_{-1} \approx 1 \quad + \quad \frac{\gamma_e}{\gamma_n}\frac{A_\perp}{\Delta - \gamma_e B_z - A_\parallel + \gamma_n B_z + Q}, \tag{B.7}$$

where we show expressions exact up to the first order in $\vartheta^{\pm}$. The Hamiltonian $\mathcal{H}_e$ can be neglected since electronic spin transitions are far off-resonance.

Thanks to the strong dependence of the enhancement factors on the transverse hyperfine coupling, we can determine $A_\perp$ with high precision from measurement of the ^{14}N Rabi oscillations.

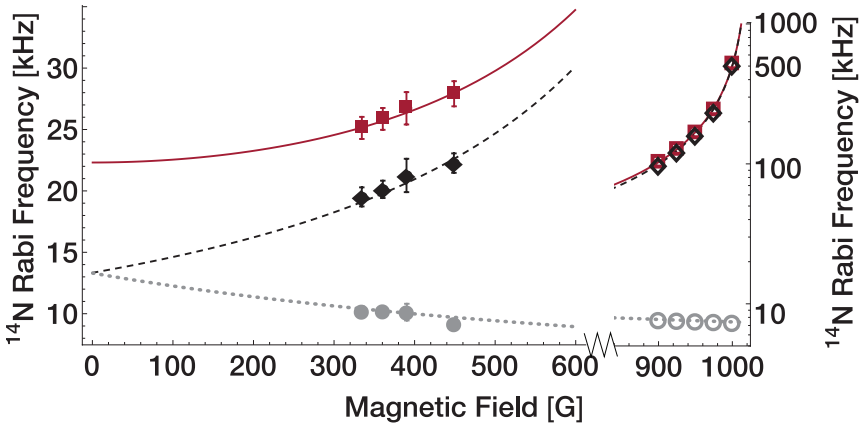

Figure B-2: ^{14}N Rabi frequency in the three NV manifolds (Red, solid line $m_s = 0$. Black, dashed line, $m_s = -1$. Gray, dotted line $m_s = +1$) as a function of the magnetic field. Rabi frequency corresponds to $\frac{\gamma_n B_1}{\sqrt{2}\pi}\alpha_{m_s}$. The filled symbols correspond to the experimental data, which matches closely the theoretical prediction. The effective Rabi frequencies increase rapidly with the field, exceeding 1 MHz when close to the ground state level anti-crossing. The enhancement allows fast manipulation of the nuclear spin even when the bare Rabi field is only $B_1 \approx 3.3$ G. The theoretical prediction is confirmed by simulations (open symbols) of the spin dynamics.

Appendix C

Coherent Control of the Nuclear Spin

The ^{14}N nuclear spin is coherently controlled by employing a resonant RF field. In order to calibrate quantum gates required for the feedback-based protection algorithm ($\pi/2$-rotation), we need to find the resonance frequency and the correct pulse length for the desired rotation. In general, the nuclear spin state cannot be directly measured optically with high fidelity. Thus, after driving the nuclear spin, we apply a gate to map the nuclear spin state to the NV electronic spin . We sweep first the RF frequency to find the resonant frequency of the transition $|1\rangle_q |1\rangle_a \leftrightarrow |1\rangle_q |0\rangle_a$. Then we sweep the RF pulse length to measure the nuclear Rabi oscillation. We note that despite the small gyromagnetic ratio of the nitrogen ($\gamma_n = 0.308$ kHz/G) its Rabi oscillations are significantly enhanced due to the transverse hyperfine coupling with the NV spin (we achieve an enhancement factor of about 20 over the bare Rabi frequency around 500 G). To further characterize the nuclear spin ancillary qubit, we measured the dephasing time, $T_{2n}^{\star}$, by performing a Ramey experiment and obtained $T_{2n}^{\star} \sim 3.2$ ms.

While the dynamics of the ^{14}N spin under RF driving is relatively simple when the NV electronic spin is in one of the population states, further complications arise when the NV qubit is in a superposition state.

For a typical nuclear spin gate, such as the Hadamard gate required for the algorithm, we need to first take into account decoherence process of the electronic spin, which progresses at a faster rate ($T_{2e}^{\star} \sim 4\mu$s) than the gate operation ($t_{\pi} \sim 30\mu$s). In addition, we need to engineer unconditional gates, even when the driving field can

only rotate the nuclear spin in one of the electronic spin manifolds. In order to protect the qubit state during the gate operation, a MW π pulse is inserted in the middle of the RF pulse and is then compensated by adding a second MW -π pulse at the end of the RF pulse. This procedure simultaneously solves also the second issue, as it produces a non-selective gate, as long as the half duration of the RF pulse (before and after the MW π pulse) is chosen to give the full gate rotation.

The Hamiltonian under the RF driving in the rotating frame is given by $\mathcal{H} = \mathcal{H} + \mathcal{H}_{\rm RF}$ with

$$\mathcal{H}_{\rm RF}(t) = -\frac{1}{2}\Omega_e \sigma_z^e \cos(\omega_{\rm RF} t + \phi) + \sqrt{2}\Omega_n \sigma_x^n. \tag{C.1}$$

Here $\Omega_{e,z}$ and Ω_n are the coupling strength of the electronic spin and the nuclear spin with the longitudinal and transverse component of the RF field respectively. We can neglect the coupling of the nuclear spin with the longitudinal component of the RF field as well as the transverse component of the RF effects on the electronic field, since at most it induces a resonance shift (Bloch-Siegert shift [14]) that is, however, refocused by the MW π pulses embedded in the RF pulse. The longitudinal driving imposes an additional, quite large, phase modulation on the NV spin Θ even in the presence of the spin echo π pulses:

$$\begin{aligned} \Theta(\tau) &= -\frac{\Omega_e}{4}\Big(\int_0^\tau \cos(\omega_{\rm RF} t + \phi)dt + \int_\tau^{2\tau} \cos(\omega_{\rm RF} t + \phi)dt\Big) \\ &= \frac{2\Omega_e}{\omega_{\rm RF}} \cos(\omega_{\rm RF}\tau + \phi) \sin(\frac{\omega_{\rm RF}\tau}{2})^2. \end{aligned} \tag{C.2}$$

While in principle one can remove this phase by a proper selection of the timing, in practice this often clashes with other time requirements set by the need to refocus effects due to the hyperfine couplings (explained below).

In our experiment, we used a more flexible strategy to remove this undesired modulation, by employing time-proportional phase incrementation [76] (TPPI) of the RF phase $\phi(\tau)$.

$\Theta(\tau)$ in Eq.(C.2) can indeed be canceled at any time by selecting $\phi(\tau) = -\omega_{RF}\tau$. Unlike stroboscopic detection with time interval $\delta\tau = 2\pi/\omega_{\rm RF}$, TPPI enables the

continuos measurement of the ^{14}N spin Rabi driving and it is also of great use when the time resolution of experiment system is limited and one cannot select $\delta\tau$ with enough precision. Defining $U(\tau) = \exp(-i\mathcal{H}\tau)$ and $R_{\pm\pi} = \exp(\mp i\pi\sigma_x^e)$, the two-spin propagator $V(\tau)$ under TPPI conditions is given by

$$\begin{aligned} V(\tau) &= R_{-\pi}U(\tau)R_{\pi}U(\tau) = e^{-i\left[\frac{A}{4}(\sigma_z^e+\sigma_z^n+\sigma_z^e\sigma_z^n)+\sqrt{2}\Omega_n\sigma_x^n\right]\tau}e^{-i\left[\frac{A}{4}(-\sigma_z^e+\sigma_z^n-\sigma_z^e\sigma_z^n)+\sqrt{2}\Omega_n\sigma_x^n\right]\tau} \\ &= \cos\left(\sqrt{2}\Omega_n\tau\right)\left[\cos\left(\tfrac{At}{2}\right)\mathbf{1} - i\sin\left(\tfrac{At}{2}\right)\sigma_z^n\right] - \\ &\quad i\sin\left(\sqrt{2}\Omega_n\tau\right)\left[\cos\left(\tfrac{At}{2}\right)\sigma_x^n + \sin\left(\tfrac{At}{2}\right)\sigma_z^e\sigma_x^n\right], \end{aligned} \tag{C.3}$$

where we took the limit $A \gg \Omega_n$ to neglect off-resonance driving. We note that due to the combination of the hyperfine coupling $A\sigma_z^e\sigma_z^n/4$ and the RF driving $\frac{1}{2}\Omega_n B_{1x}\sigma_x^n$, the propagators of the nuclear spin before and after the MW π pulse do not commute and the nuclear spin evolves about non-parallel axes in the two time intervals. This can be directly observed as a modulation of the electronic spin echo, similar to the more common ESEEM [104] for anisotropic hyperfine coupling. In order to avoid the effects of the hyperfine, we can set $A\tau = 2\pi$. Since $A \gg \Omega_n$, we can choose a timing τ fulfilling both the above condition and the desired RF pulse time, yielding $V(\tau) = \sigma_x^n$.

Bibliography

[1] A. Abragam. *Principles of Nuclear Magnetism.* Oxford Univ. Press, 1961.

[2] Clarice D. Aiello, Masashi Hirose, and Paola Cappellaro. Composite-pulse magnetometry with a solid-state quantum sensor. *Nat. Commun.*, 4:1419–, Jan 2013.

[3] A. Ajoy and P. Cappellaro. Quantum simulation via filtered hamiltonian engineering: application to perfect quantum transport in spin networks. *Phys. Rev. Lett.*, 110:220503, 2013.

[4] Gonzalo A. Álvarez, Ashok Ajoy, Xinhua Peng, and Dieter Suter. Performance comparison of dynamical decoupling sequences for a qubit in a rapidly fluctuating spin bath. *Phys. Rev. A*, 82:042306, 2010.

[5] P. W. Anderson and P. R. Weiss. Exchange narrowing in paramagnetic resonance. *Rev. Mod. Phys.*, 25(1):269–276, 1953.

[6] G. Arrad, Y. Vinkler, D. Aharonov, and A. Retzker. Increasing sensing resolution with error correction. *Phys. Rev. Lett.*, 112:150801, Apr 2014.

[7] Gopalakrishnan Balasubramanian, I Y Chan, Roman Kolesov, Mohannad Al-Hmoud, Julia Tisler, Chang Shin, Changdong Kim, Aleksander Wojcik, Philip R Hemmer, Anke Krueger, Tobias Hanke, Alfred Leitenstorfer, Rudolf Bratschitsch, Fedor Jelezko, and Jörg Wrachtrup. Nanoscale imaging magnetometry with diamond spins under ambient conditions. *Nature*, 455(7213):648–51, October 2008.

[8] N. Bar-Gill, L.M. Pham, C. Belthangady, D. Le Sage, P. Cappellaro, J.R. Maze, M.D. Lukin, A. Yacoby, and R. Walsworth. Suppression of spin-bath dynamics for improved coherence of multi-spin-qubit systems. *Nat. Commun.*, 3:858, 2012.

[9] A. Batalov, V. Jacques, F. Kaiser, P. Siyushev, P. Neumann, L. J. Rogers, R. L. McMurtrie, N. B. Manson, F. Jelezko, and J. Wrachtrup. Low temperature studies of the excited-state structure of negatively charged nitrogen-vacancy color centers in diamond. *Phys. Rev. Lett.*, 102(19):195506, 2009.

[10] Simon J. Bending. Local magnetic probes of superconductors. *Advances in Physics*, 48(4):449–535, 1999.

[11] Joakim Bergli and Lara Faoro. Exact solution for the dynamical decoupling of a qubit with telegraph noise. *Phys. Rev. B*, 75:054515, Feb 2007.

[12] Alexios Beveratos, Rosa Brouri, Thierry Gacoin, André Villing, Jean-Philippe Poizat, and Philippe Grangier. Single photon quantum cryptography. *Phys. Rev. Lett.*, 89(18):187901, 2002.

[13] M J Biercuk, A C Doherty, and H Uys. Dynamical decoupling sequence construction as a filter-design problem. *J. of Phys. B*, 44(15):154002, 2011.

[14] F. Bloch. Generalized theory of relaxation. *Phys. Rev.*, 105:1206, 1957.

[15] Ugo Boscain and Paolo Mason. Time minimal trajectories for a spin 1/2 particle in a magnetic field. *Journal of Mathematical Physics*, 47(6):062101, 2006.

[16] G. S. Boutis, P. Cappellaro, H. Cho, C. Ramanathan, and D. G. Cory. Pulse error compensating symmetric magic-echo trains. *J. Mag. Res.*, 161:132–137, 2003.

[17] D.P Burum, M. Linder, and R. R. Ernst. Low-power multipulse line narrowing in solid-state nmr. *J. Mag. Res.*, 44(1):173 – 188, 1981.

[18] Jonas Bylander, Simon Gustavsson, Fei Yan, Fumiki Yoshihara, Khalil Harrabi, George Fitch, David G Cory, and William D Oliver. Noise spectroscopy through dynamical decoupling with a superconducting flux qubit. *Nat. Phys.*, 7:565–570, 2011.

[19] P. Cappellaro, J. S. Hodges, T. F. Havel, and D. G Cory. Principles of control for decoherence-free subsystems. *J. Chem. Phys.*, 125:044514, 2006.

[20] H. Y. Carr and E. M. Purcell. Effects of diffusion on free precession in nuclear magnetic resonance experiments. *Phys. Rev.*, 94(3):630–638, 1954.

[21] Carlton M. Caves. Quantum-mechanical noise in an interferometer. *Phys. Rev. D*, 23:1693–1708, Apr 1981.

[22] Ke Chen and Ren-Bao Liu. Dynamical decoupling for a qubit in telegraphlike noises. *Phys. Rev. A*, 82:052324, Nov 2010.

[23] Mo Chen, Masashi Hirose, and Paola Cappellaro. Measurement of transverse hyperfine interaction by forbidden transitions. *Phys. Rev. B*, 92:020101, Jul 2015.

[24] Bin Cheng, Qiang-Hua Wang, and Robert Joynt. Transfer matrix solution of a model of qubit decoherence due to telegraph noise. *Phys. Rev. A*, 78:022313, Aug 2008.

[25] Boris M. Chernobrod and Gennady P. Berman. Spin microscope based on optically detected magnetic resonance. *Journal of Applied Physics*, 97(1):–, 2005.

[26] L. Childress, J. M. Taylor, A. S. Sorensen, and M. D. Lukin. Fault-tolerant quantum repeaters with minimal physical resources and implementations based on single-photon emitters. *Phys. Rev. A*, 72(5):052330, 2005.

[27] C D Clark and C A Norris. Photoluminescence associated with the 1.673, 1.944 and 2.498 eV centres in diamond. *Journal of Physics C: Solid State Physics*, 4(14):2223, 1971.

[28] N. Cody Jones, T. D. Ladd, and B. H. Fong. Dynamical decoupling of a qubit with always-on control fields. *arXiv:1205.2402*, 2012.

[29] C. Cohen-Tannoudji, J. Dupont-Roc, and G. Grynberg. *Atom-Photon Interactions: Basic Processes and Applications*. Wiley, New York, 1992.

[30] A. Cooper, E. Magesan, H.N. Yum, and P. Cappellaro. Time-resolved magnetic sensing with electronic spins in diamond. *Nat. Commun.*, 5:3141, 2014.

[31] G. Davies and M. F. Hamer. Optical studies of the 1.945 eV vibronic band in diamond. *Proceedings of the Royal Society of London A: Mathematical, Physical and Engineering Sciences*, 348(1653):285–298, 1976.

[32] G. de Lange, D. Ristè, V. Dobrovitski, and R. Hanson. Single-spin magnetometry with multipulse sensing sequences. *Phys. Rev. Lett.*, 106(8):080802, February 2011.

[33] Rogerio de Sousa. Electron Spin as a Spectrometer of Nuclear Spin Noise and Other Fluctuations. In Marco Fanciulli, editor, *Electron Spin Resonance and Related Phenomena in Low-Dimensional Structures*, volume 115 of *Topics in Applied Physics*, pages 183–220. Springer Berlin Heidelberg, 2009.

[34] Rogerio de Sousa and S. Das Sarma. Theory of nuclear-induced spectral diffusion: Spin decoherence of phosphorus donors in si and gaas quantum dots. *Phys. Rev. B*, 68:115322, Sep 2003.

[35] D. P. Divincenzo. The Physical Implementation of Quantum Computation. *Fortschritte der Physik*, 48:771–783, 2000.

[36] V. V. Dobrovitski, A. E. Feiguin, R. Hanson, and D. D. Awschalom. Decay of rabi oscillations by dipolar-coupled dynamical spin environments. *Phys. Rev. Lett.*, 102:237601, 2009.

[37] Andrew C. Doherty, Kurt Jacobs, and Gerard Jungman. Information, disturbance, and hamiltonian quantum feedback control. *Phys. Rev. A*, 63:062306, May 2001.

[38] F. Dolde, H. Fedder, M. W. Doherty, T. Nobauer, F. Rempp, G. Balasubramanian, T. Wolf, F. Reinhard, L. C. L. Hollenberg, F. Jelezko, and J. Wrachtrup. Electric-field sensing using single diamond spins. *Nat. Phys.*, 7(6):459–463, June 2011.

[39] A. Dréau, M. Lesik, L. Rondin, P. Spinicelli, O. Arcizet, J.-F. Roch, and V. Jacques. Avoiding power broadening in optically detected magnetic resonance of single nv defects for enhanced dc magnetic field sensitivity. *Phys. Rev. B*, 84:195204, Nov 2011.

[40] L. du. Preez. PhD thesis, University Witwatersrand, 1965.

[41] F. F. Fanchini, J. E. M. Hornos, and R. d. J. Napolitano. Continuously decoupling single-qubit operations from a perturbing thermal bath of scalar bosons. *Phys. Rev. A*, 75:022329, 2007.

[42] S. Felton, A. M. Edmonds, M. E. Newton, P. M. Martineau, D. Fisher, and D. J. Twitchen. Electron paramagnetic resonance studies of the neutral nitrogen vacancy in diamond. *Phys. Rev. B*, 77:081201, Feb 2008.

[43] S. Felton, A. M. Edmonds, M. E. Newton, P. M. Martineau, D. Fisher, D. J. Twitchen, and J. M. Baker. Hyperfine interaction in the ground state of the negatively charged nitrogen vacancy center in diamond. *Phys. Rev. B*, 79:075203, Feb 2009.

[44] Jack H. Freed. Generalized cumulant expansions and spinrelaxation theory. *The Journal of Chemical Physics*, 49(1), 1968.

[45] G. D. Fuchs, G. Burkard, P. V. Klimov, and D. D. Awschalom. A quantum memory intrinsic to single nitrogen-vacancy centres in diamond. *Nat Phys*, 7(10):789–793, October 2011.

[46] G. D. Fuchs, V. V. Dobrovitski, R. Hanson, A. Batra, C. D. Weis, T. Schenkel, and D. D. Awschalom. Excited-state Spectroscopy Using Single Spin Manipulation in Diamond. *Phys. Rev. Lett.*, 101(11):117601, 2008.

[47] Adam Gali, Maria Fyta, and Efthimios Kaxiras. Ab initio supercell calculations on nitrogen-vacancy center in diamond: Electronic structure and hyperfine tensors. *Phys. Rev. B*, 77(15):155206, 2008.

[48] Y. M. Galperin, B. L. Altshuler, J. Bergli, and D. V. Shantsev. Non-gaussian low-frequency noise as a source of qubit decoherence. *Phys. Rev. Lett.*, 96:097009, Mar 2006.

[49] A. Garon, S. J. Glaser, and D. Sugny. Time-optimal control of SU(2) quantum operations. *Phys. Rev. A*, 88:043422, Oct 2013.

[50] Vittorio Giovannetti, Seth Lloyd, and Lorenzo Maccone. Advances in quantum metrology. *Nat. Photon.*, 5(4):222–229, 2011.

[51] J. Gough and M.R. James. The series product and its application to quantum feedforward and feedback networks. *Automatic Control, IEEE Transactions on*, 54(11):2530–2544, Nov 2009.

[52] Todd Green, Hermann Uys, and Michael J. Biercuk. High-order noise filtering in nontrivial quantum logic gates. *Phys. Rev. Lett.*, 109:020501, 2012.

[53] Robert Griffiths and Chi-Sheng Niu. Semiclassical fourier transform for quantum computation. *Phys. Rev. Lett.*, 76(17):3228–231, Apr 1996.

[54] Bernhard Grotz, Moritz V. Hauf, Markus Dankerl, Boris Naydenov, Sebastien Pezzagna, Jan Meijer, Fedor Jelezko, Jorg Wrachtrup, Martin Stutzmann, Friedemann Reinhard, and Jose A. Garrido. Charge state manipulation of qubits in diamond. *Nat Commun*, 3:729–, March 2012.

[55] L Grover. A fast quantum mechanical algorithm for database search. In *Proceedings of 28th Annual ACM Symposium on Theory of Computing (STOC)*, pages 212–219, 1996.

[56] A. Gruber, A. Drabenstedt, C. Tietz, L. Fleury, J. Wrachtrup, and C. von Borczyskowski. Scanning confocal optical microscopy and magnetic resonance on single defect centers. *Science*, 276(5321):2012–2014, 1997.

[57] Terry Gullion, David B Baker, and Mark S Conradi. New, compensated carr-purcell sequences. *J. Mag. Res.*, 89(3):479 – 484, 1990.

[58] S. Gustavsson, J. Bylander, F. Yan, P. Forn-Diaz, V. Bolkhovsky, D. Braje, G. Fitch, K. Harrabi, D. Lennon, J. Miloshi, P. Murphy, R. Slattery, S. Spector, B. Turek, T. Weir, P. B. Welander, F. Yoshihara, D. G. Cory, Y. Nakamura, T. P. Orlando, and W. D. Oliver. Driven dynamics and rotary echo of a qubit tunably coupled to a harmonic oscillator. *Phys. Rev. Lett.*, 108:170503, 2012.

[59] U. Haeberlen. *High Resolution NMR in Solids: Selective Averaging*. Academic Press Inc., New York, 1976.

[60] U. Haeberlen and J.S. Waugh. Coherent averaging effects in magnetic resonance. *Phys. Rev.*, 175(2):453–467, 1968.

[61] E. L. Hahn. Spin echoes. *Phys. Rev.*, 80(4):580–594, 1950.

[62] Ryan Hamerly and Hideo Mabuchi. Advantages of coherent feedback for cooling quantum oscillators. *Phys. Rev. Lett.*, 109:173602, Oct 2012.

[63] Kyu Young Han, Seong Keun Kim, Christian Eggeling, and Stefan W. Hell. Metastable dark states enable ground state depletion microscopy of nitrogen vacancy centers in diamond with diffraction-unlimited resolution. *Nano Letters*, 10(8):3199–3203, 2010. PMID: 20698637.

[64] R. Hanson, F. M. Mendoza, R. J. Epstein, and D. D. Awschalom. Polarization and readout of coupled single spins in diamond. *Phys. Rev. Lett.*, 97(8):087601, 2006.

[65] J. Harrison, M. J. Sellars, and N. B. Manson. Optical spin polarisation of the n-v centre in diamond. *Journal of Luminescence*, 107(1-4):245 – 248, 2004. Proceedings of the 8th International Meeting on Hole Burning, Single Molecule, and Related Spectroscopies: Science and Applications.

[66] Timothy F. Havel. Robust procedures for converting among lindblad, kraus and matrix representations of quantum dynamical semigroups. *Journal of Mathematical Physics*, 44(2), 2003.

[67] David Hayes, Steven T Flammia, and Michael J Biercuk. Programmable quantum simulation by dynamic hamiltonian engineering. *New J. Phys.*, 16(8):083027, 2014.

[68] Xing-Fei He, Neil B. Manson, and Peter T. H. Fisk. Paramagnetic resonance of photoexcited N-V defects in diamond. i. level anticrossing in the ^{3}A ground state. *Phys. Rev. B*, 47(14):8809–8815, 1993.

[69] Xing-Fei He, Neil B. Manson, and Peter T. H. Fisk. Paramagnetic resonance of photoexcited N-V defects in diamond. ii. Hyperfine interaction with the ^{14} N nucleus. *Phys. Rev. B*, 47(14):8816–8822, 1993.

[70] J. S. Hodges, J. C. Yang, C. Ramanathan, and D. G. Cory. Universal control of nuclear spins via anisotropic hyperfine interactions. *Phys. Rev. A*, 78(1):010303, 2008.

[71] Faruque M. Hossain, Marcus W. Doherty, Hugh F. Wilson, and Lloyd C. L. Hollenberg. *Ab Initio* electronic and optical properties of the NV^- center in diamond. *Phys. Rev. Lett.*, 101:226403, Nov 2008.

[72] MaminH. J., PoggioM., DegenC. L., and RugarD. Nuclear magnetic resonance imaging with 90-nm resolution. *Nat Nano*, 2(5):301–306, May 2007.

[73] V. Jacques, P. Neumann, J. Beck, M. Markham, D. Twitchen, J. Meijer, F. Kaiser, G. Balasubramanian, F. Jelezko, and J. Wrachtrup. Dynamic polarization of single nuclear spins by optical pumping of nitrogen-vacancy color centers in diamond at room temperature. *Phys. Rev. Lett.*, 102(5):057403, 2009.

[74] F. Jelezko, T. Gaebel, I. Popa, A. Gruber, and J. Wrachtrup. Observation of coherent oscillations in a single electron spin. *Phys. Rev. Lett.*, 92(7):076401, 2004.

[75] F. Jelezko, I. Popa, A. Gruber, C. Tietz, J. Wrachtrup, A. Nizovtsev, and S. Kilin. Single spin states in a defect center resolved by optical spectroscopy. *Appl. Phys. Lett.*, 81(12):2160–2162, 2002.

[76] M. Kälin and A. Schweiger. Radio-frequency-driven electron spin echo envelope modulation spectroscopy on spin systems with isotropic hyperfine interactions. *The Journal of Chemical Physics*, 115(23):10863–10875, 2001.

[77] E. M. Kessler, I. Lovchinsky, A. O. Sushkov, and M. D. Lukin. Quantum error correction for metrology. *Phys. Rev. Lett.*, 112:150802, Apr 2014.

[78] N. Khaneja, T. Reiss, C. Kehlet, T. Schulte-Herbuggen, and S. Glaser. Optimal control of coupled spin dynamics: design of nmr pulse sequences by gradient ascent algorithms. *J. Magn. Res.*, 172:296–305, 2005.

[79] Navin Khaneja and Steffen J. Glaser. Efficient transfer of coherence through ising spin chains. *Phys. Rev. A*, 66:060301, 2002.

[80] K. Khodjasteh and D. A. Lidar. Fault-tolerant quantum dynamical decoupling. *Phys. Rev. Lett.*, 95(18):180501, 2005.

[81] Kaveh Khodjasteh and Daniel A. Lidar. Performance of deterministic dynamical decoupling schemes: Concatenated and periodic pulse sequences. *Phys. Rev. A*, 75(6):062310, 2007.

[82] Kaveh Khodjasteh and Lorenza Viola. Dynamical quantum error correction of unitary operations with bounded controls. *Phys. Rev. A*, 80:032314, 2009.

[83] J. R. Klauder and P. W. Anderson. Spectral diffusion decay in spin resonance experiments. *Phys. Rev.*, 125:912–932, 1962.

[84] Shlomi Kotler, Nitzan Akerman, Yinnon Glickman, Anna Keselman, and Roee Ozeri. Single-ion quantum lock-in amplifier. *Nature*, 473(7345):61–5, May 2011.

[85] R. Kubo, M. Toda, and H. Hashitsume. *Statistical Physics II*. Springer, 2nd edition, 1991.

[86] Ryogo Kubo. Generalized cumulant expansion method. *J. Phys. Soc. Japan*, 17(7):1100–1120, 1962.

[87] Christian Kurtsiefer, Sonja Mayer, Patrick Zarda, and Harald Weinfurter. Stable solid-state source of single photons. *Phys. Rev. Lett.*, 85(2):290–293, 2000.

[88] Abdelghani Laraoui and Carlos A. Meriles. Rotating frame spin dynamics of a nitrogen-vacancy center in a diamond nanocrystal. *Phys. Rev. B*, 84:161403, 2011.

[89] Malcolm H. Levitt. Composite pulses. *Prog. Nucl. Mag. Res. Spect.*, 18(2):61–122, 1986.

[90] G. Lindblad. On the generators of quantum dynamical semigroups. *Communications in Mathematical Physics*, 48(2):119–130, 1976.

[91] Seth Lloyd. Universal quantum simulators. *Science*, 273(5278):1073–1078, 1996.

[92] Seth Lloyd. Coherent quantum feedback. *Phys. Rev. A*, 62(2):022108, 2000.

[93] J H N Loubser and J A van Wyk. Electron spin resonance in the study of diamond. *Reports on Progress in Physics*, 41(8):1201–1248, 1978.

[94] Hideo Mabuchi. Coherent-feedback quantum control with a dynamic compensator. *Phys. Rev. A*, 78:032323, Sep 2008.

[95] Wilhelm Magnus. On the exponential solution of differential equations for a linear operator. *Communications on Pure and Applied Mathematics*, 7(4):649–673, 1954.

[96] P. Maletinsky, S. Hong, M. S. Grinolds, B. Hausmann, M. D. Lukin, R. L. Walsworth, M. Loncar, and A. Yacoby. A robust scanning diamond sensor for nanoscale imaging with single nitrogen-vacancy centres. *Nat. Nanotech.*, 7(5):320–324, 2012.

[97] N. Manson, L. Rogers, M. Doherty, and L. Hollenberg. Optically induced spin polarisation of the NV- centre in diamond: role of electron-vibration interaction. *ArXiv e-prints*, November 2010.

[98] N. B. Manson, J. P. Harrison, and M. J. Sellars. Nitrogen-vacancy center in diamond: Model of the electronic structure and associated dynamics. *Phys. Rev. B*, 74(10):104303–+, 2006.

[99] N.B. Manson and R.L. McMurtrie. Issues concerning the nitrogen-vacancy center in diamond. *Journal of Luminescence*, 127(1):98 – 103, 2007. Proceedings of the Ninth International Meeting on Hole Burning, Single Molecule, and Related Spectroscopies: Science and Applications, Hole Burning, Single Molecule, and Related Spectroscopies: Science and Applications.

[100] P. C. Maurer, G. Kucsko, C. Latta, L. Jiang, N. Y. Yao, S. D. Bennett, F. Pastawski, D. Hunger, N. Chisholm, M. Markham, D. J. Twitchen, J. I. Cirac, and M. D. Lukin. Room-temperature quantum bit memory exceeding one second. *Science*, 336(6086):1283–1286, 2012.

[101] J. R. Maze, P. L. Stanwix, J. S. Hodges, S. Hong, J. M. Taylor, P. Cappellaro, L. Jiang, A.S. Zibrov, A. Yacoby, R. Walsworth, and M. D. Lukin. Nanoscale magnetic sensing with an individual electronic spin qubit in diamond. *Nature*, 455:644–647, 2008.

[102] J. R. Maze, J. M. Taylor, and M. D. Lukin. Electron spin decoherence of single nitrogen-vacancy defects in diamond. *Phys. Rev. B*, 78(9):094303, 2008.

[103] L. P. McGuinness, Y. Yan, A. Stacey, D. A. Simpson, L. T. Hall, D. Maclaurin, S. Prawer, P. Mulvaney, J. Wrachtrup, F. Caruso, R. E. Scholten, and L. C. L. Hollenberg. Quantum measurement and orientation tracking of fluorescent nanodiamonds inside living cells. *Nat. Nanotech.*, 6(6):358–363, 2011.

[104] W. B. Mims. Envelope modulation in spin-echo experiments. *Phys. Rev. B*, 5(7):2409–2419, 1972.

[105] N. Mizuochi, P. Neumann, F. Rempp, J. Beck, V. Jacques, P. Siyushev, K. Nakamura, D. J. Twitchen, H. Watanabe, S. Yamasaki, F. Jelezko, and J. Wrachtrup. Coherence of single spins coupled to a nuclear spin bath of varying density. *Phys. Rev. B*, 80(4):041201, 2009.

[106] John J. L. Morton et al. Solid-state quantum memory using the ^{31}P nuclear spin. *Nature*, 455(7216):1085–1088, 2008.

[107] John J. L. Morton, Alexei M. Tyryshkin, Richard M. Brown, Shyam Shankar, Brendon W. Lovett, Arzhang Ardavan, Thomas Schenkel, Eugene E. Haller, Joel W. Ager, and S. A. Lyon. Solid-state quantum memory using the ^{31} p nuclear spin. *Nature*, 455(7216):1085–1088, 2008.

[108] Michiel Müller. *Introduction to Confocal Fluorescence Microscopy*. SPIE The international Society for Optical Engineering Vol. TT69, second edition, 2006.

[109] Richard J. Nelson, Yaakov Weinstein, David Cory, and Seth Lloyd. Experimental demonstration of fully coherent quantum feedback. *Phys. Rev. Lett.*, 85(14):3045–3048, 2000.

[110] P Neumann, R Kolesov, V Jacques, J Beck, J Tisler, A Batalov, L Rogers, N B Manson, G Balasubramanian, F Jelezko, and J Wrachtrup. Excited-state spectroscopy of single NV defects in diamond using optically detected magnetic resonance. *New Journal of Physics*, 11(1):013017, 2009.

[111] Philipp Neumann, Johannes Beck, Matthias Steiner, Florian Rempp, Helmut Fedder, Philip R. Hemmer, Jorg Wrachtrup, and Fedor Jelezko. Single-shot readout of a single nuclear spin. *Science*, 5991:542–544, 2010.

[112] Michael A. Nielsen and Isaac L. Chuang. *Quantum computation and quantum information*. Cambridge University Press, Cambridge; New York, 2000.

[113] L. M. Pham, N. Bar-Gill, C. Belthangady, D. Le Sage, P. Cappellaro, M. D. Lukin, A. Yacoby, and R. L. Walsworth. Enhanced solid-state multispin metrology using dynamical decoupling. *Phys. Rev. B*, 86:045214, Jul 2012.

[114] J. R. Rabeau, A. Stacey, A. Rabeau, S. Prawer, F. Jelezko, I. Mirza, and J. Wrachtrup. Single nitrogen vacancy centers in chemical vapor deposited diamond nanocrystals. *Nano Letters*, 7(11):3433–3437, 2007.

[115] Norman F. Ramsey. *Molecular Beams*. Oxford University Press, 1990.

[116] Alfred G. Redfield. Nuclear magnetic resonance saturation and rotary saturation in solids. *Phys. Rev.*, 98:1787–1809, 1955.

[117] Lucio Robledo, Hannes Bernien, Toeno van der Sar, and Ronald Hanson. Spin dynamics in the optical cycle of single nitrogen-vacancy centres in diamond. *New J. Phys.*, 13(2):025013, 2011.

[118] Lucio Robledo, Hannes Bernien, Toeno van der Sar, and Ronald Hanson. Spin dynamics in the optical cycle of single nitrogen-vacancy centres in diamond. *New Journal of Physics*, 13(2):025013, 2011.

[119] L. J. Rogers, S. Armstrong, M. J. Sellars, and N. B. Manson. Infrared emission of the NV centre in diamond: Zeeman and uniaxial stress studies. *New J. Phys.*, 10(10):103024, 2008.

[120] L J Rogers, M W Doherty, M S J Barson, S Onoda, T Ohshima, and N B Manson. Singlet levels of the NV^- centre in diamond. *New Journal of Physics*, 17(1):013048, 2015.

[121] L J Rogers, R L McMurtrie, M J Sellars, and N B Manson. Time-averaging within the excited state of the nitrogen-vacancy centre in diamond. *New Journal of Physics*, 11(6):063007, 2009.

[122] T. Rosenband, D. B. Hume, P. O. Schmidt, C. W. Chou, A. Brusch, L. Lorini, W. H. Oskay, R. E. Drullinger, T. M. Fortier, J. E. Stalnaker, S. A. Diddams, W. C. Swann, N. R. Newbury, W. M. Itano, D. J. Wineland, and J. C. Bergquist. Frequency ratio of Al^+ and Hg^+ single-ion optical clocks; metrology at the 17th decimal place. *Science*, 319(5871):1808–1812, 2008.

[123] D. Rugar, R. Budakian, H. J. Mamin, and B. W. Chui. Single spin detection by magnetic resonance force microscopy. *Nature*, 430(6997):329–332, 2004.

[124] C. A. Ryan, J. S. Hodges, and D. G. Cory. Robust decoupling techniques to extend quantum coherence in diamond. *Phys. Rev. Lett.*, 105(20):200402, 2010.

[125] Kamyar Saeedi, Stephanie Simmons, Jeff Z. Salvail, Phillip Dluhy, Helge Riemann, Nikolai V. Abrosimov, Peter Becker, Hans-Joachim Pohl, John J. L. Morton, and Mike L. W. Thewalt. Room-temperature quantum bit storage exceeding 39 minutes using ionized donors in silicon-28. *Science*, 342(6160):830–833, 2013.

[126] J. J. Sakurai. *Modern Quantum Mechanics*. Addison-Wesley, Reading, Massachusetts, revised edition edition, 1994.

[127] S. G. Schirmer and P. deFouquieres. Efficient algorithms for optimal control of quantum dynamics: the krotov method unencumbered. *New J. Phys.*, 13(7):073029, 2011.

[128] Arthur Schweiger and Gunnar Jeschke. *Principles of Pulse Electron Paramagnetic Resonance*. Oxford University Press, first edition, 2001.

[129] S.K. Sekatskii and V.S. Letokhov. Nanometer-resolution scanning optical microscope with resonance excitation of the fluorescence of the samples from a single-atom excited center. *Journal of Experimental and Theoretical Physics Letters*, 63(5):319–323, 1996.

[130] A.J Shaka, James Keeler, and Ray Freeman. Evaluation of a new broadband decoupling sequence: Waltz-16. *J. Mag. Res.*, 53(2):313–340, June 1983.

[131] Peter W. Shor. Fault-tolerant quantum computation. In *37th Annual Symposium on Foundations of Computer Science*, pages 56–65. IEEE Comput. Soc. Press, Los Alamitos, CA, 1996.

[132] Peter W Shor. Polynomial-time algorithms for prime factorization and discrete logarithms on a quantum computer. *Siam J.Sci.Stat.Comp.*, 26:1484, 1997.

[133] C. P. Slichter. *Principles of Magnetic Resonance*. Springer-Verlag, 3rd edition, 1996.

[134] Benjamin Smeltzer, Jean McIntyre, and Lilian Childress. Robust control of individual nuclear spins in diamond. *Phys. Rev. A*, 80:050302, Nov 2009.

[135] I. Solomon. Multiple echoes in solids. *Phys. Rev.*, 110:61–65, 1958.

[136] M. Steiner, P. Neumann, J. Beck, F. Jelezko, and J. Wrachtrup. *Phys. Rev. B*, 81(3):035205, 2010.

[137] Ph Tamarat, N B Manson, J P Harrison, R L McMurtrie, A Nizovtsev, C Santori, R G Beausoleil, P Neumann, T Gaebel, F Jelezko, P Hemmer, and J Wrachtrup. Spin-flip and spin-conserving optical transitions of the nitrogen-vacancy centre in diamond. *New Journal of Physics*, 10(4):045004, 2008.

[138] T. H. Taminiau, J. J. T. Wagenaar, T. van der Sar, F. Jelezko, V. V. Dobrovitski, and R. Hanson. Detection and control of individual nuclear spins using a weakly coupled electron spin. *Phys. Rev. Lett.*, 109:137602, Sep 2012.

[139] J. M. Taylor, P. Cappellaro, L. Childress, L. Jiang, D. Budker, P. R. Hemmer, A. Yacoby, R. Walsworth, and M. D. Lukin. High-sensitivity diamond magnetometer with nanoscale resolution. *Nat. Phys.*, 4(10):810–816, 2008.

[140] Cornelis J. Terblanche, Eduard C. Reynhardt, Sergei A. Rakitianski, and Jan A. Van Wyk. 13c spin-lattice relaxation in natural diamond: Zeeman relaxation in fields of 500 to 5000 g at 300 k due to fixed paramagnetic nitrogen defects. *Solid State Nuclear Magnetic Resonance*, 19(3-4):107 – 129, 2001.

[141] Francesco Ticozzi and Lorenza Viola. Single-bit feedback and quantum-dynamical decoupling. *Phys. Rev. A*, 74(5):052328, 2006.

[142] Götz S. Uhrig. Keeping a quantum bit alive by optimized pi-pulse sequences. *Phys. Rev. Lett.*, 98(10):100504, 2007.

[143] L. Viola and S. Lloyd. Dynamical suppression of decoherence in two-state quantum systems. *Phys. Rev. A*, 58:2733, 1998.

[144] Lorenza Viola, Emanuel Knill, and Seth Lloyd. Dynamical decoupling of open quantum systems. *Phys. Rev. Lett.*, 82(12):2417–2421, 1999.

[145] N.V. Vitanov, B.W. Shore, L. Yatsenko, K. Böhmer, T. Halfmann, T. Rickes, and K. Bergmann. Power broadening revisited: theory and experiment. *Optics Communications*, 199(14):117 – 126, 2001.

[146] G. Waldherr, J. Beck, M. Steiner, P. Neumann, A. Gali, Th. Frauenheim, F. Jelezko, and J. Wrachtrup. Dark states of single nitrogen-vacancy centers in diamond unraveled by single shot nmr. *Phys. Rev. Lett.*, 106:157601, 2011.

[147] Hai-Jing Wang, Chang S. Shin, Claudia E. Avalos, Scott J. Seltzer, Dmitry Budker, Alexander Pines, and Vikram S. Bajaj. Sensitive magnetic control of ensemble nuclear spin hyperpolarization in diamond. *Nat Commun*, 4:–, June 2013.

[148] Xiaoting Wang and S.G. Schirmer. Analysis of lyapunov method for control of quantum states. *Automatic Control, IEEE Transactions on*, 55(10):2259–2270, Oct 2010.

[149] Zhi-Hui Wang, Wenxian Zhang, A. M. Tyryshkin, S. A. Lyon, J. W. Ager, E. E. Haller, and V. V. Dobrovitski. Effect of pulse error accumulation on dynamical decoupling of the electron spins of phosphorus donors in silicon. *Phys. Rev. B*, 85:085206, 2012.

[150] H. M. Wiseman and G. J. Milburn. Quantum theory of optical feedback via homodyne detection. *Phys. Rev. Lett.*, 70:548–551, Feb 1993.

[151] H. M. Wiseman and G. J. Milburn. All-optical versus electro-optical quantum-limited feedback. *Phys. Rev. A*, 49:4110–4125, May 1994.

[152] H.M. Wiseman and G.J. Milburn. *Quantum measurement and control*. Cambridge University Press, 2009.

[153] J. Wrachtrup, S. Kilin, and A. Nizovtsev. Quantum computation using the 13c nuclear spins near the single nv defect center in diamond. *Optics and Spectroscopy*, 91(3):429–437, 2001.

[154] J. Wrachtrup, C. von Borczyskowski, J. Bernard, M. Orrit, and R. Brown. Optical detection of magnetic resonance in a single molecule. *Nature*, 363:244–245, 1993.

[155] J. Wrachtrup, C. von Borczyskowski, J. Bernard, M. Orrit, and R. Brown. Optically detected spin coherence of single molecules. *Phys. Rev. Lett.*, 71(21):3565–3568, 1993.

[156] Kevin C. Young and K. Birgitta Whaley. Qubits as spectrometers of dephasing noise. *Phys. Rev. A*, 86:012314, 2012.

[157] A.M. Zaitsev. *Optical Properties of Diamond*. Springer-Verlag, 2001.

[158] Wojciech H. Zurek. Decoherence and the transition from quantum to classical. *Physics Today*, 44(10):36–44, 1991.

[159] Andrei V. Zvyagin and Neil B. Manson. Chapter 10 - optical and spin properties of nitrogen-vacancy color centers in diamond crystals, nanodiamonds, and proximity to surfaces. In Olga A. ShenderovaDieter M. Gruen, editor, *Ultananocrystalline Diamond (Second Edition)*, pages 327 – 354. William Andrew Publishing, Oxford, second edition edition, 2012.